Scuola Internazionale Superiore di Studi Avanzati - Trieste

Characterizing the role of the PrP^C N-terminal domain in protein and metal binding: NMR and XAS studies

Giulia Salzano

A thesis submitted for the degree of
Doctor of Philosophy
in Functional and Structural Genomics
October 2017

SISSA - Via Bonomea 265 - 34136 TRIESTE - ITALY

Scuola Internazionale Superiore Studi Avanzati
(SISSA)

Characterizing the role of the PrP^{C} N-terminal domain in protein and metal binding: NMR and XAS studies

Giulia Salzano

A thesis submitted for the degree of
Doctor of Philosophy
in Functional and Structural Genomics
October 2017

Supervisor:	**Prof. Giuseppe Legname, Ph.D.**
External examiners:	**Roberto Fattorusso, Ph.D.**
	Jesus Requena, Ph.D.

ABSTRACT

The conversion of the cellular prion protein PrP^{C} into the infectious isoform (PrP^{Sc}) is the key event in prion diseases. The physiological role of PrP^{C} remains one of main challenges in prion biology, and it is an absolute requirement also for understanding prion diseases. Putative roles for PrP^{C} are based on its localization in the central and peripheral nervous systems and on PrP^{C}-interacting molecules or metal ions through its unstructured N-terminal domain.

We analysed the function of the cellular prion protein using structural biology techniques aimed to analyze the interaction between PrP^{C} and NCAM and PrP^{C} with copper ions. We first focused on the structural determinants responsible for human PrP^{C} (HuPrP) and NCAM interaction using Stimulated Emission Depletion (STED) nanoscopy, surface plasma resonance (SPR) and NMR spectroscopy approaches. Such structural and biological investigations revealed surface interacting epitopes governing the interaction between HuPrP N-terminus and the second module of NCAM Fibronectin type-3 domain, providing molecular details about the interaction between HuPrP and NCAM Fibronectin domain, and revealed a new role of PrP^{C} N-terminus as a dynamic and functional element responsible for protein-protein interaction.

Subsequently, we have investigated the role of copper in prion conversion and susceptibility with a special focus on the non-OR copper binding site. The molecular mechanisms of prion conversion are still debated. NMR-based studies on HuPrP and MoPrP globular domains have identified the β2-α2 loop as important element able to modulate the susceptibility of a given species to prion disease. However, recent studies have highlighted also the importance of the N-terminal region in promoting structural rearrangements to PrP^{Sc}. We studied copper coordination in the non-OR region of different species including human, sheep, bank vole and opossum. By using *in vitro* approaches, cell-based and computational techniques, we propose two types of copper coordination geometries, where the type-1 Cu(II) coordination displays a closed non-OR region conformation associated with less-susceptible species, while in type-2 a less structured and solvent exposed non-OR region might render the overall PrP^{C} structure more flexible, therefore we correlate this with higher susceptibility to prion diseases. Our data highlighted how copper coordination in the non-OR copper binding site may explain the different susceptibility to prion diseases observed in these mammalian species.

Ultimately, in the present thesis we expanded our knowledge on how the N-terminus of PrP^{C} regulates the physiological functions of PrP^{C} and how it is involved in the prion conversion.

LIST OF PUBLICATIONS

All the work reported here arises from my own experiments and data analysis performed in SISSA or as a result of joint collaborations with other groups. Most of the data was published in the following articles.

- Slapšak U., **Salzano G.**, Amin L., Abskharon R.N.N., Ilc G., Zupančič B., Biljan I., Plavec J., Giachin G. and Legname G. Prion Protein N-terminus Mediates Functional Interactions with NCAM Fibronectin Domain. J. Biol. Chem., 291, 21857-21868.
Author contribution: provided the sample, contributed to performing the experiments, analyzing the data and writing the paper.

- Giachin G.; Mai T.P.; Tran H.T.; **Salzano G.**; Benetti F.; Migliorati V.; Arcovito A.; Della Longa S.; Mancini G.; D 'Angelo P.; Legname G. The non-octarepeat copper binding site of the prion protein is a key regulator of prion conversion. Sci. Rep. 5, 15253; doi: 10.1038/srep15253 (2015).
Author contribution: provided the sample, contributed to performing the experiments, analyzing the data and writing the paper.

- Le N.T.; Narkiewicz J.; Aulić S.; **Salzano G.**; Tran H.T.; Scaini D.; Moda F.; Giachin G.; Legname G. Synthetic prions and other human neurodegenerative proteinopathies. Virus Res. 2014 Oct 31. pii: S0168-1702(14)00437-7.
Author contribution: contributed to writing the paper.

Other publications not cited here

Moda F., Bistaffa E., Narkiewicz J., **Salzano G.**, Legname G. Synthetic Mammalian Prions. In Prion Diseases; Pawel Liberski Eds.; Neuromethods, 2017.
Author contribution: contributed to writing the chapter.

- Redaelli V., Bistaffa E., Zanusso G., **Salzano G.**, Sacchetto L., Rossi M., De Luca C., Di Bari M., Portaleone SM., Agrimi U., Legname G., Roiter I., Forloni G., Tagliavini F., Moda F. Detection of prion seeding activity in the olfactory mucosa of patients with Fatal Familial Insomnia. Sci. Rep. 2017 Apr 7;7:46269. doi: 10.1038/srep46269.
Author contribution: provided the samples and contributed to writing the paper.

LIST OF ABBREVIATIONS

3D: three-dimensional
ASA: amyloid seeding assay
BCL: short peptide from neuronal cell adhesion molecule
Bv: bank vole
CC_1: charged aminoacid cluster 1(residue 23-27) in the HuPrP sequence
CC_2: charged aminoacid cluster 2 (residue 95-110) in the HuPrP sequence
CNS: central nervous system
CJD: Creutzfeldt-Jakob disease
CPZ: cuprizone
CWD: chronic wasting disease
Dpl: Doppel
DRMs: detergent insoluble membrane domains
Edbg: Edinburgh or *Prnp*$^{-/-}$, a PrP^C-null mice strain
ER: endoplasmic reticulum
f: familial
FFI: Fatal familial insomnia
FNIII: fibronectin type III domain
FSE: Feline spongiform encephalopathy
FT: Fourier Transform
GAGs: glycosaminoglycans
GPI: glycosylphosphatidylinositol
GSS: Gerstmann-Sträussler–Scheinker
GT1: mouse hypothalamic cells line
HB: hydrogen bond
HD: hydrophobic domain (residue 111-134) in the HuPrP sequence
Hu: human
IBs: inclusion bodies
Ig: immunoglobulin
IPTG: isopropyl b-D-galactopyranoside
KI: knockin
LRP1: low density lipoprotein receptor-related protein
LRP: 37-kDa/67-kDa laminin receptor precursor
MD: molecular dynamic
MM: minimal medium
Mo: mouse
N2a: mouse neuroblastoma cells line
NCAM: neuronal cell adhesion molecule
neo: neomycin phosphotransferase expression cassette
Ngsk: Nagasaki, a PrP^C-null mice strain
NMR: nuclear magnetic resonance
NOE: nuclear Overhauser enhancement
Op: opossum
OR: octapeptide-repeat region
ORF: open reading frame
Ov: ovine

PMCA: Protein Misfolding Cyclic Amplification
PrP: prion protein
PrP^{C}: physiological cellular form of PrP
PrP^{Sc}: misfolded, pathogenic form of PrP^{C}, also denoted as prion.
^{Ctm}PrP: C-terminal transmembrane PrP form
^{Ntm}PrP: N-terminal transmembrane PrP form
PrP^{*}: partially destabilized folding intermediate of PrP^{C}
PK: protease K
PRNP: human prion protein gene
Prnp: prion protein gene in non human species
Prnd: Doppel gene in non human species
Sh: Syrian Hamster
rec: recombinant
RMSD: root main square deviation
RT: room temperature
s: sporadic
SB: salt bridge
ScGT1: chronically PrP^{Sc} infected mouse hypothalamic cells line
ScN2a: chronically PrP^{Sc} infected mouse neuroblastoma cells line
SPR: surface plasma resonance
STED: stimulated emission depletion nanoscopy
STI1: stress-inducible protein I
Tg: transgenic
ThT: thioflavin T
TME: Transmissible Mink Encephalopathy
TSEs: transmissible spongiform encephalopathies, also denoted as prion diseases
WT: wild-type
XAFS: X-ray absorption fine structure
ZrchI: Zurich I or $Prnp^{0/0}$, a PrP^{C}-null mice strain

TABLE OF CONTENTS

Chapter III

Chapter IV

CHAPTER I

INTRODUCTION

1.1 Biogenesis of PrP^C

The prion protein (PrP) gene (*PRNP* in human or *Prnp* in other species) is highly conserved among species. The complete open reading frame (ORF) of all known PrP genes is located within a single exon [1-3]. In mouse, sheep, cattle, and rat the PrP gene contains three exons with the ORF located in exon 3, while human, Syrian hamster, opossum and tammar wallaby have 2 exons with the PrP ORF present in exon 2. The other exons contain untranslated sequences including the promoter and termination sites. The PrP promoter contains multiple copies of GC rich repeats and is devoid of TATA box [4, 5]. In humans, *PRNP* is a single copy gene mapped in the short arm of chromosome 20, which corresponds to the homologous region of mouse chromosome 2 where *Prnp* is located. PrP mRNA has been detected in a wide range of tissues and cell types, but the highest concentration is found in the brain, where *in situ* hybridization has demonstrated that the greatest abundance of mRNA is located in neurons [6-8].

As a typical cell-surface glycoprotein, the pre-pro-protein is translocated to the endoplasmic reticulum (ER) due to the presence of a 23 amino acids N-terminal signal peptide that is then cleaved into the ER lumen. Here, the immature PrP is subjected to several post-translational modifications including N-linked glycosylation at residues N181 and N197 of human (Hu), formation of a single disulfide bond at position C179 and C214, cleavage of the C-terminal signal peptide and subsequent attachment of the glycosylphosphatidyl inositol (GPI) anchor at position 231 [9-11]. During co-translational translocation in the ER, PrP can be synthesized with three topologies in the ER. The majority of PrP nascent chains generate a secreted form of PrP that follow the traditional exocytic pathway to the cell surface. In addition, two C- or N-terminal transmembrane forms, denoted as ^{Ctm}PrP and ^{Ntm}PrP, respectively, due to transmembrane insertion of the PrP hydrophobic domain (residues from 110 to 134) in the ER compartment are synthesized [12] (**Figure 1.1**). The role of the minor forms, ^{Ctm}PrP and ^{Ntm}PrP, is still not fully clarified but may be associated with neurotoxicity and cellular death especially in case of inherited prion diseases [13].

The mature GPI-anchored form, PrP^C, is derived from the secreted form, which fully translocates into the ER and is trafficked through the Golgi apparatus. Here, further processing of the N-linked oligosaccharides results in modified glycosylation to complex-type sugar chains.

Glycosylation of PrP^C is variable, resulting in un-, mono-, or diglycosylated species, depending on the number of glycosylation sites occupied with oligosaccharide chains [14]. The mature PrP^C is found mostly in the cholesterol- and sphingolipid-rich membrane domains, also known as lipid rafts, which are detergent-resistant membrane domains with many important cellular receptors and other GPI-anchored proteins [15]. Interestingly, the association of PrP^C with lipid rafts seems to be required for its correct folding, as cholesterol depletion led to its misfolding [16-18].

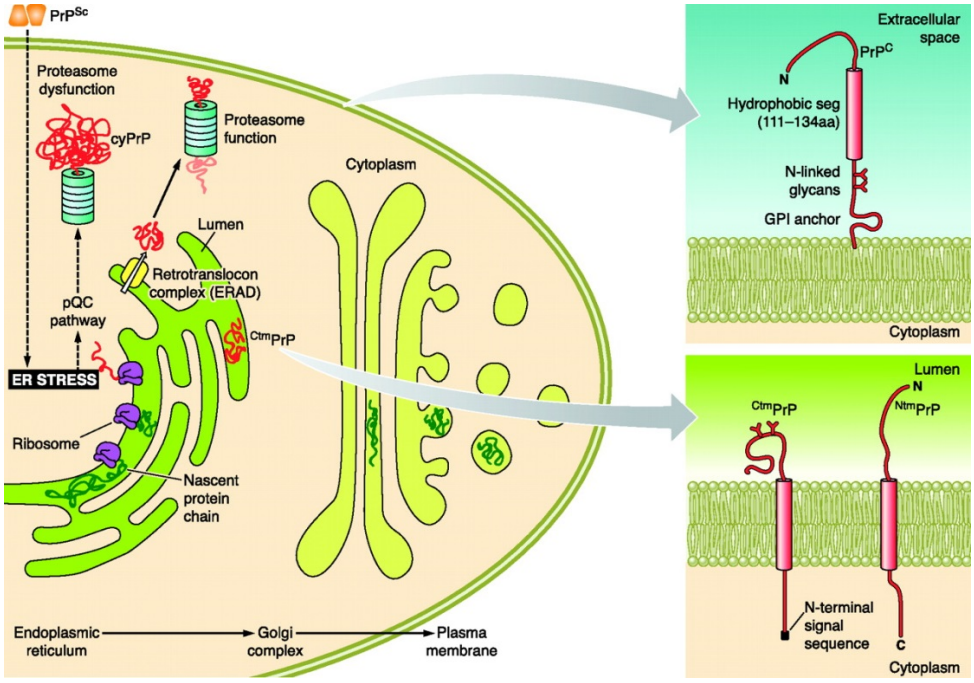

Figure 1.1 Biogenesis of PrP^C. The cellular prion protein, PrP^C (green coils), is synthesized, folded, and glycosylated in the endoplasmic reticulum (ER), where its glycosyl phosphatidylinositol (GPI) anchor is added, before further modification in the Golgi complex. Mature PrP^C translocates to the outer leaflet of the plasma membrane. Instead, ^{Ctm}PrP and ^{Ntm}PrP are unusual transmembrane forms, generated in the ER, which have their COOH or NH_2 terminus in the ER lumen, respectively (modified from [19]).

PrP^C undergoes cyclic rounds of endocytosis [20] with a transit time of approximately 60 minutes [21]. The process occurs between the cell surface and the endocytic compartment and it can follow either clathrin-dependent pathways, or be mediated by "caveolae-like" domains [20]. It was proposed that the N-terminal positively charged motif, KKRPKP, is responsible for the endocytosis of PrP^C by clathrin-coated vesicles [22]. From the cell surface, PrP^C can be endocyted to internal endosomal compartments, delivered from early to late endosomes, and routed to lysosomes for degradation or recycled to the cell surface for ensuing cycles.

1.2 Structural Biology of the Human PrP^C

The human PrP (HuPrP) gene encodes a 253 amino acids long pre-pro-protein that is subsequently processed as mentioned before. In the mature form, the first 22 residues are cleaved after translation, whereas the last 23 amino acid residues are cleaved prior to the addition of the GPI anchor to Ser231. The mature human PrP^C (HuPrP) is composed of 209 residues. The majority of high-resolution structural studies on PrP^C were carried out with bacterially expressed recombinant (rec) PrP, lacking the Asn-linked glycosylation at residues 181 and 197 [23]. Atomic structures obtained by NMR techniques and X-ray crystallography revealed that recPrP shares a very similar fold across different mammalian species [24]. The full-length PrP^C has a unique structure: while the N-terminal moiety (from residue 23 to 127) does not adopt any identifiable folding structure in solution [25], the C-terminus adopts a predominantly α-helical conformation with small β-sheet content (residues 128–231) [26].

The N-terminus half of the protein may be divided into four different consecutive domains, a first charge cluster or CC1, the octapeptide repeat (OR), a second charge cluster or CC2, and a hydrophobic domain-termed (HD), containing a palindromic region consisting of an alanine-rich tract of amino acids, AGAAAAGA, which is highly conserved across a wide variety of mammalian species. CC1 and CC2 (residue 23-27 and 95-110, respectively) seem be involved in glycosaminoglycans (GAGs) [27, 28] and nucleic acids [29, 30] binding. It has been observed that the CC1 region is involved in recycling and internalizing PrP^C from the cell surface [31]. However, mice lacking CC1 or CC2 domains did not show pathologies and are susceptible to prion infection [32, 33].

The HD is believed to play a role in the PrP^C function in concert with CC2. Indeed, ablation of CC2 in combination with a partial or complete deletion of HD causes severe pathologies in transgenic (Tg) mice, suffering from ataxia to cerebellar granule cell loss. A partial deletion of HD is not toxic [34].

The palindromic sequence AGAAAGA is also known as “toxic peptide”, because short peptides corresponding to this segment form fibrils in solution with β-sheet structure which are toxic to cultured mouse hippocampal cells, suggesting that this palindromic sequence may be involved in the PrP^{Sc} to PrP^C conversion [35-37]. During the conversion, the region encompassing the CC2 and HD is not accessible to antibodies recognizing this epitope in PrP^C [38], indicating that this segment undergoes profound conformational changes upon conversion to PrP^{Sc}. Moreover, antibodies directed against this region effectively halt prion replication in ScN2a cells [39].

The octapeptide-repeat region (OR) is an evolutionarily conserved motif, where histidine and tryptophan residues were found to be essential for the binding of copper and other divalent cations. The interaction between PrP^C and copper will be discussed in more detailed in section 1.7.3.

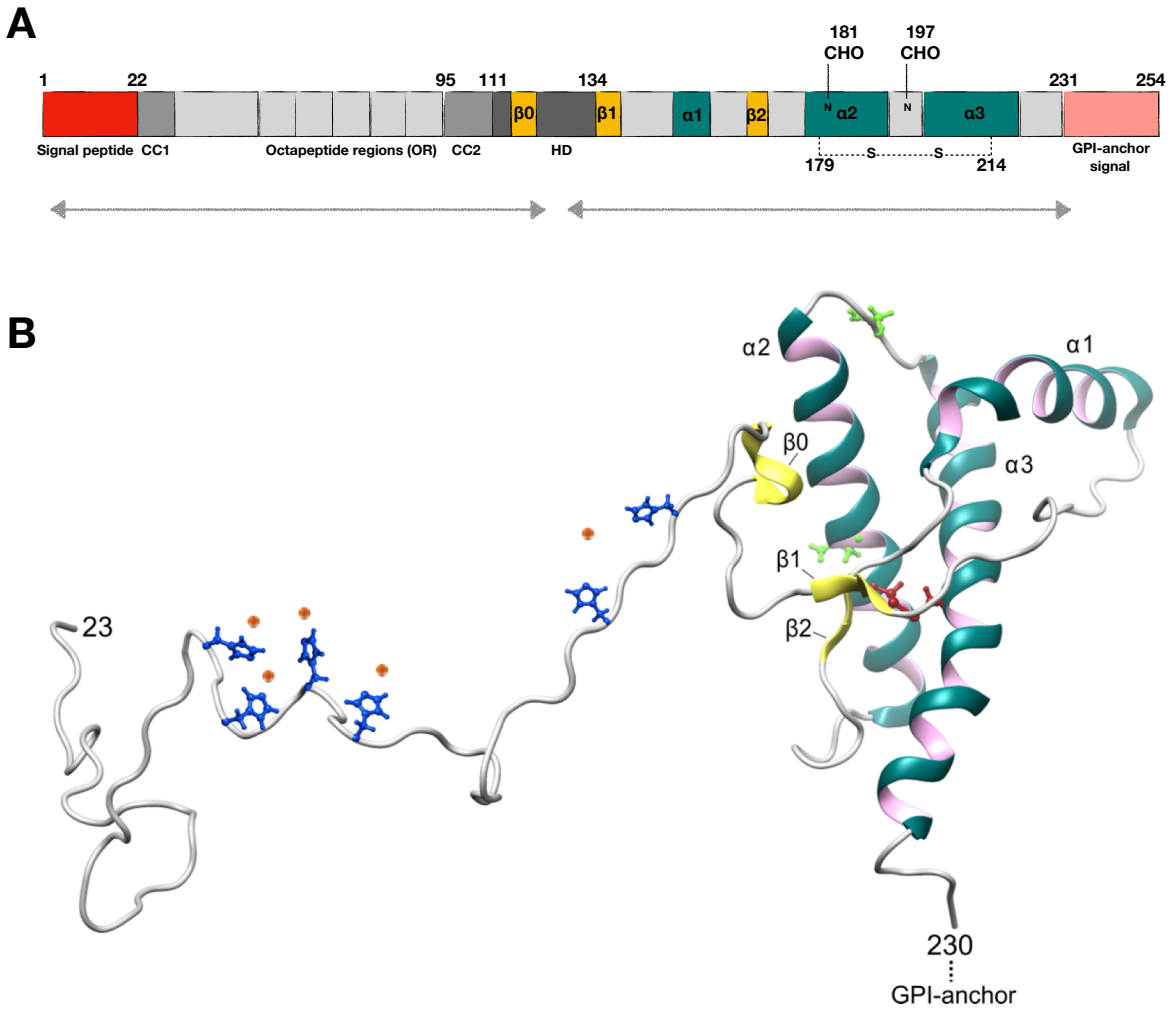

Figure 1.2. The structure of cellular prion protein. (**A**) Schematic illustration of primary PrP^C structure. CC1: charged cluster 1, CC2: charged cluster 2, HD: hydrophobic domain. (**B**) Secondary structure of PrP^C. Histidine residues are highlighted in blue, copper ions in orange.

The structured C-terminal domain is composed of three α-helices (α1, α2 and α3) and two very short β-strands which form an antiparallel β-sheet (β1 and β2). A third β-sheet strand has been recently identified and named β0 [40, 41].

Helices α2 and α3 form the bulk of the globular domain and are covalently bridged by a disulfide bond between Cys179 and Cys214 (**Figure 1.2**). The C-terminal NMR structures of WT HuPrP obtained at different pH values (4.5, 5.5 and 7.0) show almost identical backbone tertiary structures with local differences in flexible regions [25, 42, 43].

1.3 PrP^C and prion diseases

The post-translational conversion of PrP^C into the misfolded, pathogenic form, called prion or PrP^{Sc}, plays a key role in transmissible spongiform encephalopathies (TSEs), or prion diseases. Prion diseases are transmissible neurodegenerative disorders affecting human and a wide range of animal species. These disorders can arise sporadically, be inherited, or be acquired through infection.

1.3.1 Animal prion diseases

Animal prion diseases include scrapie of sheep, goats and mufflons [44], bovine spongiform encephalopathy (BSE) in cow [45], transmissible mink encephalopathy (TME) in ranch-reared mink [46], feline spongiform encephalopathy (FSE) in domestic cats [47], chronic wasting disease (CWD) of cervids and spongiform encephalopathy of primates [48].

Scrapie is the ancient form of TSEs. It occurred in sheep and goats [49]. Neuropathological signs are spongiform vacuolation, astrogliosis and the deposition of PrP^{Sc} amyloid plaques in the central nervous system (CNS). The incubation period of scrapie is 2-5 years and death occurs within 2 weeks to 6 months after clinical onset. Several polymorphisms in *Prnp* have been associated to scrapie susceptibility in goat and sheep. For example, Q171R and A136V polymorphisms confer resistance and susceptibility to the infection, respectively. This part will be discussed in more detailed in section 1.6.2.

Bovine Spongiform Encephalopathy (BSE) is a fatal neurodegeneration in cattle. The pathology presents with tremors, ataxia, aggressive behavior and hyperactivity to stimuli. PrP^{Sc} accumulation and spongiform vacuolation are usually found in the brain, and the incubation period for BSE is 2 to 8 years. Besides the classical BSE (cBSE), in recent years two atypical forms of BSE have been identified in several European countries [50], Japan [51, 52], United States [53] and Canada [54]. The two atypical BSE strains -denoted as H-type BSE and L-type BSE- [55] are identified by the higher and lower electrophoretic mobility of the unglycosylated protease resistant PrP^{Sc} fragment, respectively [56]. Histopathological as well as immuno-histochemical analyses show that atypical forms of BSE can be experimentally transmitted to transgenic mice and primates and clearly differ from cBSE isolates, with unique incubation periods, PrP^{Sc} profiles and histological lesions [57, 58].

CWD is a TSE of captive as well as free-ranging members of the family *Cervidae*. Since 1967 CWD has been documented in 24 USA states, 2 Canadian provinces and in imported animals in South Korea. Recently, it has also been confirmed 5 cases of CWD in Norway. The affected species include mule deer (*Odocoileus hemionus*) [59], white-tailed deer (*O. virginianus*) [60], Rocky Mountain elk (*Cervus elaphus nelsoni*) [48], and moose (*Alces alces shirasi*) [61]. Deer and elk with CWD show subtle signs of disease, characterized by weight loss, isolation from the herd, hypersalivation and rarely ataxia. The origin of CWD is still unknown, although intracerebral transmission of the scrapie agent has been shown to induce the disease in elk. Epidemiological and experimental data provide evidence that horizontal transmission of CWD can efficiently occur by contact with affected animals or through environmental exposure [60, 62-65]. Until now, the natural transmission of CWD has not been proved in humans who have

been exposed for long to the affected area and consumed venison. Moreover, transgenic mice expressing either the human, ovine or bovine PrP^{C} coding frames did not develop the disease when inoculated with the CWD agent.

Transmissible mink encephalopathy (TME) and feline spongiform encephalopathy are very rare prion diseases. TME outbreaks have been reported in ranched mink in the United States of America (Wisconsin, Idaho and Minnesota) and FSE has been reported in domestic cats and captive wild members of the family *Felidae* in the UK, with a few cases identified in France, Australia, Ireland, and Germany. Histopathological analysis of FSE cases revealed spongiform degeneration in the brain and spinal cords, with substantial variations in terms of vacuolation and PrP^{Sc} aggregation profiles depending on the affected species. For these two uncommon TSEs, the death occurs after 2-8 weeks of the clinical onset.

1.3.2. Human prion diseases

In human, TSEs include a heterogeneous group of invariably fatal neurodegenerative diseases evenly distributed worldwide and etiologically arising as sporadic, genetic or acquired. According to the recent classification, idiopathic forms include sporadic Creutzfeldt-Jakob disease (sCJD) [66], sporadic fatal insomnia (sFI) and the variably protease sensitive prionopathies (VPSPr). Genetic forms comprise familial CJD (fCJD), Gerstmann-Sträussler-Scheinker disease (GSS) [67], fatal familial insomnia (FFI) [68] and prion protein cerebral amyloid angiopathy (PrP-CAA). The acquired forms are transmitted from human to human, as iatrogenic CJD (iCJD) or Kuru [69], from cattle to human, and human to human, as variant CJD (vCJD). Sporadic CJD is the most frequent form and accounts for an incidence of about 0.6–1.2 per million per year [70]. Genetic forms account for 10%–15% of human prion diseases, whereas the acquired forms are negligible [71]. Key evidence exists supporting the link between mutations in *PRNP* and genetic prion diseases. Several mutations linked to fCJD, GSS and FFI have been identified (**Figure 1.3**); they display many effects both at the structural and pathological levels. Since in genetic prion diseases the conversion process from PrP^{C} to PrP^{Sc} appears to occur spontaneously in the brain, they represent an invaluable tool for the comprehension of the molecular basis of TSEs.

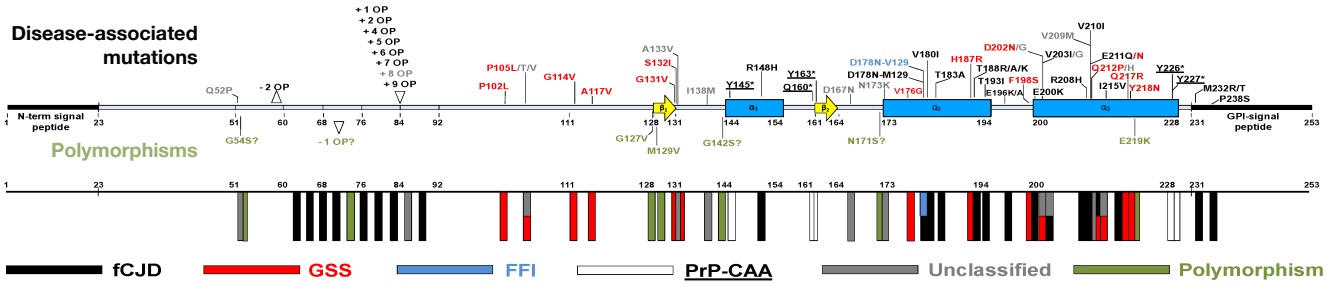

Figure 1.3. Secondary structure of the immature HuPrP with all the currently identified disease-associated mutations and polymorphisms (unclassified phenotype in gray; fCJD in black; GSS in red; PrP-CAA underlined; FFI in blue; and polymorphisms in green). The mature HuPrP consists of residues 23–231, while the N-terminal and

C-terminal signal peptides are cleaved during protein maturation. In the lower panel, the frequency of the mutations and polymorphisms along the *PRNP* sequence is represented by colored rectangles (modified from [72]).

It has been proposed that *in vitro* disease-linked mutations increase the likelihood of misfolding by the thermodynamic destabilization of PrP^C [73-75], although individual mutations differently affect PrP^C stability. Mutations may also alter surface properties of PrP^C, triggering in turn an abnormal interaction with other not yet identified cofactors [76, 77], or causing an aberrant trafficking and accumulation inside the cell [78].

1.4 The "protein-only" hypothesis

According to the protein-only hypothesis, the central molecular event in the replication of prions is the self-propagating conversion of PrP^C to PrP^{Sc} [79]. Two different mechanisms have been proposed (**Figure 1.4**).

The nucleation-polymerization model states that PrP^C and PrP^{Sc} are at equilibrium, but the latter is much less stable, shifting the equilibrium toward the cellular form. Stabilization of PrP^C occurs only when a stable oligomeric nucleus appears [80]. After this passage, PrP^C can adopt the scrapie conformation. The rate-limiting step is the formation of the stable nucleus. This step of stable nucleus reflects the lag phase of spontaneous conversion and it is accelerated by adding preformed PrP^{Sc} seeds.

The template assisted model expects that PrP^C can rarely adopt the PrP^{Sc} conformer, which is more thermodynamically stable but kinetically inaccessible [81]. Whenever PrP^{Sc} occurs spontaneously or is provided exogenously, it can template the misfolding of PrP^C with a direct interaction. The rate-limiting state in this model is represented by the dimerization between PrP^C and PrP^{Sc} monomers, or the formation of a less stable folding intermediate denoted PrP*.

The two models are mutually exclusive; in fact, the nucleation-polymerization model could explain the initial formation of the seed, while the template-assisted model could be involved in the elongation of fibrils. However, in both cases the formation of oligomeric structures or amyloid fibrils represents thermodynamic minima, with respect to PrP^C and PrP^{Sc}, making this process spontaneous.

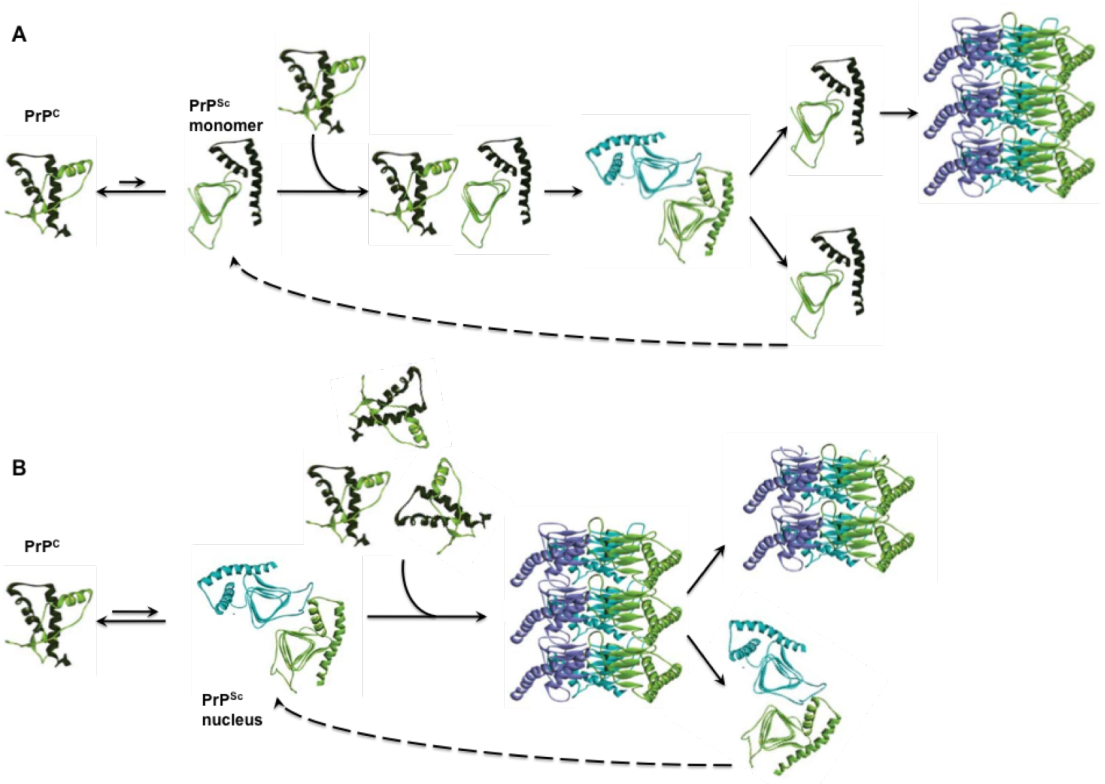

Figure 1.4. (**A**) Template-assisted model and (**B**) nucleation-polymerization model (modified from [26]).

1.5 Structural biology of synthetic prions

Determining the structure of prions is of utmost importance in prion biology to understand the molecular mechanisms leading to the conversion process whereby α-helical motifs in PrP^{C} are replaced by β-sheet secondary structures in PrP^{Sc}.

A defining feature of PrP^{Sc} is a high resistance to degradation by proteolytic enzymes such as the Proteinase K (PK). Limited proteolysis on PrP^{Sc} usually generates a smaller C-terminal PK-resistant molecule composed by approximately 142 residues starting from residue ~90. Historically, PrP^{Sc} is denoted also as PrP27-30 because of its electrophoretic mobility, which encompasses a molecular weight from 27 to 30 kDa [82]. The protease-resistant core of PrP^{Sc} has been shown to form aggregates and amyloid, which stain with Congo red and show green-gold bi-refringence, typical of amyloids [83]. However, it has been shown that the amyloid properties of PrP^{Sc} are not an obligatory feature of prion diseases [84] and not all PrP^{Sc} molecules are resistant to protease digestion [85].

One feature that distinguishes the two isoforms is their secondary structures. Fourier Transform Infrared Spectroscopy (FTIR) and circular dichroism studies have shown that unlike PrP^{C}, which is predominantly α-helix (47% α-helix and only 3% β-sheet), PrP^{Sc} is mainly β-sheet enriched [86]. Because PrP^{Sc} is insoluble and forms aggregates, the atomic structure of PrP^{Sc} is still unclear.

Over the years, different biochemical and biophysical methods, such as spectroscopy analysis, electron microscopy, X-ray fiber diffraction, small-angle X-ray scattering, limited proteolysis, hydrogen/deuterium (H/D) exchange, and surface reactivity measurements, have led to several three-dimensional (3D) structure structural models of PrP^{Sc}. Here the frequently discussed models for the structure of PrP^{Sc} will be discussed.

The β-helix model is one of the most popular models that was proposed based on EM data on mouse brain-purified PrP^{Sc} (**Figure 1.5 A**). In this model, the prion N-terminal residues (~89–175) could get converted into a triangular β-helix containing four turns (four-rung model). In addition, they proposed that the β-helix associated with an intact *C*-terminal α2-α3 bundle, which retained its α-helical structure from the PrP^{C} fold [87]. Interestingly, the β-helical motif has been observed in other proteins that exhibit biochemical features reminiscent of PrP^{Sc}, such as partial resistance to protease degradation and aggregation propensity [88]. The fungal prion HET-s was shown to form a β-solenoid arrangement of β-sheets that is structurally similar to β-helices [89]. Remarkably, the C-terminal α-helices that are retained in a previous model are no longer supported by experimental data [86, 90].

The β-spiral was proposed by Daggett and colleagues based on molecular dynamics simulations of PrP conformational fluctuations under amyloidogenic conditions (acidic pH) (**Figure 1.5 B**). In this model, all three α-helices from the original PrP structure were retained, while the number of β-strands was extended to four. The model was characterized by a spiraling core of extended structure, consisting of three short β-strands (spanning amino acids 116–119, 129–132 and 160–164) and the recruitment of a nascent β-strand (amino acids 135–140). It was proposed that formation of β-strands involves the natively unfolded N-terminal region of PrP27-30, while the *C*-terminal α2 and α3 helices remained intact. From individual monomers a fibrillary model was build up, in which the β-strands are oriented at angles that are not perpendicular to the fibril axis. This model has the highest proportion of α-helical structure from all published models and one of the lowest β-sheets contents. Moreover, it does not feature a cross-β architecture, known experimentally to be a key characteristic of PrP^{Sc} fibrillar aggregates.

Cobb and colleagues proposed a parallel in-register β-sheet model, where the recPrP amyloid consists of β-strands and relatively short turns and/or loops with no residual α-helices (**Figure 1.5 C**). Furthermore, each molecule of PrP contributes only with 4.8 Å to the length of the amyloid fibril. The authors also postulate that the C-terminal region (amino acids 159–219 in mouse PrP) is converted to a hairpin structure and that the fibrils are formed as a long two-layered β-sheet. Although some researchers have adopted this model to explain the structure of PrP^{Sc} [91], this recPrP amyloid preparation has not been reported to produce infectivity and the model does not correlate with the repeating unit size of 19.2 Å observed by X-ray fiber diffraction experiments on PrP^{Sc} and PrP 27–30 [92].

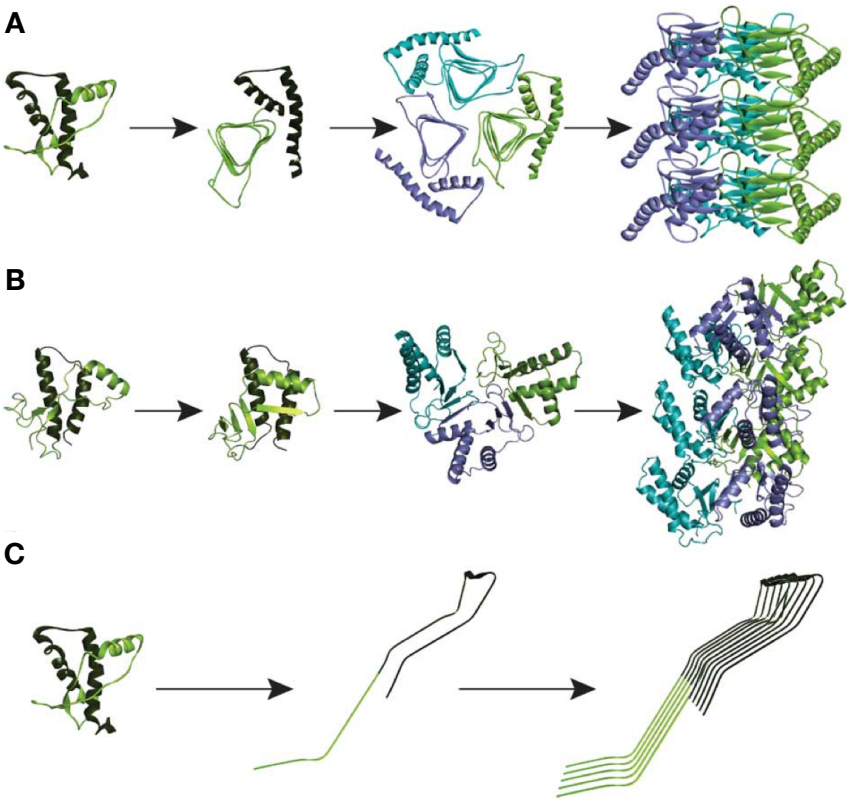

Figure 1.5. (**A**) The PrP^{Sc} monomer and the β-helical model. Residues ~90-175 are shown to form left-handed β-helices that associate into trimers, leaving the α-2 and α-3 helices of PrP^{C} intact. (**B**) In the spiral model the two native β-sheets elongate in a longer single β-strand, which forms intermolecular β-sheets with other PrP^{Sc} molecules. **(C**) Parallel and in-register β-structure model including a continuum of short β-strands from residue ~90 to the entire C-terminal region (modified from [26]).

X-ray diffraction data from both natural and synthetic prions were obtained [93], including the Syrian hamster (SHa) Sc237 PrP27-30 strain (SHaSc237), the mouse RML prion (MoRML), the mouse adapted synthetic prion (MoSP1), mouse truncated recombinant PrP(89-230) and truncated recombinant SHa(90-231) amyloids. Fiber diffraction patterns of SHaSc237, MoRML and MoSP1 exhibited a marked intensity maximum at 4.8 Å resolutions, confirming the presence of β-strands running perpendicular with respect to filament axis, typical for amyloid structures. Equatorial maxima, diminished in intensity with increasing resolution. Equatorial diffraction from natural brain isolates and synthetic prions also included an intense, moderately sharp, low-angle reflection (63.3 Å), characteristic of fibers with poorly ordered para-crystalline packing. These data are more consistent with β-helical model. Contrarily, diffraction patterns from both recombinant MoPrP(89-230) and recombinant SHa(90-231) showed a well-defined 4.8 Å meridional layer line, but with an equatorial broad maximum at 10.5 Å. This diffraction pattern is consistent with a stacked β-sheet structure for the major component of recPrP amyloids. These differences imply that recPrP fibrils do not have the same amyloid structure as

brain adapted prions. This structural information might also explain the substantial differences in their infectivity.

Recently, novel methods to obtain pure preparations of prions from mouse brain were developed, showing that pathogenic PrP in these preparations is assembled into rod-like assemblies. The infectious PrP rods have a common hierarchical assembly comprising twisted pairs of short fibres with repeating substructure [94]. Moreover, cryo-electron microscopy studies showed that a four-rung β-solenoid structure as a key feature for the architecture of infectious mammalian prions [95] and this feature is present in different infectious prions [96].

1.6 The species barrier and the prion strains

Transmission of prion diseases between different mammalian species is limited by the so called “species barrier” (Pattison IH 1966, Res Vet Sci). The prion species barrier occurs when prions from a donor species are transmitted to a different recipient species and can be characterize by extended incubation period before the onset of symptoms in the recipient species. If prions are then re-isolated from the recipient host and re-transmitted to another host of the recipient species, the incubation period decreases and the prions are “adapted”. For example, a prion species barrier occurs between mice and hamsters (**Figure 1.6 B**). Inoculation of hamster prions into mice did not elicit disease, nor did it cause an accumulation of PrP^{Sc} [97]. Samples of PrP^{Sc}-negative brain were then passaged one more time into mice, and this again did not cause clinical signs for >650 days. However, injection of the mouse brain samples into hamsters resulted in rapid lethality. This indicates that the agent had silently replicated for several years in mice, but maintained full infection potential towards hamsters.

The first experimental transmission of a TSE between species was performed with scrapie between sheep and goats in 1939, showing 100% susceptibility, suggesting that goats are highly susceptible. Then, further experiments were performed with other species to test their susceptibility to TSEs. These experiments revealed that some animals such as rabbits and guinea pigs display intrinsically very low susceptibility to prion infection [98] in contrast to other species such as hamsters and bank voles, which are unusually susceptible [99].

Identical animals infected with prions from different sources can develop varying pathologies, which upon passage to new hosts of the same species will maintain their biochemical properties and clinical outcomes. Infectious prions that present and maintain different pathologies when passaged to a new host are referred to as prion "strains" [100] (**Figure 1.6 A**).

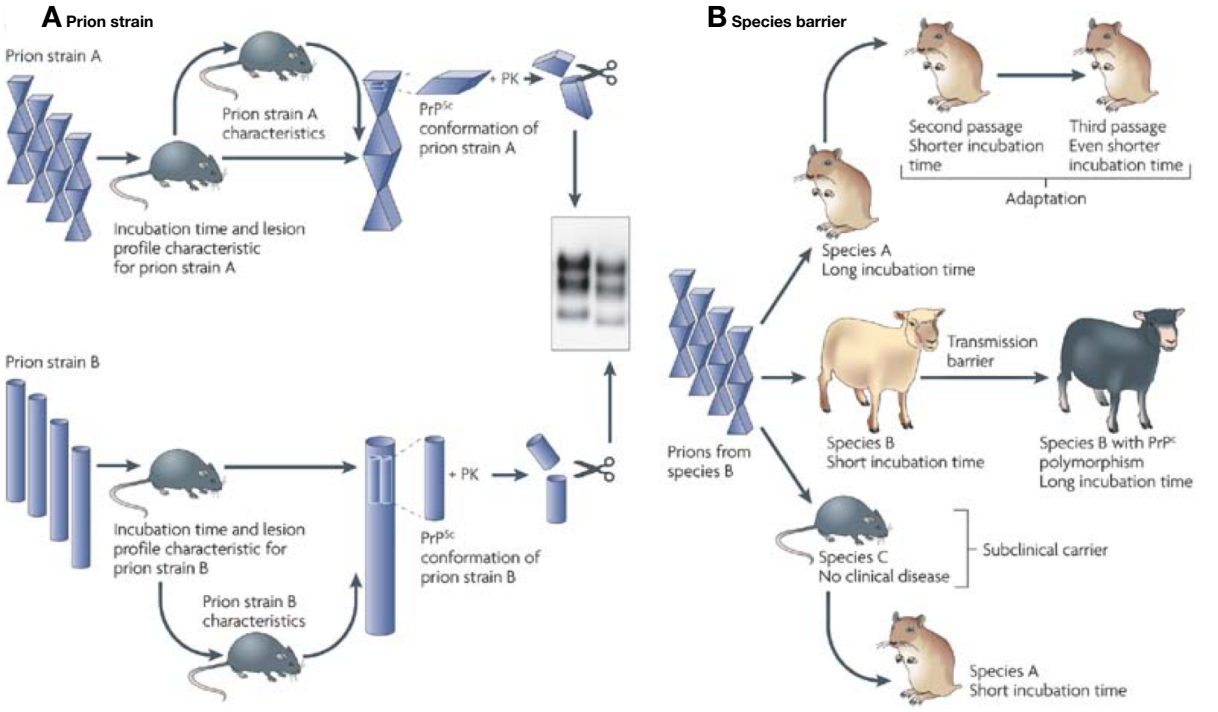

Figure 1.6. Prion species barriers and strain variation phenomena. (**A**) The transmission of different prion isolates (prion strain A and prion strain B) to identical hosts results in distinct disease phenotypes, such as incubation times. These features persist following serial passages to new hosts. In some cases, strains exhibit characteristic biochemical signatures such as electrophoretic mobility of the proteinase-K (PK)-resistant core. (**B**) Prions isolated from one species are often less infectious to other species, as evident by longer incubation times and reduced attack rates in these other species. After serial passages, incubation times gradually decrease (adaptation) (modified from [100]).

Prion strains are the result of alternative stable conformations of PrP^{Sc} that can be faithfully propagated in new hosts [101, 102]. The differences in these conformations result in differences in resistance to PK digestion and electrophoretic mobility after PK digestion [103, 104], varying glycosylation patterns [105], sedimentation velocities and resistance to urea and guanidinium hydrochloride denaturation [106].

The combination of different hosts and prion strains can also result in different pathologies and clinical symptoms. The most common variation between strains is in the time between inoculation and symptom onset, referred to as the incubation period, which is often reproducible within hosts of the same species [103, 107].

1.6.1 Structural variations of PrP^C between and within species

The overall architecture of PrP^C shares a very similar fold among mammals. However, structural variations among mammalian PrP^C are present. Local sequence and structure variations are most prominently localized at the interface between the β2-α2 loop (residues 165-175) and in the C-terminal part of α3 helix (residues 215-228) providing insights into a specific PrP^C regions that may control susceptibility or resistance to prion conversion.

The β2-α2 loop region has been identified as important element able to modulate the susceptibility of a given species to prion disease [25, 108-112].

While this loop is highly flexible in most species, it shows a well-defined conformation in the PrP structures of Syrian hamster [113], elk [114], bank vole [115], wallaby [116], rabbit [117] and horse [118] **(Figure 1.7)**.

In the NMR structure of the MoPrP, no resonances could be assigned for the residues of the β2-α2 loop, most probably due to conformational heterogeneity of this part of the protein chain [119], therefore it is believed to have a flexible β2-α2 loop. In contrast, in the NMR structure of PrP^C from Syrian hamster, the resonances for the loop residues could be clearly identified; residues 166-168 folded into a short 310-helix and amino acids 171-174 formed the first turn of α-helix 2 [113].

In the structure of elk PrP^C, the β2-α2 loop was clearly defined. Elk and deer are species susceptible to CWD; they are also quite unique in incorporating a threonine residue at position 174, which in most known sequences is an asparagine or, less commonly, serine. Mutating two residues in the mouse β2-α2 loop to mimic elk PrP resulted in a clearly defined "rigid" loop as observed in elk PrP. The great susceptibility of elk to CWD combined with the rigidity of the loop in its prion protein led to the hypothesis that structural homogeneity in the β2-α2 loop results in increased susceptibility to prion disease [114]. This hypothesis received support from an *in vivo* model in which the rigid loop mutant of mouse PrP was expressed in transgenic mice, which subsequently became highly susceptible to prion infection [120].

The structure of PrP^C from bank voles, a species extremely susceptible to prion diseases, also showed the β2-α2 loop in a clearly defined conformation [115], as for the Tammar Wallaby PrP^C, which also revealed that long-range contacts to the C-terminus of helix-3 may help to stabilize the β2-α2 loop [116].

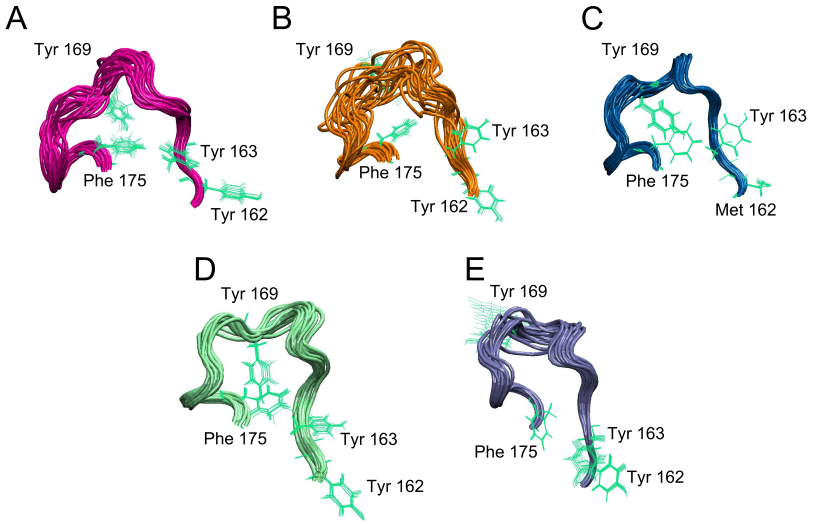

Figure 1.7. Backbone fold of residues 162-175 corresponding to the β2-α2 loop the in (**A**) human PrP^C (pdb id 1QM1), (**B**) ovine PrP^C ARR (pdb id 1Y2S), (**C**) tammar wallaby (pdb id 2KFI), (**D**) bank vole PrP^C (pdb id 2K56) and (**E**) human PrP^C, Q212P) (pdb id 2KUN).

Despite growing evidence that rigidity in the β2-α2 loop generally correlates well with susceptibility to prion disease there are also some exceptions. PrP^C from pigs and rabbits, which are quite resistant to infection, also have clearly defined β2-α2 loops [117, 121]. This finding, however, can still be accommodated in the framework of the conformational selection model when one replaces simple rigidity of the β2-α2 loop with the conformational subset available to it as the determinant of resistance and susceptibility. In support of this hypothesis, it has been found that amino acid identity at position 170 and its resulting conformational effects are determinant to inter-species transmission [122].

1.6.2. PrP^C polymorphisms within species

There are known polymorphisms in the primary PrP^C sequence of different mammalian species [123]. In sheep PrP^C amino acid polymorphisms at residues 136, 154 and 171 dictate the level of susceptibility or resistance to scrapie. For instance, the polymorphisms VRQ (V136, R154 and Q171) and ARQ (A136, R154 and Q171) render sheep more susceptible to scrapie, while ARR (A136, R154 and R171) and AHQ (A136, H154 and Q171) are considered protective polymorphisms [124, 125], although rare instances of infection have been reported [126]. During unfolding, all four variants formed an intermediate state rich in β-sheet structure. The activation energy for its formation was significantly higher in the resistant variants, ARR and AHQ, and accompanied by a lower β-sheet propensity when compared to the susceptible variants, VRQ and ARQ [127]. The crystal structures of the OvPrP variants [128] reveals that in OvPrP VRQ a hydrogen bond between the Q171 side-chain and residue R167 stabilizes the structure, when compared with OvPrP ARR (**Figure 1.8**).

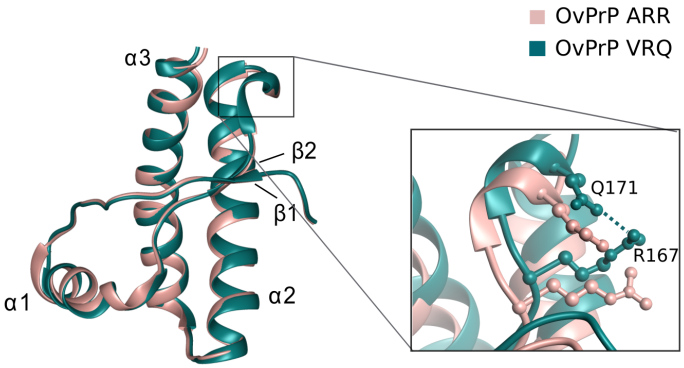

Figure 1.8. Comparison of the crystal structure of the globular domain of the ARR allele of sheep PrP (pink, pdb id 1Y2S) and VRQ (green, pdb id 1TQB). In the box, the hydrogen bonds between the Q171 side-chain and residue R167 is shown.

Another case of PrP^C amino acidic variations within a species effecting susceptibility to infection is the methionine/valine polymorphism at position 129 in the amino acid sequence of human PrP^C. During the BSE epidemic in the United Kingdom, all documented human cases of vCJD have been in individuals homozygous for methionine at residue 129 [129]. The presence

of methionine at position 129 results in increased susceptibility to prion disease, while the presence of valine at that position appears to be protective [130]. Polymorphism at residue 129 also modulates the conformational conversion of the D178N variant of human PrP, determining the development of either FFI (methionine) or familial CJD (valine) [131].

1.7 Defining the PrP^C function

PrP^C is a cell surface protein expressed in a variety of different organs and tissues with high expression levels. It is mainly known for its role in prion diseases, where its misfolding causes fatal neurodegenerative conditions.

A fully satisfactory understanding of the physiological function of PrP^C has been lacking for a long time. Putative roles for PrP^C are based on its localization in the central and peripheral nervous systems and on PrP^C-interacting molecules or metal ions [41].

1.7.1. Insights into the PrP^C function from PrP^C-null mice

Soon after PrP^{Sc} was proposed to be the causative agent of prion diseases, *Prnp* knockout mice were generated to assess whether the loss of physiological PrP^C function would led to neurodegeneration in prion diseases.

The first *Prnp* null mouse strain, $Prnp^{-/-}$, or Zurich I, was produced in a mixed C57BL/6J x 129/Sv(ev) background, by replacing of codon 4–187 with a neomycin phosphotransferase expression (neo) cassette [132]. A second line of PrP^C-deficient mice, known as Npu or Edimburgh (Edbg), was produced by interruption of the *Prnp* ORF at position 93 and introduction of a neo cassette [133]. In a first round of characterization, these mice were not found to show any clear abnormality expect for their resistance to prion infection thus proving that PrP^C is an absolute requirement for developing TSEs.

In contrast with these earliest lines, PrP^C-deficient mice from which the entire *Prnp* gene was removed develop progressive cerebellar ataxia, which initially was attributed to the loss of PrP^C, since the observed phenotype was abolished by reintroduction of PrP^C. [134, 135]. Later, it was discovered that this phenotype was due to the deletion of a splice acceptor site in exon 3 of *Prnp*. This led to aberrant overexpression of PrP paralogue gene encoding Doppel (Dpl), causing neurodegeneration of cerebellar Purkinje cells. Although ZrchI and Edbg mice did not present any obvious physiological abnormalities, these mice lines provided a platform for experiments aimed at gaining further insight on the role of PrP^C in the context of behavior, sleep-wakefulness cycle, memory, synaptic activity and neuronal excitability.

Immunocytochemical studies showed that PrP^C is enriched along axons and in pre- and postsynaptic terminals [136, 137] and that it undergoes anterograde and retrograde axonal transport. Recently, it has been shown that sialic acid within GPI-anchor is important for targeting PrP^C to synapses. These observations suggest a role of PrP in preserving normal synaptic structure and function by regulating synaptic transmission and plasticity; indeed, synaptic dysfunction and synaptic loss are early event in prion diseases [138].

Long-term potentiation (LTP) correlates with synaptic plasticity, which underlies learning and memory formation in the hippocampus. Thus, any LTP deficits may results in cognitive defects. Even if initial studies did not report any reduction in memory performance in mice Zurich, a later study found deficiencies in spatial learning and memory in PrP^C-deficient mice. These data are in contrast with another study carried out in *Prnp* ZH1/ZH1 mice that did not reveal any memory impairment. Thus, a role for PrP^C in memory is still contentious.

A role of PrP^C in sleep homeostasis and sleep continuity has also been proposed [139]. It would explain the disruption of sleep occurring in some forms of prion diseases (*i.e.* sporadic and familial fatal insomnia). Nonetheless, the molecular bases of sleep regulation are not completely understood. Recent work indicates that calcium-dependent hyperpolarization is critical to sleep duration, and that sleep deterioration is associated with impairment of calcium-dependent potassium channels, voltage-gated calcium channel (VGCC) and N-methyl-D-aspartate (NMDA) glutamate receptors. One of the most detailed functional studies recently published deals with the involvement of PrP^C and copper ions in NMDAR S-nitrosylation and activity. By exploiting PrP knockout mice, the authors showed that the depletion of PrP^C is associated with a reduction in the S-nitrosylation of the 2 NMDAR subunits GluN2A and GluN1, while not affecting the levels of the corresponding proteins at the synapse [41, 140].

1.7.2. PrP^C functions suggested by interaction partners

To gain deep insight into the function of PrP^C many proteins that interact and bind to PrP^C have been identified. Most of them have been identified as potential PrP^C-binding partners by using many different methods, such as yeast two-hybrid screening, co-immunoprecipitation and cross-linking. The functional relevance of the binding has been proved only for very few PrP^C ligands, including the stress-inducible protein I (STI1), the 37-kDa/67-kDa laminin receptor precursor (LRP), and the neuronal cell adhesion molecule (NCAM).

STI1 is a heat shock protein first described in a macromolecular complex with Hsp70 and Hsp90 chaperone family proteins, mainly localized in the cytoplasm but a small fraction of the total protein is present at the cell membrane, where it seems to interact with PrP^C [141]. The interaction between STI1 and PrP^C induces neuroprotective signals that rescue cells from apoptosis *via* cAMP/protein kinase A and the Erk signaling pathways [142].

LRP is another cell surface PrP^C ligand. It mediates internalization of PrP^C and directs the complex through clathrin coated pits. LRP was suggested to act as a putative PrP^C receptor because it was shown to co-localize with PrP^C on the surface of both N2a and baby hamster kidney cells.

NCAM belongs to immunoglobulin (Ig) superfamily cell adhesion molecules (CAMs) and it is present on the cell surface of neurons, astrocytes and oligodendrocytes, where it mediates homophilic and heterophilic cell adhesion [143]. NCAM is involved in neuronal migration, axon growth and guidance, as well as in synaptic plasticity associated with learning and memory [144]. Alternative splicing of the *NCAM1* gene results in isoforms of three size classes, that differ in their membrane attachment and cytosolic regions (namely, NCAM120, NCAM140 and NCAM180), but share an extracellular domain consisting of five Igs and two fibronectin type-3

(FNIII1,2) domains (**Figure 1.9 A**). Variable use of alternative exons in the extracellular domain results in small insertions into Ig4 or between the FNIII1,2 domains.

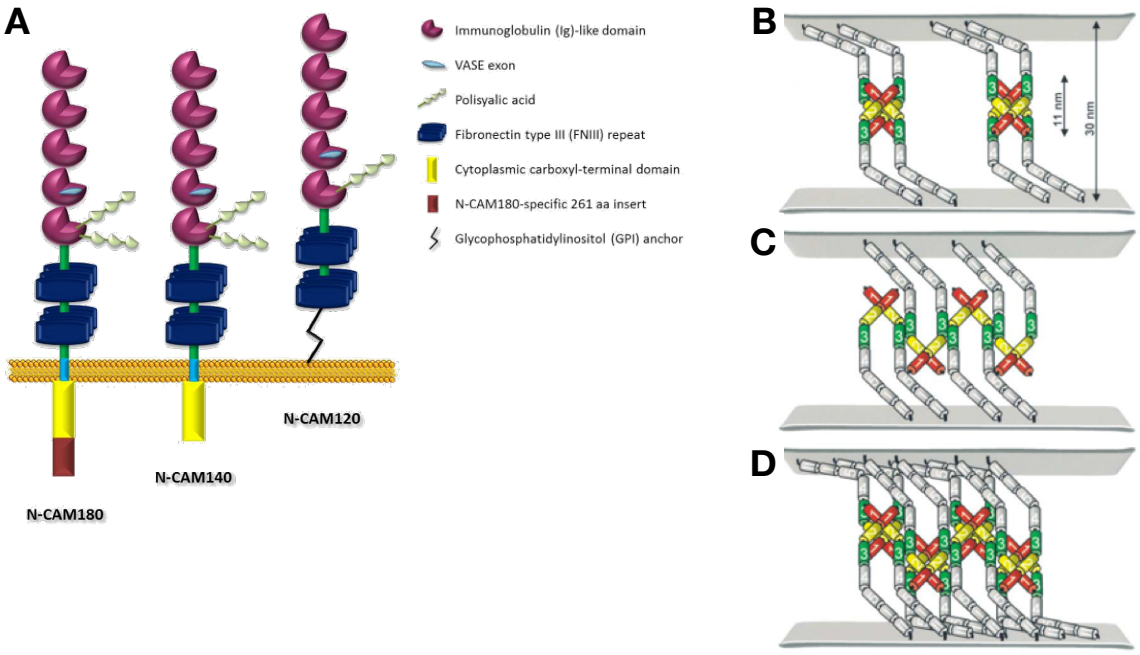

Figure 1.9. (A) Schematic drawing of three NCAM isoforms. **(B)** Schematic representations of the zipper adhesion complexes formed by NCAM. The compact zippers are stabilized by Ig1-to-Ig3 and Ig2-to- Ig2 interactions between Ig1-2-3 *cis* dimers originating from two opposing cell membranes. **(C)** The flat zipper is stabilized by Ig2-to-Ig3 interactions between Ig1-2-3 *cis* dimers originating from two opposing cell membranes. **(D)** The two types of zippers may coexist as observed in the crystal and will result in formation of a double zipper-like adhesion complex (modified from [145]).

NCAM function is further regulated by an unusual posttranslational modification consisting in the addition of polysialic acid to Ig5 [146, 147].

NCAM physiological function is mediated by multiple modes of homophilic interaction through NCAM Ig domains [145]. The Ig1 and Ig2 domains mediate dimerization of NCAM molecules situated on the same cell surface (*cis* interactions), whereas the Ig3 domain mediates interactions between NCAM molecules expressed on the surface of opposing cells (*trans* interactions) through simultaneous binding to the Ig1 and Ig2 modules. This arrangement results in two perpendicular zippers forming a double zipper-like NCAM adhesion complex (**Figure 1.9 B-D**).

Additionally, NCAM is also engaged in heterophilic interactions, *i.e.* NCAM can bind other protein partners modulating different functions. Different groups have deeply investigated the structural and molecular basis governing the interaction between the NCAM FNIII1,2 domain and the fibroblast growth factor receptor 1 (FGFR1) [148, 149].

Besides the interaction with FGFR1, NCAM can bind PrP^C and engages different cellular responses. This part will be discussed in more detailed in the following section.

1.7.2.1. Biological relevance of PrP^C-NCAM interaction

PrP^C has been first identified in a complex with NCAM by chemical cross-linking [150]. Both PrP^C and NCAM have been implicated in signaling cascades involving the $p59^{fyn}$ non-receptor tyrosine kinase (fyn) [151] and fyn is involved in NCAM-induced neurite outgrowth [152]. PrP^C and NCAM in cultured hippocampal neurons were found to co-localization along neurites and in growth cones [153].

PrP^C accumulates in lipid rafts enriched in fyn (**Figure 1.10 A**). NCAM binds to RPTPα outside of lipid rafts, activating fyn, and therefore it is excluded from lipid rafts. Clustering of NCAM results in its palmitoylation that redistributes NCAM to lipid rafts [154]. In lipid rafts, *cis* interactions between NCAM and PrP^C further recruit and stabilize NCAM in lipid microdomains activating fyn *via* NCAM, and finally resulting in neurite outgrowth.

In NCAM-deficient and PrP^C-deficient neurons, NCAM/PrP^C-dependent neurite outgrowth is arrested, indicating that PrP^C is involved in nervous system development cooperating with NCAM as a signaling receptor (**Figure 1.10 B-C**).

Enzyme-linked immunosorbent assay (ELISA) experiments using an NCAM-derived peptides library against the recombinant full-length MoPrP have shown that FNIII1,2 domain shares highest affinity for MoPrP [155]. N2a cells expressing a MoPrP deletion mutant, including residues from 144 to 173, did not form cross-linking with NCAM, suggesting that the interaction between PrP^C and NCAM occurs through this amino acidic region.

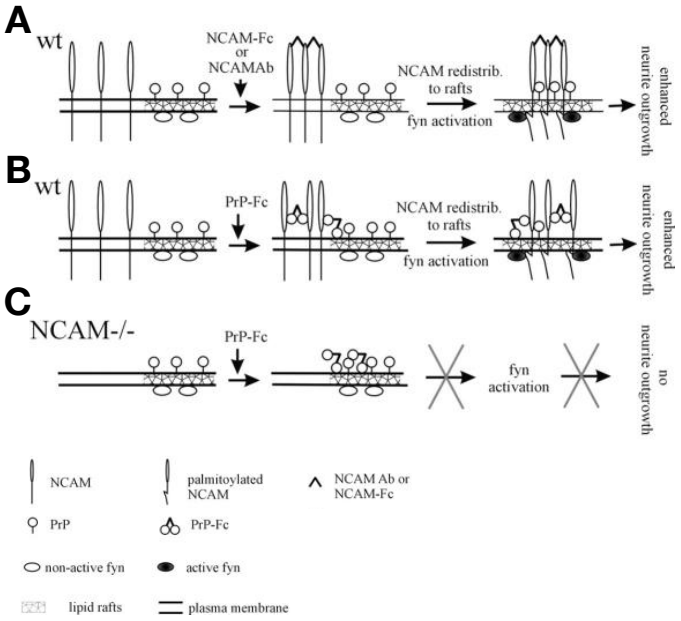

Figure 1.10. Signals cascade following the interaction between NCAM and PrP^C (modified from [153]).

1.7.3. PrP^C functions suggested by metal interaction

Many efforts have been made to understand the role of metal ions in both PrP^C physiology as well as in prion pathogenesis. To date, evidences support the idea that the physiological function of PrP^C is related to its metal-binding properties. PrP^C binds copper *in vivo*, and cultured cells and neurons chronically exposed to high Cu^{2+} concentrations show increased expression of *Prnp*. Moreover, it has been shown that copper stimulates rapid endocytosis and trafficking of PrP^C, through binding to the octapeptide region (OR) region [17].

PrP^C takes up the Cu^{2+} through its flexible N-terminal domain, composed of five copper binding sites in this domain: four in the OR and one in non-octapeptide region (non-OR region) or fifth copper binding site [156].

The OR is an evolutionarily conserved motif, although the number of the repeated units can vary among species (**Figure 1.11 A**). In HuPrP the OR consists of one nonapeptide, PQGGGGWGQ and four repeats of the sequence PHGGGWGQ. Within the OR, histidine and tryptophan residues were found to be essential for the binding of copper and other divalent cations such as zinc, nichel, iron and manganese [157], but the highest affinity is for Cu^{2+} (around 5-8 μM) [74]. In a single octapeptide the binding is mediated by the histidine and tryptophan which form a β-turn conformation wrapped around and coordinating Cu^{2+} (**Figure 1.11 B**) [158]. The OR does not appear to be essential for prion infectivity [159]. However, the insertion of extra octapeptide repeats is related to inherited forms of prion diseases [160, 161] suggesting that the OR may play a role in modulating the conversion of the protein into the pathogenic form. The binding of Cu^{2+} suggests that PrP^C may be involved in copper homeostasis.

Figure 1.11. **Schematic representation of PrP^C and its Cu(II) binding sites.** (**A**) A sequence alignment for the Cu binding regions is shown including sequences from different mammalian prion proteins (PrP): HuPrP (human, Homo sapiens, NCBI accession code AAA60182), MoPrP (mouse, Mus musculus, AAA39997), SHaPrP (Syrian hamster, Mesocricetus auratus, AAA37091) and OvPrP (sheep, Ovis aries, AFM91142.1) (modified from [162]. (**B**) X-ray crystal structure of the Cu^{2+}-HGGGW complex (modified from [163]).

Additional histidines at position 96 and 111 are involved in high affinity copper binding and form the non-OR, or fifth, copper binding site [164, 165]. This region seems critical for prion conversion. However, animals treated with excess of copper [166] or with metal chelators [167] in both cases displayed a delayed onset of disease symptoms. These data indicate that there is no consensus and, often, contrasting results regarding the specific physiological function of copper binding, as well as the implication of this metal in developing prion diseases.

1.7.3.1. The binding of copper at the octapeptide repeats binding sites.

The OR region in human prion protein is composed of highly conserved multiple tandem repeats of the same eight amino acids (PHGGGWGQ). This region can bind four copper ions with identical coordination geometry [168, 169]. Each repeat contains a histidine which is generally accepted to be the primary residue responsible for the copper coordination [158, 170].

At pH 7.4, the copper coordination to the octapeptide repeat region is dependent on the relative amount of available copper and on the pH of the surrounding environment [163, 170] (**Figure 1.12**).

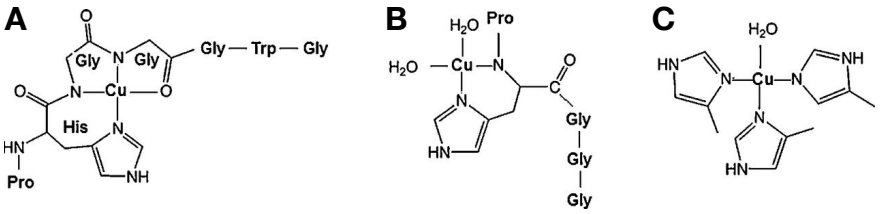

Figure 1.12. Models of the three coordination modes of copper binding to the octarepeat region. (A) Component 1, (B) component 2 and (C) component 3 (modified from [171]).

At low copper occupancy, a single Cu^{2+} ion is bound by the imidazole side chains of four OR histidine residues in a square planar geometry. This multi-His coordination mode is commonly referred to as component 3 (**Figure 1.12 C**), with a dissociation constants ranging from ~0.1 to 10 nM [172, 173]. As the copper-to-protein ratio is increased, OR binding transitions through an intermediate two-His binding mode (component 2) (**Figure 1.12 B**) to a high-occupancy structure in which each individual repeat of PHGGGWGQ coordinates a single Cu^{2+} ion. This high-occupancy binding mode, known as component 1 (**Figure 1.12 A**), coordinates copper through the imidazole nitrogen of histidine, the backbone amide nitrogens from the first and second glycines immediately following the histidine, and the carbonyl oxygen of the second glycine [158, 174].

1.7.3.2. The binding of copper at non-octapeptide repeat binding site

Several studies have shown that copper is able to bind outside of the octarepeat region of PrP^C [158, 161, 165]. Jones and co-authors discovered a multi-co-ordination mode that was strongly influenced by pH. They found three coordinations, all of them display a square planar geometry (**Figure 1.13**). At pH 7.5 and above, a 4N complex dominates, while at pH 6.0, a ligand rearrangement shifts the coordination to a 3N1O configuration. At low pH, a multi histidine residue 2N2O coordination dominates [171].

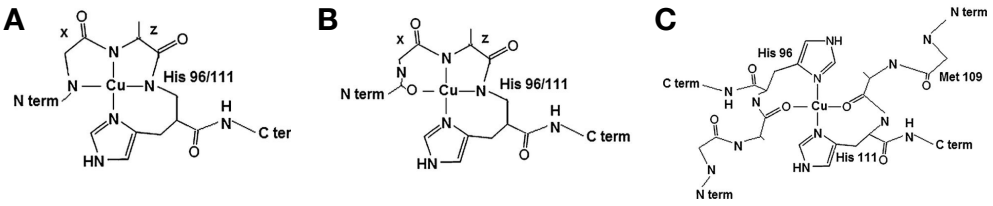

Figure 1.13. Models of the Cu^{2+} coordination modes in the non-octapeptide repeat site. (A) Component 1 is a 4N complex that dominate at pH 7.5 and above, **(B)** Component 2 is a 3N1O complex that exists at pH 6, **(C)** Component 3 is a 2N2O complex that may exist at pH 5.5 (modified from [171]).

1.8 The role of the N-terminal domain in the PrP^C function and conversion

As anticipated, PrP^C consists in two distinct structural moieties: a flexible and disordered N-terminal tail and the globular C-terminal domain. Several studies suggest that the N-terminal domain may act as a molecular sensor that allow PrP^C to relay intracellular neuroprotective signals, but can also modulate prion conversion, being a target of the most effective antiprion compounds.

Both the N- and C-terminal domains may also be physically divided following a proteolytic processing of PrP^C in a region termed "α-cleavage" releasing PrPN1 and PrPC1 [175]. A minor cleavage termed "β-cleavage" also occurs at residues 90–91, releasing peptides PrPN2 and PrPC2 [176]. Interestingly, this cleavage is up-regulated in TSE [175]. Another type of cleavage within the OR is induced by reactive oxygen species in the presence of Cu^{2+} [177]. The cleavage of PrP^C may regulate the function of the protein in at least two ways; inactivation of existing functions as well as unmasking new activities.

Several evidences pointed out that N- and C-terminal domain may be physiologically connected. It was proposed that the C-terminal domain act as a molecular regulator of the N-terminal domain. Indeed, mAb binding at specific epitopes in the globular domain disrupts the normal regulation, leading the N-terminal domain to carry out toxic effects. Deletion of N-terminal segments rescue the normal functions. It has been proposed that this coupling is due to a direct interaction between the C- and N-terminal domain. In support to this hypothesis, EXAFS studies on the human pathological point mutation, Q212P -which is located in the globular domain- shown that the mutation alters the coordination geometry of the non-OR region in the N-terminal, supporting the involvement of both C- and N-terminal domain [164].

Recently, NMR and electron paramagnetic resonance (EPR) spectroscopy studies revealed that interaction between C- and N-terminal domain is mediated by copper ions. In this study there were identified the residues in the globular domain involved in the interaction, but not residues of the N-terminal domain because of the high flexibility [178].

Other studies highlighted that in contrast to most GPI-anchored proteins, the PrP^C's GPI anchor does not seem to have a predominant control on PrP^C internalization. Several studies have shown that N-terminal domain is necessary and sufficient for constitutive endocytosis of PrP^C *via* clathrin-coated pits in primary neurons and a variety of cell lines [17, 179, 180].

The N-terminal domain is also essential for the movement of PrP^C outside of lipid rafts before its internalization. In the absence of a transmembrane domain, PrP^C cannot directly interact with cytoplasmic clathrin-associated adaptor protein complexes.

1.8.1. The neuroprotective role of the PrP^C hydrophobic domain

Several mouse models have demonstrated the neuroprotective role of PrP^C hydrophobic domain (HD). Ataxia and degeneration of cerebellar granule neurons occurred in transgenic mice expressing a PrP construct deleted of residues 32–121 or 32–134 [181]. Mice expressing a PrP construct with shorter deletions (*i.e.* D32-80, D32–93, D32–106, or D23–88) did not display neurological symptoms [182]. These results showed a correlation between the absence of the HD (amino acids 112–133) and toxicity of the transgene.

Transgenic models also showed that the HD is required for myelin maintenance. Selective depletion of PrP^C from neurons but not from Schwann cells results in chronic peripheral demyelinating polyneuropathy in mice [183].

Prnp$^{-/-}$ mice displayed three times larger infarct size compared with *Prnp*$^{+/+}$ mice [184]. Mice expressing a PrP^C mutant deleted of amino acids 32–93 had infarct size similar to *Prnp*$^{-/-}$ mice, indicating a neuroprotective function for this domain *in vivo*.

A transgenic mouse model indicated that PrP^C neuroprotective domain maps to amino acids 23–88 [182, 185]. In addition, fusion of N-terminus of PrP^C (amino acids 1–133) to Doppel completely reversed Doppel toxicity in a transgenic mouse [185]. The anti-Doppel activity of PrP^C N-terminal domain 23–90 was also confirmed in SH-SY5Y cells [186].

Amyloid precursor protein (APP) cleavage initiates the production of Aβ and is considered as one of the key molecular events in Alzheimer's disease. Removal and over-expression of PrP^C in SH-SY5Y cells increased and decreased β-secretase cleavage of APP respectively [187]. In a model proposed by the authors, GAGs connect PrP^C to β-secretase and prevent the protease from accessing APP [187, 188]. *In vivo*, APP and Aβ levels do not depend on the presence of PrP^C and a role for PrP^C in APP metabolism seems therefore unlikely [189].

1.8.2. The neurotoxic role of the N-terminal domain of PrP^C

The interaction between Aβ oligomers and PrP^C suggested that PrP^C may act as a receptor and mediates oligomer-induced synaptic toxicity. Indeed, addition of synthetic Aβ42 oligomers to hippocampal slices from *Prnp*$^{+/+}$ but not *Prnp*$^{-/-}$ mice reduced LTP [190]. Subsequently, it has been shown that absence of PrP^C in a transgenic Alzheimer mouse rescues deficits in spatial learning and memory, confirming the role of PrP^C as a mediator of Aβ toxicity [189]. Aβ42 oligomers inhibited the constitutive endocytosis of PrP^C in cultured cell lines and hippocampal neurons, resulting in a large increase of PrP^C at the cell surface within minutes after addition of oligomers [191]. This inhibition likely results from the binding of Aβ42 oligomers to the N-terminal domain and interference with the endocytic signal peptide. Thus, the N-terminal domain of PrP^C may act as a general receptor for toxic β-sheet conformers [192].

1.8.3. The role of the N-terminal domain of PrP^C in prion conversion

Although the region comprising the OR region is not essential for prion replication, its deletion results in extended incubation times and altered manifestations in the pathology in animals experimentally inoculated with mouse adapted scrapie prions [181].

Two mouse models with point mutations within the N-terminal domain confirmed the importance of this region for prion conversion. First, a two amino-acid substitution at amino acids 108 (leucine to methionine) and 111 (valine to methionine) were associated with a prolonged incubation time in mice challenged with four different strains of murine prions [193]. Second, a single amino-acid substitution from proline to leucine at position 101 considerably altered prion incubation time and targeting of the brain pathology after challenge with prions from murine, hamster, sheep and human sources [193, 194]. Experiments performed with recombinant PrP constructs and in persistently infected cultured cells strengthened the significance of the N-terminal domain of PrP^C in prion conversion. Deletions of amino acids 34–94 and 34–113 inhibited the formation and altered the conformation of hamster PrP^{Sc} in a cell-free conversion assay [195]. Deletion of amino acids 95–107 and 112–119 also prevented the formation of PrP^{Sc} in ScN2a cells [32, 196].

In cell-free conversion assays, conversion of PrP^C into PrP^{Sc} is stimulated by heparan sulphates and heparin sulphate proteoglycans [197, 198]. In particular GAGs might act as a polyanionic scaffold facilitating the interaction between PrP^C and PrP^{Sc} [199]. Interestingly, the N-terminal domain of pathological mutants of PrP have a more exposed N-terminus and display enhanced heparin binding [28]. Mutants also formed aggregates more readily than wild-type PrP^C, suggesting that GAGs participate in prion conversion.

The N-terminal domain is also a site for several ligands with antiprion activites. One important class are heparan sulphate proteoglycans. Heparan sulphate mediates direct interactions of proteoglycans with proteins, including PrP^C N-terminus, promoting the association of PrP with lipid rafts and enhancing the conversion in prion infected N2a cells [200]. Moreover, sulphated GAGs enhance internalization of PrP^C in cultured cells, which may explain their inhibitory effects on prion conversion in cultured cells [179, 200].

Degenerate phosphorothioate oligodeoxynucleotides are also considered inhibitors of PrP^{Sc} in prion-infected N2a [199]. Several studies suggest a common mechanism of action of the most effective antiprion compounds in the N-terminal domain. Anionic antiprion molecules may interact with cationic amino acids and planar aromatic molecules could interact with the repeated tryptophan residues and bridge several PrP^C molecules. After clustering and/or internalization, PrP^C becomes unable to convert into PrP^{Sc}.

1.9 Aims of the research

The conversion of the cellular prion protein PrP^{C} into the infectious isoform (PrP^{Sc}) is the key event in prion diseases. The physiological role of PrP^{C}, as well as the structural and molecular mechanisms leading to PrP^{Sc} conversion, remains largely unknown. Putative roles for PrP^{C} are based on its localization in the central and peripheral nervous systems and on PrP^{C}-interacting molecules or metal ions.

In the present thesis, the interactions of the cellular prion protein with NCAM and copper ions have been investigated in the context of their functional role. In particular, objects of this thesis are:

i. Identification of the structural determinant responsible for the interaction between PrP^{C} and NCAM.
   Despite the inherent structural disorder of the PrP^{C} N-terminal domain, which can mediate interaction with both metals and cellular polyanions (*e.g.* sulfate proteoglycans), the binding with physiological protein partners has not been proved yet.
   Cell biology, biophysical and structural investigations on the interaction between NCAM and HuPrP were performed, providing the first structural evidence of the interaction between PrP and NCAM.

ii. Understanding the role of copper in prion conversion and susceptibility with a special focus on the fifth copper binding site.
   The molecular mechanisms of prion conversion are still debated [201]. NMR-based studies on HuPrP and mouse PrP (MoPrP) globular domains have identified the β2-α2 loop as important element able to modulate the susceptibility of a given species to prion disease [25, 108-112]. However, recent studies have highlighted also the importance of the N-terminal region in promoting structural rearrangements to PrP^{Sc}. The segment from residues 90 to 127 may act as an alternate N-terminal switch for prion conversion because of the ability of a palindromic motif AGAAAAGA (residues 113-120) to initiate β-sheet enrichment [40] and to form neurotoxic species [196, 202, 203]. The proximity of the non-OR copper binding site to this palindromic motif suggests a pathological link between copper binding to this site and prion conversion.

CHAPTER II

MATERIAL AND METHODS

2.1 STED nanoscopy experiments

Note: STED microscopy was performed at the NanoBiophotonics Department (Max Plank Institute for Biophysical Chemistry, Göttingen, Germany) and analyzed by Dr. Ladan Amin (SISSA). For this reason, we have moved the related Materials and Methods in the **Appendix II, Section I**.

2.2 Molecular biology experiments

2.2.1 Cloning of MoPrP and HuPrP in pET-11a vector

The pET-11a vector expressing the MoPrP(23-230) were kindly provided by the group of Prof. Jesús Requena (Universidade de Santiago de Compostela, Spain).

The WT MoPrP(89-230) was amplified from genomic murine DNA by PCR using primers 5' –GGA ATT CCA TAT GGG CCA AGG AGG GGG TAC CCA T- 3' and 5' –TCA GCT GGA TCT TCT CCC GTC GTA ATA GGC CGG ATC CCG- 3'.

The WT HuPrP(23-231, M129) was amplified from pGEM-T Easy vector::HuPrP complete ORF by PCR using primers 5' – GGA ATT CCA TAT GAA GAA GCG CCC GAA GCC TGG A- 3' and 5' –CGG GAT CCC TAG CTC GAT CCT CTC TGG TAA TAG GCC TGA- 3'.

The WT HuPrP(90-231, M129) was amplified from genomic human DNA by PCR using primers 5'-GGA ATT CCA TAT GGG TCA AGG AGG TGG CAC CCA C-3' and 5'-CGG GAT CCC TAG CTC GAT CCT CTC TGG TAA TAG GCC TGA-3'.

The WT HuPrP(23-144, M129) was amplified from pET-11a::HuPrP (23-231, WT) by PCR using primers 5' –TTT CGG CAG TGA CTA AGA GGA CCG TTA CTA T- 3' and 5' –ATA GTA ACG GTC CTC TTA GTC ACT GCC GAA A- 3'.

The DNA product was then inserted into pET-11a vector (Novagen) using NdeI and BamHI restriction sites. The PCR were performed using the Vent (New England Biolab) DNA polymerase according to manufacturer's instructions. Plasmid DNA was purified using the QIAprep Spin Miniprep Kit (Quiagen). The cloned DNA sequences were verified by sequencing.

Peptides HuPrP (23-89), HuPrP (23-50), HuPrP (60-68), HuPrP (93-114), HuPrP (93-114, P102L) used for NMR experiments were purchased from Chematek Spa.

2.2.2 Cloning of FNIII1,2, FNIII1 and FNIII2 in pET-11a vector

The FNIII1,2, FNIII1 and FNIII2 domains were PCR amplified from pCEP-Pu vector encoding for FNIII1,2 (kindly provided by Dr. Federico Carafoli, Imperial College London, London, UK) and inserted into a modified pET11a vector (i.e. carrying a C-terminal uncleavable HisTag) using restriction free cloning protocol. Our FNIII1,2 and FNIII1 numbering schemes correspond to Carafoli et al. 2008 [204].

2.2.3 Cloning of OpPrP, BvPrP and OvPrP in pET-11a vector

The pET-11a vector expressing the OpPrP (100-237), BvPrP (91-231), OvPrP (93-233, VRQ) and OvPrP (93-233, ARR) were purchased from Chematek Spa.

2.2.4 Mutagenesis of HuPrP and MoPrP constructs

The WT HuPrP(90-231, M129) was amplified from genomic human DNA by PCR using primers 5'-GGA ATT CCA TAT GGG TCA AGG AGG TGG CAC CCA C-3' and 5'-CGG GAT CCC TAG CTC GAT CCT CTC TGG TAA TAG GCC TGA-3'. The DNA product was then inserted into pET-11a vector (Novagen) using NdeI and BamHI restriction sites.

The PCR were performed using the Vent (New England Biolab) DNA polymerase according to manufacturer's instructions. Plasmid DNA was purified using the QIAprep Spin Miniprep Kit (Quiagen). The cloned DNA sequences were verified by sequencing.

The HuPrP and MoPrP variants were constructed using the QuikChangeTM kit (Stratagene) according to manufacturer's instructions. Q212P and P102L mutations were inserted on HuPrP(90-231) construct. H60Y, H68Y, H76Y and H84Y were inserted into pcDNA::MoPrP(1-254)WT, pcDNA::MoPrP(1-254)WT3F4 or pET::MoPrP(23-230). We used the following primers for the mutagenesis:

Q212P mutation: 5'-CGC GTG GTT GAG CCG ATG TGT ATC ACC C- 3' and 5'-GGG TGA TAC ACA TCG GCT CAA CCA CGC G- 3'.

P102L mutation: 5'-ACA GTC AGT GGA ACA AGC TGA GTA AGC CAA AAA CCA A-3' and 5'-TTG GTT TTT GGC TTA CTC AGC TTG TTC CAC TGA CTG T- 3'.

H96Y mutation: 5'-CAA GGA GGG GGT ACC TAT AAT CAG TGG AAC AAG C-3' and 5' –GCT TGT TCC ACT GAT TAT AGG TAC CCC CTC CTT G- 3'.

H60Y mutation: 5' –CAG CCC TAC GGT GGT GGC TGG GGA CAA- 3' and 5' -TTG TCC CCA GCC ACC ACC GTA GGG CTG- 3'.

H68Y mutation: 5' –GGG GAC AAC CCT ATG GGG GCA GCT GG- 3' and 5' – CCA GCT GCC CCC ATA GGG TTG TCC CC- 3'.

H76Y mutation: 5' –AGC TGG GGA CAA CCT TAT GGT GGT AGT TGG G- 3' and 5' – CCC AAC TAC CAC CAT AAG GTT GTC CCC AGC T- 3'

H84Y mutation: 5' –TGG GGT CAG CCC TAT GGC GGT GGA TGG- 3' and 5' –CCA TCC ACC GCC ATA GGG CTG ACC CCA- 3'.

All the constructs were verified by sequencing.

2.3 Protein expression and inclusion bodies isolation

2.3.1 Prion proteins expression in LB medium.

For recombinant proteins expression we always used *Escherichia coli* BL21(DE3) strain (Stratagene). For all recombinant MoPrP and HuPrP variants and OpPrP, BvPrP and OvPrP constructs we always used *Escherichia coli* BL21(DE3) strain (Stratagene) and produced in LB medium (10 g trypton, 5 g yeast extract, 10 g NaCl) according to the following protocol: freshly transformed 100 mL overnight culture of *E. coli* BL21 (DE3) cells was added to 2 L of LB medium plus ampicillin (100 μg/mL) in a Biostat B plus 2 L bioreactor (Sartorius) which allows for an automated control of pH, temperature and pO2. The expression was induced at 0.8 OD_{600} with 1 mM IPTG. The cells were harvested 16 hours after induction by centrifugation at 4000 g, 4 °C for 30 min.

2.3.2 FNIII1,2, FNIII1 and FNIII2 expression for NMR structural studies.

For double labeled recombinant proteins expression, the cultures were grown in M9 minimal medium (MM) using the recipe described by [205]. We have expressed our proteins using the 2 L bioreactor (Sartorius Biostat-B plus), as for the PrPs.

Small scale expression trials, aimed at increasing the FNIII expression level in M9 MM, included the following conditions: different concentrations of the inducer isopropyl β-D-galactopyranoside (0.4, 0.6, 0.8 and 1 mM IPTG) and two temperature conditions (30 and 37°C). For isotope labeling, 4 g/L [$^{13}C_6$] glucose and 1 g/L [^{15}N] ammonium chloride were added.

The final protocol for the large scale expression of double labeled ^{13}C,^{15}N FNIII1,2, FNIII1 and FNIII2 was the following: freshly transformed 100 mL overnight culture of *E. coli* BL21 (DE3) cells was pelleted by centrifugation at 4000 g, 4°C for 30 min. Bacterial pellet was resuspended with 50 mL double labeled M9 MM and added at 37°C to 2 L of M9 MM plus ampicillin (100 μg/mL). At 0.8 OD_{600} expression was induced with IPTG to a final concentration of 0.25 mM. The cells were harvested 12 hours after induction and the bacteria were pelleted by centrifugation at 4000 g, 4°C for 30 min.

2.3.3 Isolation of inclusion bodies

The overexpression of all our proteins in *E. coli* BL21 (DE3) resulted in the formation of insoluble bacterial inclusion bodies. We developed a common inclusion bodies extraction protocol. Bacterial paste was resuspended in 25 mM Tris-HCl, 5 mM EDTA, 0.8% TritonX-100, 1 mM PMSF, pH 8 and lysed at RT by French press (EmulsiFlex-C3). Three cycles of mechanical lysis at 100 MPa were sufficient to disrupt the cells. Inclusion bodies were separated by centrifugation (30 min, 10,000 g at 4°C), rinsed in 25 mM Tris-HCl, 5 mM EDTA, 0.8% TritonX100, pH 8, and then in bi-distilled water several times. Pure inclusion bodies were solubilized 12 hrs at 37°C in 5 volumes of 8M GndHCl, and then centrifuged 30 min, 10000 g at 4°C to remove bacterial debris.

2.4 Protein purification

2.4.1 HuPrP, MoPrP variants and other mammalian PrPs purification

The dissolved IBs in 8 M GndHCl were diluted to 6 M GndHCl using 50 mM Tris, 1 M NaCl, pH 8.0 then loaded onto a 5 mL HisTrap crude column (GE Healthcare) in binding buffer (2 M GndHCl, 500 mM NaCl, 20 mM Tris, 20 mM imidazole, pH 8.0). After that, the column was washed with 3 column volume (CV) of binding buffer and eluted with a gradient from 0-100 % of elution buffer (5 M GndHCl, 500 mM NaCl, 20 mM Tris, 500 mM imidazole, pH 8.0) at 5 mL/min in 20 min. Finally, the PrP-contained fractions were loaded onto gel filtration column (Superdex 200 26/60, GE) and eluted with 6 M GndHCl, 25 mM Tris-HCl, 5 mM EDTA, pH 8 at a flow rate of 2 mL/min. Purified protein was analyzed by SDS-PAGE. Protein concentration was determined by UV at 280 nm and stored at −80 °C before use.

2.4.2 FNIII1,2, FNIII1 and FNIII2 purification for NMR structural studies

Double labeled ^{13}C, ^{15}N FNIII1,2, FNIII1 and FNIII2 were purified according to the following protocol. The 8M GndHCl inclusion bodies solutions were diluted to 6M GndHCl using buffer 80 mM Tris, 2 M NaCl, pH 8. The solution was loaded 1 mL/min onto a 5 mL HisTrap column (GE Healthcare) equilibrated in binding buffer (2 M GndHCl, 500 mM NaCl, 20 mM Tris, 20 mM imidazole, pH 8) and eluted 5 mL/min using a gradient of elution buffer (2 M GndHCl, 500 mM NaCl, 20 mM Tris, 500 mM imidazole, pH 8). Purified proteins were analyzed by SDS-polyacrylamide gel electrophoresis under reducing condition.

2.5 Protein refolding

Lyophilized prion proteins were solubilized in sterile ddH_2O to a final concentration of 5 mg/mL. To 1 mL of 5 mg/mL of protein we added 4 mL of 8 M GndHCl, and then we leaved the samples at RT for 30 min or stored at -80°C before use. For refolding, the GndHCl solutions were rapidly diluted to a protein concentration of 0.1 mg/mL using buffer 25 mM Tris, 5 mM EDTA, pH 8. The samples were then dialyzed against refolding buffer (20 mM NaOAc, 0.005% NaN_3, pH 5.5) using a Spectra/Por membrane (cutoff of 3 kDa), until a final GndHCl concentration of about 10 μM.

2.5.1 Protein quantification

The protein concentration was determined, according to the Lambert-Beer law, by measuring the absorption at 280 nm (A_{280}).

2.6 Surface plasmon resonance experiments

Binding kinetics were determined on biacore 2000 (GE Healthcare). Ten µg of NCAM was diluted in 10 mM NaOAC, pH 5.2 and immobilized on CM5 chip activated with N-hydroxysuccinimide (NHS), N-ethyl-N-(3-dimethylaminopropyl) carbodiimide (EDC), using a flow rate of 5 µL/min. A steady signal of about 400 response units (RU) was obtained after immobilization and blocking with ethanol amine. All kinetic SPR analysis were run at 30 µL/min flow rate in PBS, 0.05% Tween20 and 3 mM ethylenediaminetetraacetic acid (EDTA) at 25 °C. After each cycle, the surface was regeneration with 60 s pulse of 100 mM glycine, pH 1.5. Association rates (K_{on}) and dissociation rates (K_{off}) were obtained using a 1:1 Langmiur binding model (Biacore evaluation software version 4.1). The equilibrium dissociation constant (K_d) was calculated from the ratio K_{off}/K_{on}.

2.7 ELISA experiments

BCL was immobilized at 0.5 µM and titrated with full-length HuPrP (0-5 µM). Antigen was detected using anti-PrP^C SAF34 antibody which recognizes an epitope corresponding to the octapeptide repeats region (residues 60-91) [206].

2.8 NMR spectroscopy experiments

Note: all the NMR experiments here presented were performed in collaboration with the group of Prof. Janez Plavec at the Slovenian NMR Centre, National Institute of Chemistry, Ljubljana, Slovenia.

2.8.1 Sample preparation

Refolded proteins were concentrated to 0.8-1 mM using Amicon centrifugal cells (Millipore). The same device was used for buffer exchange.

2.8.2 NMR spectroscopy

All NMR experiments used for structure determination were performed on ^{13}C, ^{15}N isotopically labelled FNIII2 domain on the Varian VNMRS 800 MHz NMR spectrometer equipped with triple $^{1}H/^{13}C/^{15}N$ resonance cryogenic probe head with inverse detection at 298 K. NMR sample contained 0.9 mM FNIII2 domain in 50 mM TBS buffer pH 7.45 and 150 mM NaCl. NMR experiments for HN and HC detection were performed in 90%/10% H_2O/D_2O and 100% deuterated buffer, respectively. Sequence-specific assignment of the backbone resonances for FNIII2 domain was obtained using standard double resonance ^{15}N-HSQC and triple resonance NMR experiments HNCO, HN(CO)CA, HNCA, HN(CO)CACB and HNCACB. ^{1}H and ^{13}C resonances of aliphatic and aromatic side chains were assigned using 13C-HSQC and

HAHB(CO)NH, CC(CO)NH, (H)CCH-TOCSY and ^{13}C-edited HSQC-NOESY experiments. NOEs contacts were determined in 3D ^{15}N- and ^{13}C-edited HSQC-NOESY experiments in order to perform structure calculation.

2.8.3 Structure calculations

The structure modelling of FNIII2 domain was performed using program CYANA 3.0 [207]. Structure refinement using explicit solvent model was performed by YASARA program [208]. An ensemble of 20 lowest energies structures of FNIII2 domain was validated by web server software ICing [209].

2.8.4 Titrations with HuPrP peptides

Titration of ^{13}C, ^{15}N isotopically labelled FNIII2 domain with unlabelled HuPrP(23-144) was performed in 25 mM HEPES buffer, pH 7.0. Titrations of labelled FNIII2 domain were also done with unlabelled HuPrP(23-50), HuPrP(23-89), HuPrP(60-68), HuPrP(93-114), HuPrP(93-114, P102L) peptides at pH 6.0 (20 mM NaOAc buffer, 0.35 mM labelled FNIII2 domain per titration experiments). Titrations were followed by analysis of Δδ(H,N) of FNIII2 domain in ^{15}N-HSQC experiments. All recorded spectra were processed by NMRPipe [210] software and analysed with CARA [211] and Sparky [212] software.

Amide chemical shift changes were calculated for each non-overlapped cross-peak in ^{15}N-HSQC spectrum of FNIII2 domain according to Eq. (1) and (2):

$$\Delta\delta(H,N) = \sqrt{(\Delta\delta_H)^2 + (0.154 \times \Delta\delta_N)^2} \quad \ldots \text{Eq. 1}$$

$$\Delta\delta_{H,N} = \delta_{H,N\ bound} - \delta_{H,N\ free} \quad \ldots \text{Eq. 2}$$

where $\Delta\delta_H$ and $\Delta\delta_N$ are defined as the difference in the ^{1}H and ^{15}N amide chemical shifts between the protein-peptide complex and the free state of FNIII2 domain [213].

2.8.5 Modelling the complex between FNIII2 domain and HuPrP(93-114, P102L)

Modelling of complex between FNIII2 domain and HuPrP(93-114, P102L) was made with HADDOCK software [214, 215].

2.8.6 Accession number

The chemical shift data were deposited in Biological Magnetic Resonance Data Bank (BMRDB). The atomic coordinates and structure factors (code 5LKN) have been deposited in the Protein Data Bank (PDB).

2.9 X-ray Absorption measurements

Note: All X-ray absorption measurements were performed in collaboration with the group of Prof. Paola D'Angelo (Department of Chemistry, University of Rome "La Sapienza", Rome, Italy).

2.9.1 Sample preparation

Refolded proteins were concentrated to 1.5-2 mM using Amicon centrifugal cells (Millipore). Samples with 1:1 Cu(II):WT and mutants HuPrP(90-231) ratio were prepared in 25 mM NaOAc pH 5.5 and 25 mM MOPS buffer pH 7.0. The Cu(I):WT and mutants HuPrP(90-231) complexes were generated reducing Cu(II) with 40 mM ascorbate.

2.9.2 XAS spectra data collection

X-ray absorption spectra were recorded at the European Synchrotron Radiation Facility (ESRF) on beam line BM30B, under ring conditions of 6.0 GeV and 180 mA. The spectra were collected at the Cu K-edge in fluorescence mode using a solid state 30-element Ge detector, with sample orientation at 45° to incident beam. The X-ray photon beam was vertically focused by a Ni−Pt mirror, and dynamically sagittally focused in the horizontal size. The monochromator was equipped with a Si(111) double crystal, in which the second crystal was elastically bent to a cylindrical cross section. The energy resolution at the Cu K-edge is 0.5 eV. The spectra were calibrated by assigning the first inflection point of the Cu foil spectrum to 8981 eV. All the spectra were collected at 10 K. For Cu(II) samples photo reduction is usually observed and thus the beam was moved to different spots of the sample at each scan. During collection, data were continuously monitored in order to insure sample homogeneity across the multiple spots collected from different sample-holder's cells. For each sample, 12 spectra were recorded with a 7 s/point collection statistic and averaged. The collection time was 25 min for each spectrum.

2.9.3 EXAFS Data Analysis

The analysis of the EXAFS data was carried out using the GNXAS code, which is based on a theoretical calculation of the X-ray absorption fine structure signal and a subsequent refinement of the structural parameters. In the GNXAS approach the interpretation of the experimental data is based on the decomposition of the EXAFS χ(k) signal into a summation over *n*-body distribution functions $\gamma^{(n)}$, calculated by means of the MS theory. Each signal has been calculated in the muffin-tin approximation using the Hedin-Lundqvist energy dependent exchange and correlation potential model, which includes inelastic loss effects. The analysis of the EXAFS spectra was carried out starting from the coordination models reported in the literature for the WT HuPrP and HuPrP Q212P proteins [164, 165, 216]. In particular the Cu(II) ion was found to have two different coordinations: in the former case the inner shell is formed by H96, H111, and two additional low Z ligands (oxygen or nitrogen donors), while M109 and Q98 are found in the Cu(II) axial positions. In the latter case the Cu(II) ion is coordinated by a single histidine ligand, namely H111, and three N/O scatterers, while one more distant sulphur

atom and a water molecule are found at longer distance. Based on these two models and considering the amino acidic residues present in the different mammalian PrP^C, theoretical EXAFS spectra were calculated to include contributions from first shell two-body signals, and three-atom configurations. Previous investigations on model compounds have shown that a quantitative EXAFS analysis of systems containing histidine rings or having amino acidic residues that are chelated to the Cu(II) ion, requires a proper treatment of MS contributions [164, 165, 217]. The analysis of the OvPrP ARR and OpPrP resistant species has been carried out considering the coordination with a nitrogen atom of H111, with two oxygen atoms of S95 that chelates the Cu(II) ion forming a ring in the equatorial pane (in this case two carbon atoms of the serine give rise to a single scattering contribution at about 2.86 Å), with an oxygen atom of Q98 and a sulphur atom of M109. The EXAFS spectra of the more susceptible OvPrP VRQ and BvPrP species have been analysed using the same model as HuPrP Q212P where the Cu(II) ion is coordinated by H111, Q98, M109 and a water molecule. The model χ(k) signal is then refined against the experimental data by using a least-squares minimization procedure in which structural and nonstructural parameters are allowed to float. The structural parameters are the bond distance (R) and bond variance (σ^2_R) for a two-body signal, the two shorter bond distances, the intervening angle (θ and φ), and the six covariance matrix elements for a three-body signal. In all cases two additional nonstructural parameters were minimized, namely E_0 (core ionization threshold) and S_0^2 (many body amplitude reduction factor). To establish error limits on the structural parameters, a number of selected parameters from the fit results were statistically analyzed using two-dimensional contour plots. This analysis examines correlations among fitting parameters and evaluates statistical errors in the determination of the copper coordination structure, as previously described [164]. Briefly, parameters with highest correlation dominate in the error estimate. The results of the EXAFS fits for all the systems are given in Table S1 and the best-fit curves are shown in Figure S1. The EXAFS spectra were analyzed in the k range between 2.4-12.6 $Å^{-1}$. In all cases S_0^2 was found equal to 0.9, while E_0 was found 3 eV above the first inflection point of the spectra.

2.10 Molecular Dynamics simulation on HuPrP WT

Note: The simulation-based structural predictions were performed by Giordano Mancini (Scuola Normale Superiore, Pisa, Italy). For this reason, we have moved the related Materials and Methods in the **Appendix II, Section II**.

2.11 Cell culture and transfection

2.11.1 Neuroblastoma cell cultures

N2a and ScN2a cells were cultured in Opti-MEM (GIBCO) media supplemented with 10% fetal bovine serum (FBS) and 1% penicillin-streptomycin, and incubated at 37 °C, 5% CO_2.

Transient transfections were performed using X-treme gene DNA transfection kit (Roche Biochemicals) according to the manufacturer guidelines. Seventy-two hours post-transfection, the cells were collected for further analysis.

2.11.2 Biochemical assays on PrP^{Sc} and PrP^{C}

Cell lysates were harvested in cold lysis buffer (10 mM TrisHCl pH 8.0, 150 mM NaCl, 0.5% Nonidet P-40 substitute, 0.5% sodium deoxycholate), quantified by BCA protein assay kit (Pierce) and stored at −20 °C until use. For protease-K (PK) digestion assay, quantified protein lysates were treated with PK (Roche) at 37 °C. ScN2a cell lysates were digested with 20 μg/mL of PK for 1 hour, while cell lysates from N2a cells transfected with either WT or H96Y 3F4-MoPrP constructs were digested with 2 and 5 μg/mL of PK for 30 minutes. PK digestions were stopped by adding 2 mM phenylmethyl-sulphonyl fluoride. Subsequently, the samples were ultracentrifuged at 100,000 g for 1 h at 4 °C (Optima TL, Beckman Coulter, Inc.). The pellets were resuspended in sample buffer. The glycan modifications on PrP^{C} were assessed using Endo-H and PNGase-F enzymes (New England Biolabs) according to the manufacturer instructions. Samples were loaded onto a 10% SDS-PAGE gel and immunoblotted on Immobilion PVDF (Millipore) membranes. Membranes were blocked with 5% (w/v) non-fat milk protein in TBS-T (0.05% Tween), incubated with 1:1000 anti-PrP antibody 3F4 (Covance), and developed by enhanced chemiluminescence (GE Healthcare). Band intensity was acquired using the UVI Soft software (UVITEC, Cambridge). Total PrP^{C} expression levels in N2a and ScN2a cell lysates were normalized on β-actin value using 1:10,000 anti-β-actin Peroxidase (Sigma-Aldrich). The PrP^{Sc} PK-resistance levels in all the mutants were derived using as reference the PK-resistant band intensity of the ScN2a cells transfected with WT 3F4-MoPrP. To evaluate the role of copper in prion conversion, ScN2a cells were transiently transfected with pcDNA3.1::3F4-MoPrP(1–254) WT and pcDNA3.1::3F4-MoPrP(1–254) H96Y plasmids, treated for 48 hours with increasing concentration (10, 20, 30 and 40 μM) of cuprizone (CPZ, Sigma Aldrich) and immediately collected for lyses, PK digestion and immunoblot as described above.

2.11.3 Fluorescence imaging

Cells were grown on poly-L-lysine-coated coverslips for 24 hours before fixation in 4% paraformaldehyde and washed with PBS prior to blocking in 1% FBS, 0.3% Triton X-100. Cells were incubated at 4 °C for 12 hours in blocking buffer with anti-PrP primary antibodies, *i.e.* 3F4 and D18 (InPro Biotechnology) monoclonal antibodies. The following day, cells were incubated for 1 hour with secondary antibodies conjugated with AlexaFluor. For PrP^{C} cell surface detection, cells were incubated at 4 °C for 15 min and probed with 3F4 antibody. Cells were permeabilized with 0.2% Triton-X and stained with AlexaFlour-488 secondary antibody. To detect Thioflavin-S (ThS)-positive aggregates, transfected and non-transfected cells were fixed with 4% PFA/4% sucrose/1% Triton X-100 in PBS. For organelle markers, we used anti-Calnexin (ER marker), anti-EEA1 (early endosome marker), anti-Tfn (recycling endosome marker), anti-M6PR (late endosomes marker) and anti-LAMP2 (lysosomes marker) purchased

from Abcam. Nuclei were stained with DAPI dye (VECTOR Laboratories). Images were acquired with a DMIR2 confocal microscope equipped with Leica Confocal Software (Leica).

2.11.4 Monitoring the kinetics of in vitro fibril formation

To monitor the formation of ThT-positive fibrils, we used 100 µg/mL of WT full-length MoPrP stored in acetate buffer (25 mM NaOAc, 6 M GdnHCl, pH 5.5) or Tris buffer (25 mM Tris-HCl, 6 M GdnHCl, pH 7.0). To induce protein polymerization in the amyloid seeding assay (ASA) we added a preformed PrP^{Sc} seed to the reaction purified from ScN2a transiently expressing either 3F4-tagged WT MoPrP or 3F4-tagged H96Y MoPrP according to our previous protocols. Data were analyzed and figures were produced using Origin 8.6 software.

2.11.5 Prion formation in N2a cells

N2a cells were transiently transfected with either 3F4-tagged WT or H96Y MoPrP and regularly passaged every 7 days up to passage (P) 8. Subsequently, the protein extracts were analyzed by PK digestion to monitor the presence of PK-resistant PrP^{Sc} levels through passages (see above). Prion formation was assessed by cell seeding experiments. Phosphotungstic acid (PTA)-extracted PrP^{res} seeds -we denoted as PrP^{res} the material generated by N2a cells transfected with 3F4-tagged H96Y MoPrP- were subjected to N2a cells and regularly passaged every 7 days up to P8. The detection of newly generated PrP^{res} was assessed by PK digestion as previously described, and the PrP^{res} seeds isolation using PTA was performed according to our previous protocols.

CHAPTER III

RESULTS

3.1 Identification of the structural determinant responsible for the interaction between PrP^C and NCAM

Among the variety of PrP^C protein interactors, the neuronal cell adhesion molecule (NCAM) has been proved *in vivo*, but the structural basis of this functional interaction are still a matter of debate. Here we focused on the structural determinants responsible for human PrP^C (HuPrP) and NCAM interaction using Stimulated Emission Depletion (STED) nanoscopy, surface plasmon resonance (SPR) and NMR spectroscopy approaches.

PrP^C co-localizes with NCAM in mouse hyppocampal neurons and this interaction is mainly mediated by the intrinsically disordered PrP^C N-terminal domain, which binds with high affinity the NCAM fibronectin type-3 domain. NMR structural investigation revealed surface interacting epitopes governing the interaction between HuPrP N-terminus and the second module of NCAM fibronectin type-3 domain. Our data provided a molecular-level picture of the interaction between HuPrP and NCAM fibronectin domain, and revealed a new role of PrP^C N-terminus a dynamic and functional element responsible for protein-protein interaction.

3.1.1 NCAM co-localizes with PrP^C

Functional interactions of PrP^C with its binding partner(s) have been suggested previously [218]: *cis* and *trans* interactions between NCAM and PrP^C promote neurite outgrowth; the disruption of these interactions indicate that PrP^C is involved in nervous system development cooperating with NCAM as a signaling receptor.

We used STimulated Emission Depletion (STED) nanoscopy to confirm the association between PrP^C and NCAM in mouse hippocampal culture. We determined simultaneously the cellular distribution of PrP^C, NCAM and Actin (**Fig. 3.1 A**). PrP^C and NCAM share very similar distributions along the neurite and in hippocampal growth cones (GC). The staining for PrP^C and NCAM was preferentially localized in the central domain and transition zone of the GC membrane, when compared to the actin, rarely detecting these staining in motile structure like filopodia (**Fig. 3.1 B**).

By using STED nanoscopy we could detect very low colocalization between PrP^C and NCAM, while treatment with 1 μM nerve growth factor (NGF) results in an increasing of colocalization (**Fig. 3.1 B**). The observed higher association between PrP^C and NCAM in treated cultures

suggested that these proteins might functionally cooperate to transduce signals into the cell interior, which in turn trigger the neurite growth.

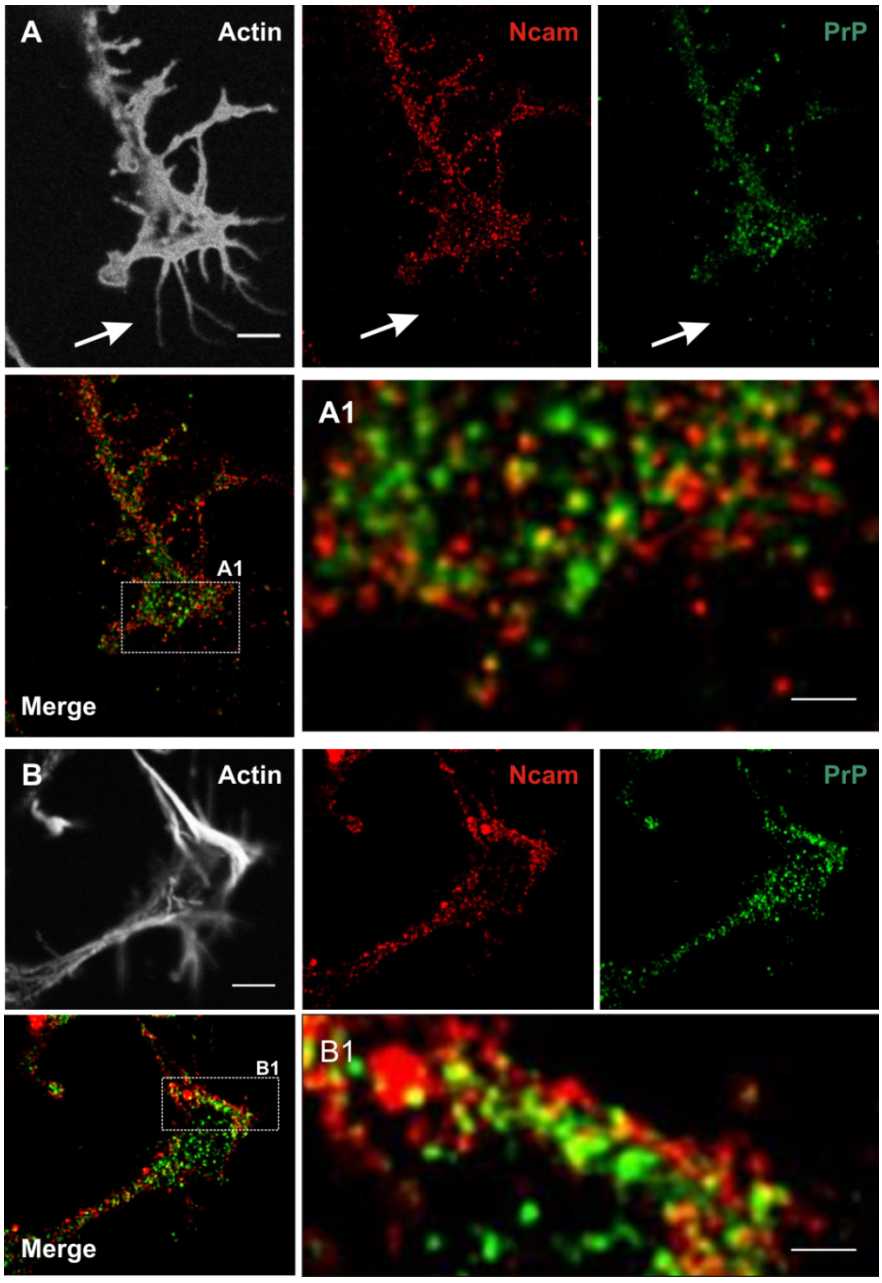

Figure 3.1. PrP-NCAM interaction in vitro. STED images of GC stained for PrP, NCAM, Actin and merge of the PrP and NCAM in control condition. Scale bar 500 nm. (A1-A2) High-resolution images of areas indicated in **(A)**. Scale bar 250 nm. **(B)** As in (A) but neurons were incubated with 1 μM NGF (2 h).

3.1.2 FNIII1,2 domain binds to the HuPrP N-terminal domain with high affinity.

SPR experiments were used to analyse the binding of FNIII1,2 domain to different HuPrP and MoPrP constructs, including full-length HuPrP and MoPrP (*i.e.* from residues 23 to 231 and 23-230, respectively), the HuPrP N-terminal domain (residues 23-144) and the truncated C-terminal HuPrP and MoPrP (residues 90-231 and 89-230, respectively). We observed strong interaction between FNIII1,2 domain and the HuPrP N-terminal domain with K_d of 5.4 nM. Also the full-length HuPrP binds to FNIII1,2 domain with high affinity (K_d of 337 nM) while for the truncated HuPrP we were not able to report any interaction. The full-length MoPrP displayed a week affinity for FNIII1,2 domain (K_d 3.8 μM), while the truncated MoPrP behaved almost identically to the truncated HuPrP, displaying no interaction with FNIII1,2 domain (**Figure 3.2 and Table 3.1**).

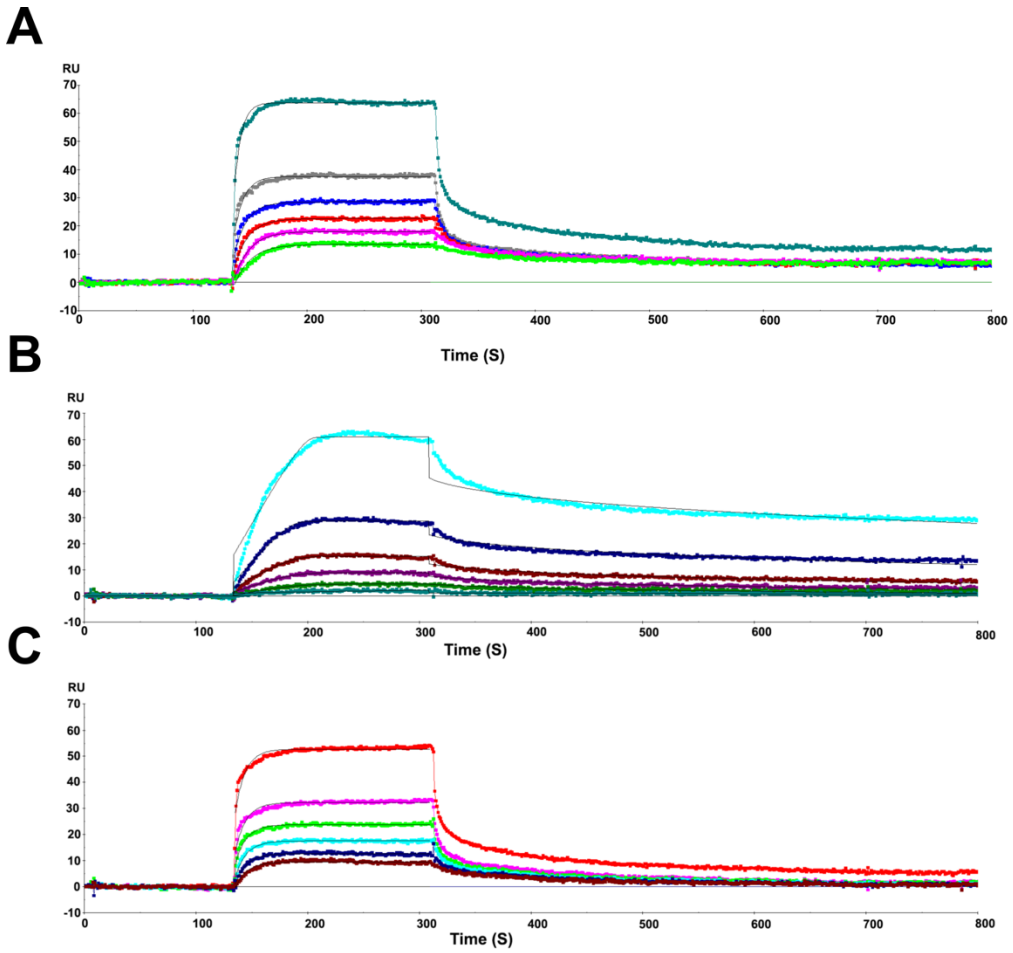

Figure 3.2. SPR analysis of the FNIII-HuPrP or MoPrP interactions. Shown are raw sensorgrams obtained on a Biacore 2000 instrument. Selected curves are labelled with the respective analyte concentration. Binding of full-length HuPrP, HuPrP N-terminus and full-length MoPrP to immobilized FNIII (A, B and C, respectively).

Table 3.1. Dissociation constants for the interaction between FNIII (immobilized) and different HuPrP and MoPrP constructs.

Protein	K_d (nM)	K_{on} (1/Ms)	K_{off} (1/s)	Chi^2
HuPrP(23-231)	337	2.00E+05	0.0674	0.629
HuPrP(90-231)	NO	NO	NO	NO
HuPrP(23-144)	5.4	1.42E+06	7.66E-03	0.612
MoPrP(23-230)	3800	2.58E+04	0.0983	0.684
MoPrP(89-230)	NO	NO	NO	NO

Additionally, we confirmed that a short NCAM peptide, named BCL, corresponding sequence of residues 620-635 in FNIII1,2 domain is able to interact with HuPrP using ELISA (**Figure 3.3**). Peptide BCL also binds to MoPrP [155] and it is considered a NCAM mimetic peptide employed as NCAM surrogate in pharmacological experiments [219]. These data add more insights about the HuPrP regions involved in the interaction with FNIII1,2 domain, showing that this binding is largely mediated by the largely unstructured N-terminal HuPrP domain.

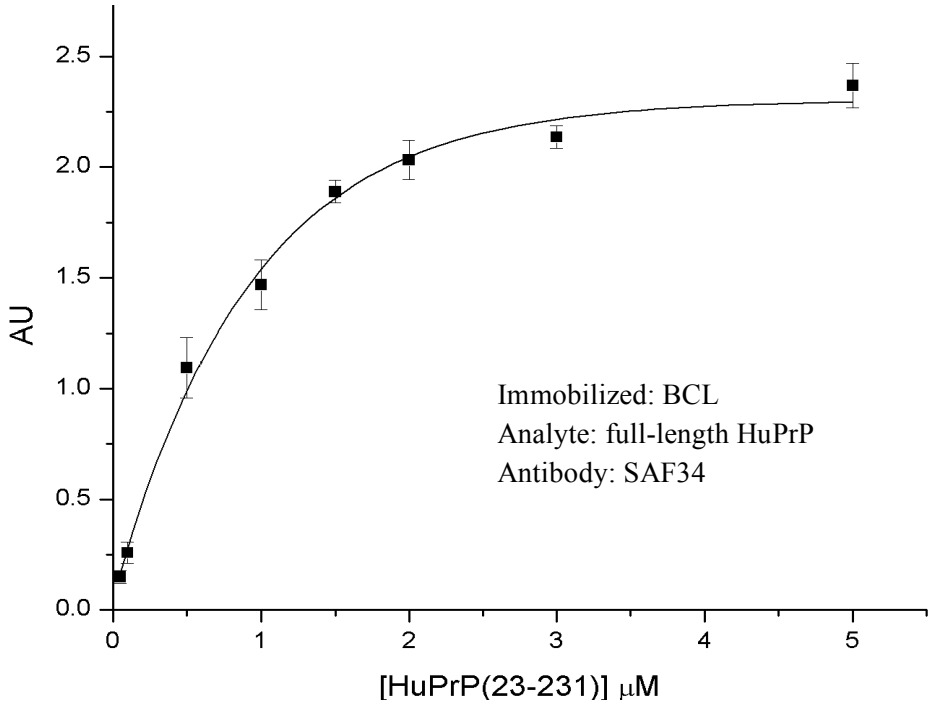

Figure 3.3. ELISA showing the interaction between BCL and full-length HuPrP.

3.1.3 NMR structure of the NCAM fibronectin domain 2, FNIII2

3.1.3.1 Sequence-specific resonance assignment of the FNIII2

Binding properties of HuPrP and NCAM in solution were evaluated by performing NMR spectroscopy. Unambiguous assignment of HuPrP(23-144) residues was not possible because of high signal overlap in the ^{15}N-HSQC spectrum, which was due to high percent of glycine residues, octarepeats and intrinsically disordered properties of unstructured N-terminus **(Fig. 3.4 A)**. Thus, studies with ^{15}N, ^{13}C isotopically labelled FNIII1,2, FNIII1 and FNIII2 domains were performed in order to find a suitable candidate to evaluate HuPrP-NCAM binding properties.

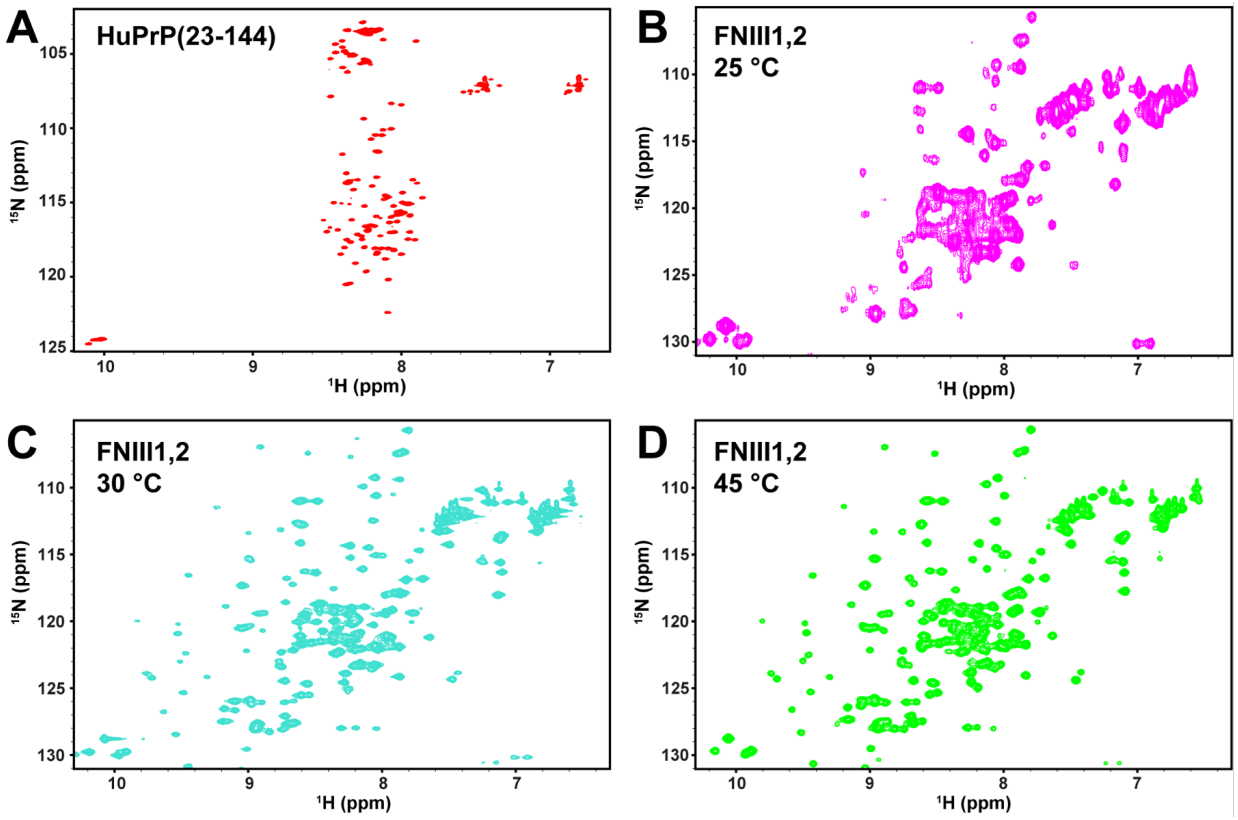

Figure 3.4. (A) ^{15}N HSQC spectra of HuPrP(23-144) and **(B-D)** FNIII1,2 domain at three different temperatures.

^{15}N HSQC spectra of FNIII1,2 domain were detected at three different temperatures. The ^{15}N-HSQC spectrum of FNIII1,2 domain was crowded with overlapped signals at 25 °C (**Figure 3.4 B**). To improve relaxation features and cross peaks intensities in ^{15}N-HSQC spectrum of FNIII1,2 domain the temperature of the sample was increased to 30 °C and 45 °C (**Figure 3.4 C and D**). While this approach resulted in a clear improvement of spectra resolution, on the other hand it caused the instability of the sample, leading to a complete protein precipitation.

To characterized binding properties between HuPrP and NCAM, smaller module of FNIII1,2, FNIII1 and FNIII2 domains, were examined. The FNIII1 domain was also unappropriated for study because of sample instability. Thus, we employed the FNIII2 domain as a model system.

^{15}N HSQC spectrum of ^{13}C, ^{15}N double labelled FNIII2 domain demonstrated good dispersion of cross-peaks indicating that the protein adopts a globular fold thus a potential for detailed structure characterisation (**Figure 3.5 A**).

Sequence-specific assignment of the backbone resonances for FNIII2 domain was obtained using standard double resonance ^{15}N-HSQC and triple resonance NMR experiments HNCO, HN(CO)CA, HNCA, HN(CO)CACB and HNCACB (See **Figure 3.6** for the detailed spectra description). For side-chain assignments the protein was buffer exchanged in deuterated water to perform a ^{13}C heteronuclear experiment **(Figure 3.7)**. ^{1}H and ^{13}C resonances of aliphatic and aromatic side chains were assigned using ^{13}C-HSQC and HAHB(CO)NH, CC(CO)NH, (H)CCH-TOCSY and ^{13}C-edited HSQC-NOESY experiments (**Figure 3.8)**.

Final level of completeness of ^{1}H, ^{13}C and ^{15}N resonance assignment was high (92.9%). Forty-three chemical shifts were unassigned, most of them belonged to the C-terminal His-tag.

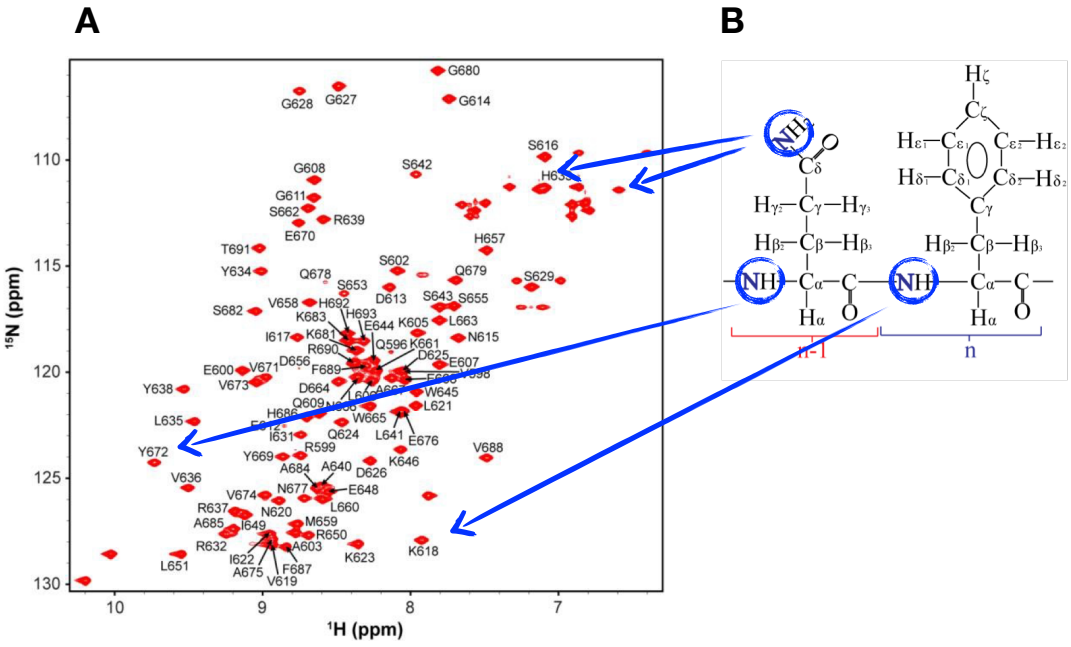

Figure 3.5. Assigned ^{1}H-^{15}N HSQC spectrum of FNIII2 with one letter amino acid code. (**A**) A two-dimensional HSQC spectrum of the FNIII2 is represented. The nitrogen chemical shifts are shown on the left side of the spectrum. (**B**) In this spectrum are visible cross-peaks for all N-H correlations. Mainly these are amide groups of protein backbone, with exception of prolines. The side chain NH_2- groups of Asn and Gln are visible, usually in the right upper corner of the spectrum and the Trp side chain groups are also detected.

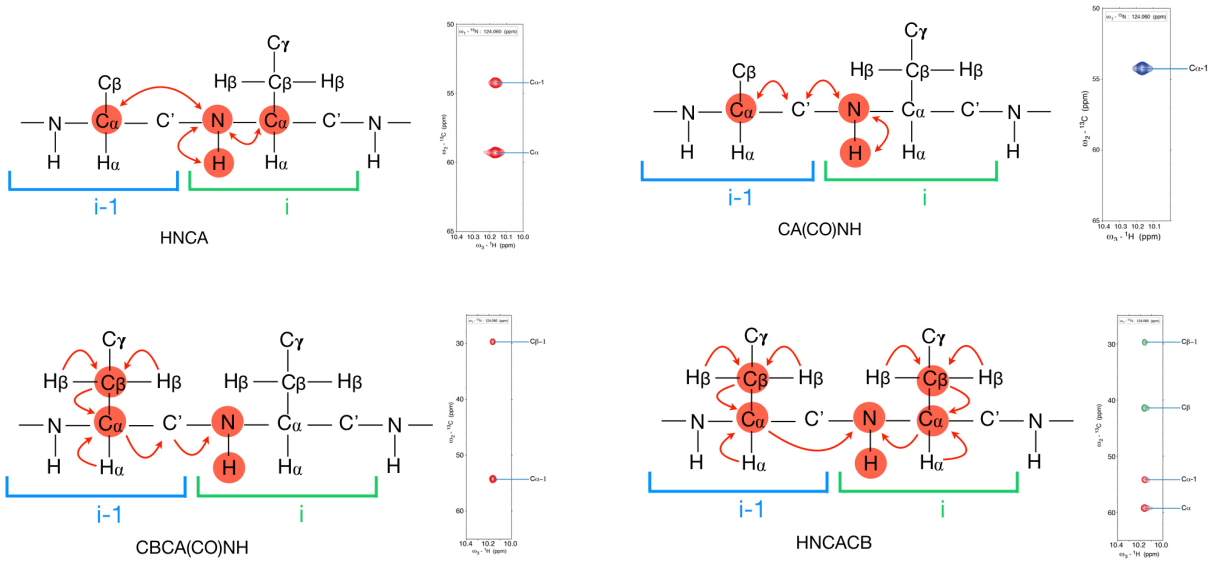

Figure 3.6. NMR sequence specific backbone assignment strategy. In the **HNCA** experiment the magnetization is transferred from ^{1}H to ^{15}N and then via the N-Cα J-coupling to the $^{13}Cα$ and then back again to ^{15}N and ^{1}H hydrogen for detection. The chemical shift is evolved for $^{1}H^{N}$ as well as the $^{15}N^{H}$ and $^{13}Cα$, resulting in a 3-dimensional spectrum. Since the amide nitrogen is coupled both to the Cα of its own residue and that of the preceding residue, both these transfers occur and peaks for both Cα are visible in the spectrum. However, the coupling to the directly bonded Cα is stronger, thus these peaks will appear with greater intensity in the spectra. In the **CA(CO)NH** spectrum the magnetization is passed from ^{1}H to ^{15}N and then to C'. From here it is transferred to $^{13}Cα$ and the chemical shift is evolved. The magnetization is then transferred back via C' to ^{15}N and ^{1}H for detection. The chemical shift is only evolved for the ^{1}HN, the $^{15}N^{H}$ and the $^{13}Cα$, but not for the C'. This results in a spectrum which is like the HNCA, but which is selective for the Cα of the preceding residue. In the **CBCA(CO)NH** spectrum magnetization is transferred from $^{1}Hα$ and $^{1}Hβ$ to $^{13}Cα$ and $^{13}Cβ$, respectively, and then from $^{13}Cβ$ to $^{13}Cα$. From here it is transferred first to C', then to ^{15}NH and finally to $^{1}H^{N}$ for detection. The chemical shift is evolved simultaneously on $^{13}Cα$ and $^{13}Cβ$, so these appear in one dimension. The chemical shifts evolved in the other two dimensions are $^{15}N^{H}$ and $^{1}H^{N}$. The chemical shift is not evolved on C'. Finally, in the **HNCACB** magnetization is transferred from $^{1}Hα$ and $^{1}Hβ$ to $^{13}Cα$ and $^{13}Cβ$, respectively, and then from $^{13}Cβ$ to $^{13}Cα$. From here it is transferred first to $^{15}N^{H}$ and then to $^{1}H^{N}$ for detection. Transfer form $Cα_{i-1}$ can occur both to $^{15}N_{i-1}$ and $^{15}N_{i}$, or viewed the other way, magnetization is transferred to ^{15}Ni from both $^{13}Cα_{i}$ and $^{13}Cα_{i-1}$. Thus, for each NH group there are two Cα and Cβ peaks visible. The chemical shift is evolved simultaneously on $^{13}Cα$ and $^{13}Cβ$, so these appear in one dimension. The chemical shifts evolved in the other two dimensions are $^{15}N^{H}$ and $^{1}H^{N}$.

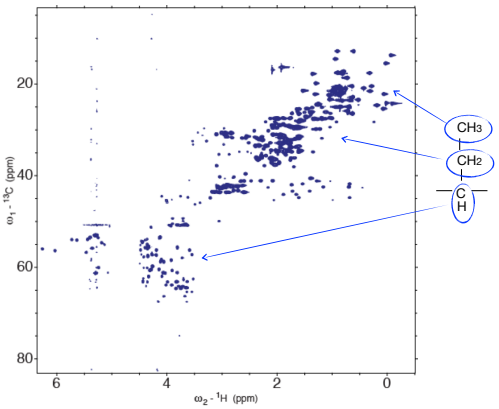

Figure 3.7. ^{1}H-^{13}C HSQC spectrum of FNIII2. This spectrum is the carbon equivalent of the ^{1}H-^{15}N-HSQC and it is a useful reference for side-chain assignments. All ^{1}H-^{13}C correlations are shown. The magnetization is transferred from ^{1}H to ^{13}C and then back again for detection and all ^{1}H-^{13}C moieties, regardless of chemical type, are showed.

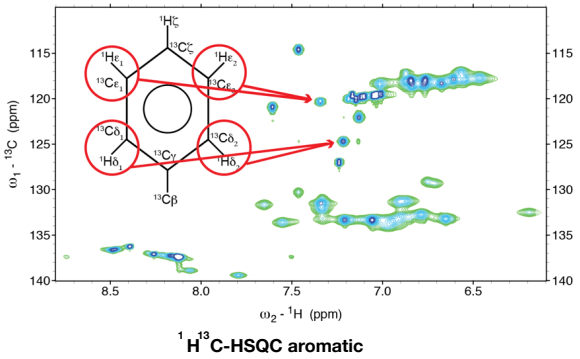

Figure 3.8. Side chain assignment strategy. ^{13}C-HSQC aliphatic spectrum has been explained in the previous picture. Similarly, in the ^{13}C-HSQC aromatic spectrum the magnetization is transferred from ^{1}H to ^{13}C and then back again for detection, and all ^{1}H-^{13}C moieties present in aromatic rings are showed.

The assignment starts with a set of C(CO)NH spectra. In the CC(CO)NH spectrum the magnetization is transferred from the side-chain hydrogen nuclei to their attached ^{13}C nuclei. Then isotropic ^{13}C mixing is used to transfer magnetization between the carbon nuclei. From here, magnetization is transferred to the carbonyl carbon, onto the amide nitrogen and finally the amide hydrogen for detection. The chemical shift is evolved simultaneously on all side-chain carbon nuclei, as well as on the amide nitrogen and hydrogen nuclei, resulting in a three-dimensional spectrum. Additional 3D experiments are obtained that are optimized for side chain spin connectivity. In the (H)CCH-TOCSY spectrum magnetization is transferred from the side-chain hydrogen nuclei to their attached ^{13}C nuclei. This is followed by isotropic ^{13}C mixing and finally transfers back to the side-chain hydrogen atoms for detection. The proton resonances in aromatic ring are assigned using 3D ^{15}N ^{13}C HSQC-NOESY spectra. In these spectra magnetization is exchanged between all hydrogens using the NOE. Then the magnetization is transferred to neighboring ^{13}C nuclei and back to ^{1}H for detection.

3.1.3.2 Three-dimensional structure of FNIII2

The structure modelling of FNIII2 domain was performed using program CYANA 3.0 [207]. **Figure 3.9** shows iterative cycles of structure determination by extracting upper-distances from NOESY data sets, based on the CANDID algorithm.

A high-resolution NMR structure of FNIII2 domain was determined on the basis of the high level of resonance assignments (92.9%) and in a total of 1658 NOE restraints. The root-mean-square deviation (r.m.s.d.) values relative to the mean coordinates are 0.28 Å for backbone and 0.78 Å for heavy atoms (residues 595-691). The complete structural statistics is summarized in **Table 3.2**.

The calculated three-dimensional model showed that FNIII2 domain consists of six antiparallel β-strands, marked A-F on **Figure 3.10**. They are arranged into two right-handed β-sheets which formed a β-sandwich. The first β-sheet is composed of strands A and D (residues Ser616-Asn620 and His657-Lys661, respectively) and the second β-sheet of strands B, C, E and F (residues Ile631-Ala640, Ile649-Pro652, Tyr669-Asn677 and Ala682-Phe687, respectively).

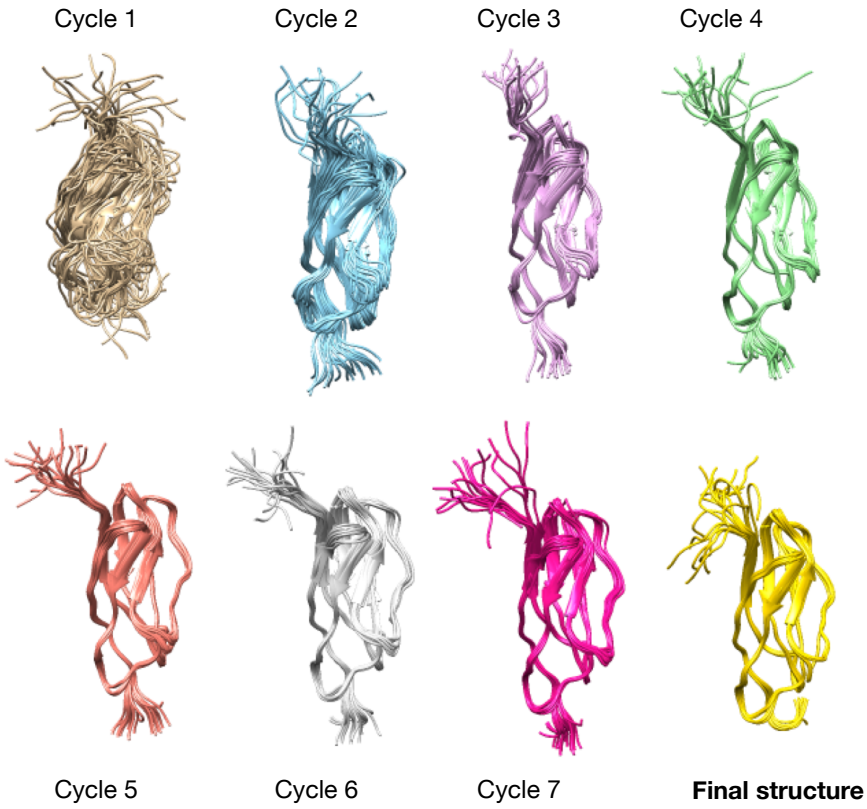

Figure 3.9. Structures of FNIII2 obtained with the program CYANA.

Table 3.2. NMR restraints and structural statistics for the ensemble of 20 lowest energy structures of FNIII2 domain.

NOE upper distance limits[a]	
Total	1658
Intra-residue (|i-j| = 0)	337
Sequential (|i-j| = 1)	441
Medium-range (1 < |i-j| < 5)	108
Long-range (|i-j| >= 5)	772
Torsion angle restraints	
Backbone (φ/ψ)	136
RMSD to the mean coordinates (Å)	
Ordered backbone atoms (1-97)	0.28 ± 0.09
Ordered heavy atoms (595-691)	0.78 ± 0.08
Ramachandran plot (595-691)[b]	
Residues in most favored regions (%)	85.2
Residues in additional allowed regions (%)	14.8
Structure Z-scores[b]	
1st generation packing quality	-0.419 ± 0.568
2nd generation packing quality	7.386 ± 2.149
Ramachandran plot appearance	-3.376 ± 0.339
Chi-1/chi-2 rotamer normality	-6.283 ± 0.259
Backbone conformation	-0.441 ± 0.137
RMS Z-scores[b]	
Bond lengths	1.201 ± 0.004
Bond angles	0.581 ± 0.008
Omega angle restraints	0.758 ± 0.030
Side chain planarity	0.437 ± 0.029
Improper dihedral distribution	0.779 ± 0.016
Inside/Outside distribution	1.029 ± 0.011

[a] None of the 20 structures exhibits distance violations over 0.2 Å and torsion angle violation over 5°.
[b] Ensemble of structures was analysed by PROCHECK-NMR and WhatIF programs incorporated in CING structure evaluation package [209].

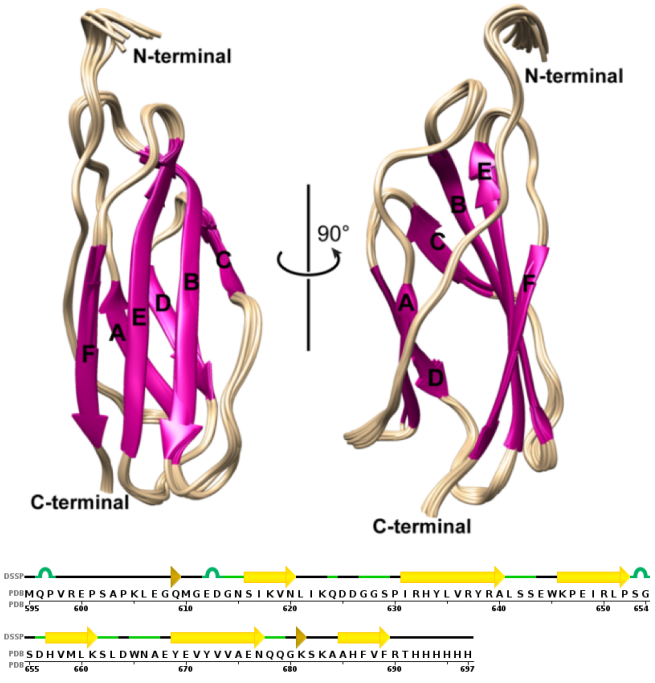

Figure 3.10. (A) Ensemble of 20 lowest energies structure of FNIII2 domain (residues 595-691). The β-strands are highlighted using letter codes. **(B)** Sequence of FNIII2 protein. The elements of secondary structure are shown.

3.1.4 NMR chemical shift perturbation analysis for characterizing the binding between HuPrP and NCAM

Multidimensional heteronuclear NMR experiments were used to evaluate binding properties between the FNIII2 domain and N-terminal HuPrP(23-144) and to characterize the formed complex. Upon addition of HuPrP(23-144) the FNIII2 domain sample became blurred due to aggregation, leading to multimeric complex at pH 7.0. Interestingly, during the titration experiment no amide chemical shift changes Δδ(H,N) were observed in ^{15}N-HSQC spectrum of FNIII2 domain (**Figure 3.11**). Detailed analysis of cross-peak line widths and absence of chemical shift changes gave the conclusion that cross-peaks correspond to unbound state of labelled FNIII2 domain.

Analysis of signal intensities during the titration indicated that the cross-binding complex is formed in a 1:1 ratio. Additionally, we tried to thermally disrupt multimeric complex at 45 °C to gain monomeric form of the complex. While the sample cleared up indicating that the multimeres fell apart to smaller fragments, the ^{15}N-HSQC spectrum did not improve after thermal treatment. Clearly, even smaller fragments of multimeric complex were still too big to be observed by NMR. Titration was replicated at pH 6.0 (**Figure 3.12 A**). Δδ(H,N) were observed in ^{15}N-HSQC spectra of FNIII2 domain at ratio 1 to 0.5 for residues Arg599, Glu600, Gly614, Arg639, Ser642, Asp656, Ser664, Tyr669, Tyr672, Gln678, Lys683, His686 and Val688. However, the cross-peaks in ^{15}N-HSQC spectra of FNIII2 domain disappeared at ratio 1:2 due to complex formation similarly as observed at higher pH value.

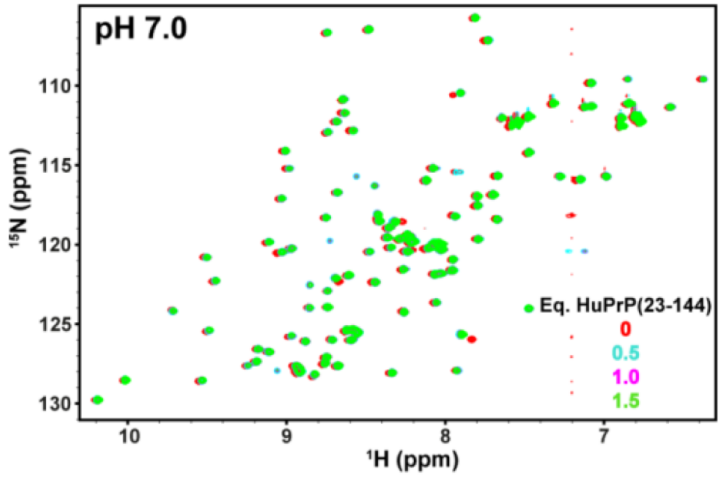

Figure 3.11. ^{15}N HSQC spectrum of FNIII2 domain overlaid with ^{15}N HSQC spectrum of FNIII2 domain titrated with HuPrP(23-144) peptide at pH 7.0.

In order to determine the binding site on HuPrP, the N-terminal part of it was divided into smaller fragments. Graduate titrations of FNIII2 domain with peptides HuPrP(23-89), HuPrP(23-50), HuPrP(60-68), HuPrP(93-114) and HuPrP(93-114, P102L) were performed to the final ratio between protein and peptide 1 to 2 **(Figure 3.12)**. Upon titrations with HuPrP(93-114), HuPrP(93-114, P102L) and HuPrP(23-89) Δδ(H,N) were observed in ^{15}N-HSQC spectra

of FNIII2 domain (**Figure 3.12 C, E and F**). In contrast, we did not identified any Δδ(H,N) of FNIII2 domain with peptide HuPrP(60-68) (**Figure 3.12 B**) and negligible one with peptide HuPrP(23-50) (**Figure 3.12 D**). For all titration studied were calculated Δδ(H,N) of FNIII2 domain using equation 1.

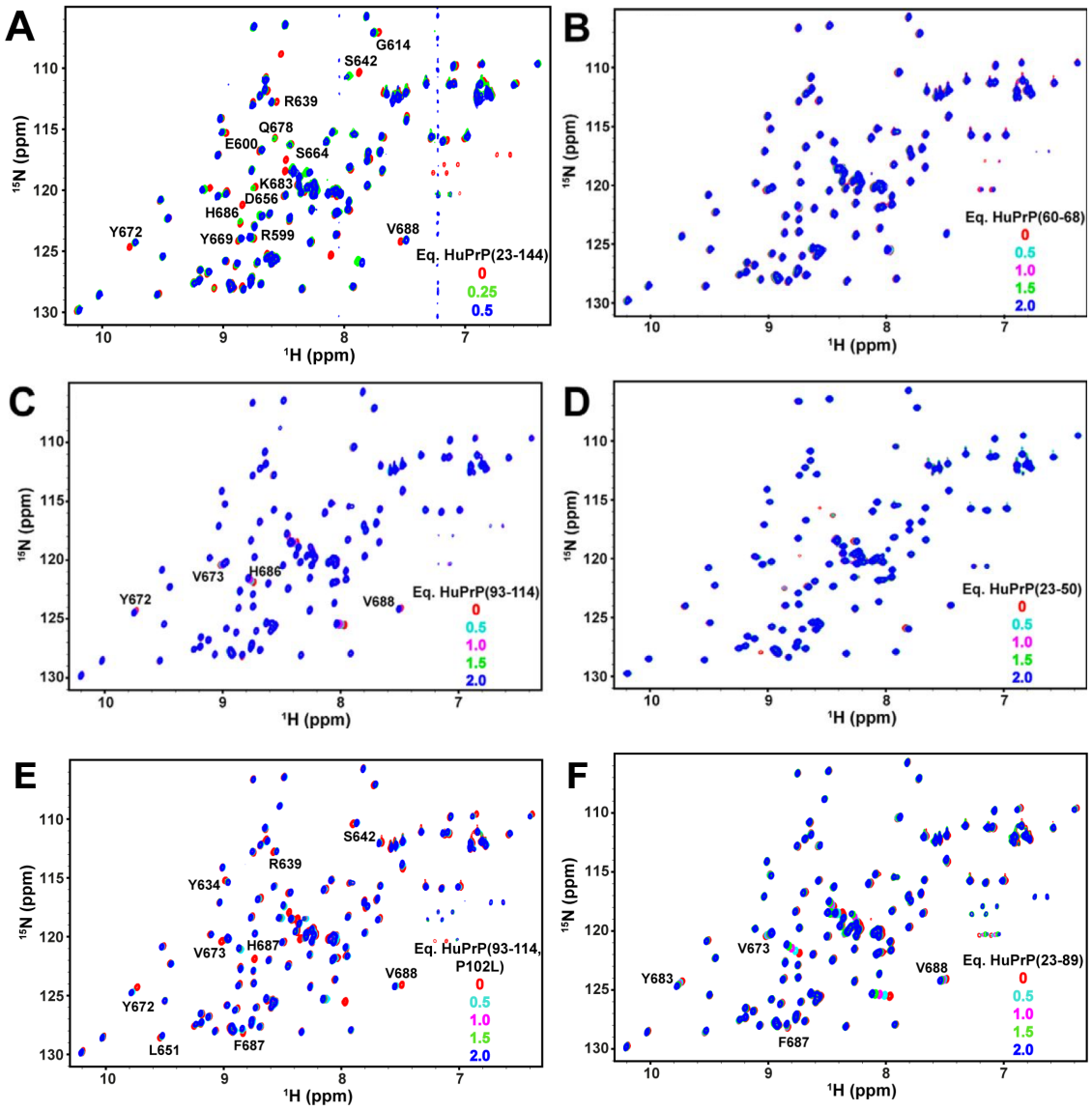

Figure 3.12. Overlays of ^{15}N HSQC spectra of FNIII2 domain in the presence of peptides originating from HuPrP at pH 6. A, HuPrP(23–144). B, HuPrP(60-68). C, HuPrP(93–114). D, HuPrP(23-50). E, HuPrP(93–114, P102L). F, HuPrP(23-89). The HuPrP peptide to FNIII2 equivalents are indicated with the corresponding spectra.

Titrations with peptides HuPrP(23-144), HuPrP(23-89) and HuPrP(93-114, P102L) resulted in biggest Δδ(H,N) of FNIII2 domain. The biggest Δδ(H,N) were observed for residues Tyr669, Val673, His686, Phe687 and Val688 of FNIII2 domain. Other cross-peaks of FNIII2 domain

exhibit negligible chemical shift changes. Detailed analysis of Δδ(H,N) of FNIII2 domain presented in **Figure 3.13** together with peculiarities of line-width broadening led us to conclude that residues Tyr669, Val673, His686, Phe687 and Val688 of FNIII2 domain are involved in interaction with HuPrP.

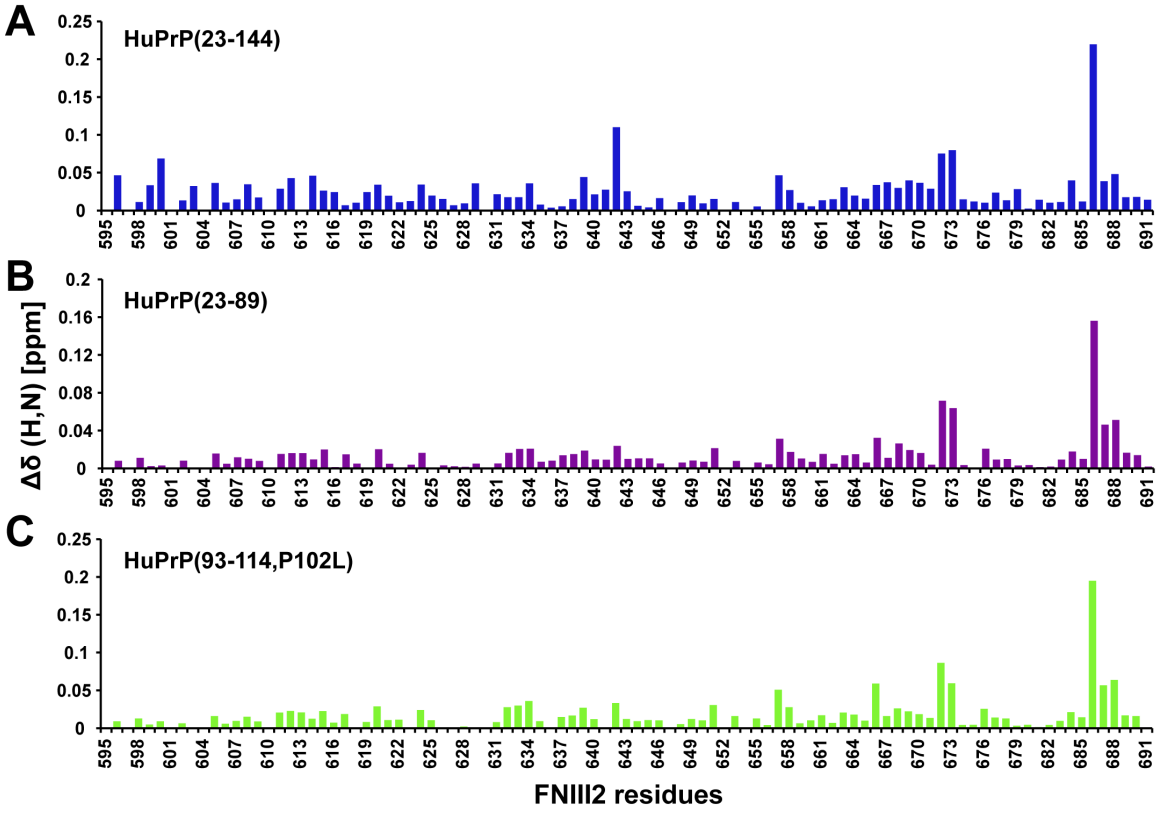

Figure 3.13. Chemical shift changes Δδ(H,N) for FNIII2 domain upon interaction with peptides originating from HuPrP at pH 6.0. (**A**) HuPrP(23-144) peptide at ratio 1:0.5, (**B**) HuPrP(93-114, P102L) at ratio 1:2 and (**C**) HuPrP(23-89) at ratio 1:2. Δδ(H,N) were calculated according equation 1.

Since peptide HuPrP(93-114, P102L) exhibited the strongest interactions with FNIII2 domain we examined the effects of interaction on the peptide as well. ^{15}N-HSQC, NOESY, TOCSY, ^{13}C-HSQC aliphatic and aromatic spectra were used for chemical shift assignment of unlabelled peptide. ^{13}C-^{15}N ω_1 filtered 2D NOESY/TOCSY and ^{13}C-^{15}N ω_1 filtered 3D ^{15}N-HSQC-NOESY were used to determine inter- and intramolecular contacts in complex. Upon binding no intermolecular contacts were observed in ^{13}C-^{15}N ω_1 filtered 2D NOESY. The largest intramolecular chemical shift changes were observed for cross-peaks in ^{13}C-^{15}N ω_1 filtered 2D TOCSY of amino acids Trp99, His111, Met112 and Ala113 of HuPrP(93-114, P102L).

Experimental data therefore indicate that amino acids Tyr669, Val673, His686, Phe687 and Val688 of FNIII2 domain and Trp99, His111, Met112 and Ala113 of HuPrP(93-114, P102L) are most probably involved in the interaction of NCAM domain and wt HuPrP. This data was used

as docking restraints for HADDOCK calculation [220]. 131 lowest-energy structures were grouped into 13 clusters according to RMSD. The numbers of structures in the best 10 clusters varied from 4 to 34 with their HADDOCK scores ranged from 71.8 to 53.5. The clusters could be split into two groups of similar size. The first model describes interactions between Trp99 on HuPrP(93-114, P102L) and FNIII2 domain while the second one describes interactions of His111-Ala113 with HuPrP(93-114, P102L) and FNIII2 domain (**Figure 3.14**).

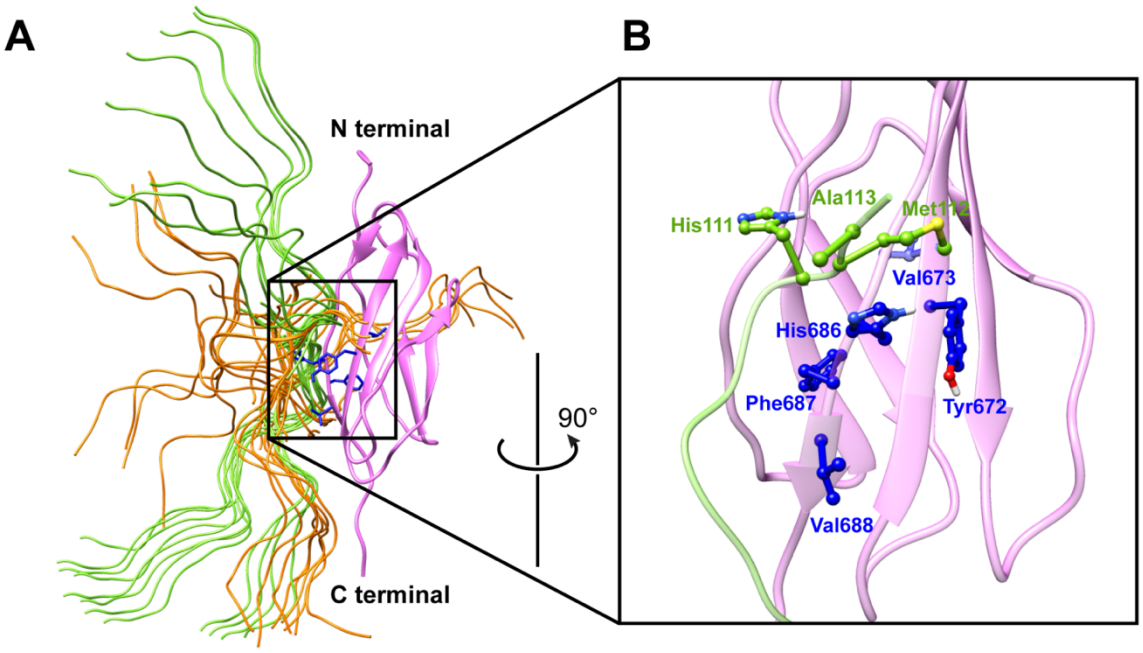

Figure 3.14. Low-resolution model of complex between FNIII2 domain and HuPrP(93-114, P102L). **(A)** Ensemble of 40 models of complex between FNIII2 domain (pink) and HuPrP(93-114, P102L) (green and orange if it interacts with His111-Ala113 and W99, respectively) clustered by HADDOCK program (4 models from each of 10 clusters). **(B)** Enlarged binding region of the best HADDOCK model of FNIII2 domain – HuPrP(93-114, P102L) complex. Amino acids involved in the interaction are presented with balls and sticks (FNIII2 domain in blue, HuPrP(93-114, P102L) in green).

3.2 Understanding the role of copper in prion conversion and susceptibility

Copper coordination to the non-octarepeat region has garnered interest due to the possibility that this interaction may impact prion conversion. We used extended X-ray absorption fine (EXAFS) spectroscopy, cell-biology approaches and molecular dynamic (MD) simulations to study copper coordination at pH 5.5 and 7.0 in human PrP^C constructs, either wild-type (WT) or carrying pathological mutations.

EXAFS spectroscopy is a powerful tool to investigate both local structure and dynamics on a wide class of metal-containing proteins. This technique is very sensitive to the coordination geometry of an absorbing atom and thus allows the measurement of bond distances and angles of the surrounding atomic cluster with atomic resolution, typically within 5 Å or less of the element of interest. Compared with diffraction-based methods, EXAFS generally does not provide three-dimensional information, but it can provide improved precision in atomic positions and it can also provide structural information on solutions.

We show that mutations and pH cause modifications of copper coordination in the non-octarepeat region. In the WT at pH 5.5, copper is anchored to His96 and His111, while at pH 7, it is coordinated by His111. Pathological point mutations alter the copper coordination at acidic conditions where the metal is anchored to His111.

As model systems for the mutants we used Q212P, P102L –the prototypical GSS mutation [221]- and H96Y –an artificial mutation devoid of one His residue involved in copper binding. EXAFS data clearly highlighted modifications of the non-OR copper-binding site induced by these mutations.

To understand the physiological implications of our EXAFS data, we performed *in vitro* and cell-based approaches. We found that H96Y mutation largely promoted prion conversion, PrP accumulation in the endosomal compartments, and generation of *bona fide* infectious prion material (*e.g.* displaying partial PK-resistance and the ability to perform seeded aggregation *in vitro* and in cell).

Finally, MD simulations were used to hypothesize possible structural consequences on the HuPrP structure caused by an altered copper coordination in the non-OR region. In our simulations we predicted structural facets of WT HuPrP(90-231) coordinating Cu(II) *via* either H111 or both H96 and H111. Comparison of trajectories showed that removal of H96 ligand from the Cu(II) coordination results in β-sheet enrichment in the segment spanning the non-OR region and palindromic motif.

Our study highlights the importance of the non-OR region for prion conversion and proposes a model in which PrP^C coordinating copper with one His residue may render PrP^C more prone to prion conversion at acidic pH condition.

3.2.1 Copper coordination in the non-OR region of WT HuPrP

A previous investigation XAS was used to determine the atomic structure of non-OR copper-binding site in the WT HuPrP(90-231) [164]; in this thesis work XAS experiments at the Cu K-edge were carried out at pH 5.5 and the structure of the binding site of both Cu(II) and Cu(I) was

found to be identical. Quantitative analysis of the EXAFS spectra indicated that in both oxidation states, copper ion is coordinated by two His residues (H96 and H111 with Cu-N distance of 1.98(2) Å), by two low Z ligands (either oxygen or nitrogen atoms at 1.98 (1.99) Å) and by one sulphur scatterer at longer distance (*i.e.* 3.25 Å) [164].

To highlight the effect of pH on the local coordination of the copper ion, XAS spectra of both Cu(II) and Cu(I) HuPrP(90-231) complexes were collected at pH 7.0 (**Figure 3.15**). While at pH 5.5 the EXAFS spectra are almost identical for both copper oxidation states, at pH 7.0 EXAFS signals show markedly different features over the full *k*-range. The quantitative analysis of the EXAFS data indicates that at pH 7.0 only a single His coordinates the metal ion in both oxidation states, thus suggesting that one of the two His residues (H96 or H111) moves away from the metal.

EXAFS data concerning Cu(II)-HuPrP(90-231) at pH 7.0 could be modeled as a four coordinate copper center with one His at 1.99(2) Å, and three N/O scatterers at 1.99(4) Å with a more distant sulphur scatterers at 3.47(4) Å. As far as the Cu(I)-HuPrP(90-231) protein is concerned, the EXAFS analysis revealed a three-fold coordination with one His at 1.98(2) Å, one N/O scatterers at 2.00(2) Å and one sulphur scatterer at 2.27(4) Å. In this case one Met residue enters the Cu(I) first coordination shell, similarly to what previously found at acidic pH value [164].

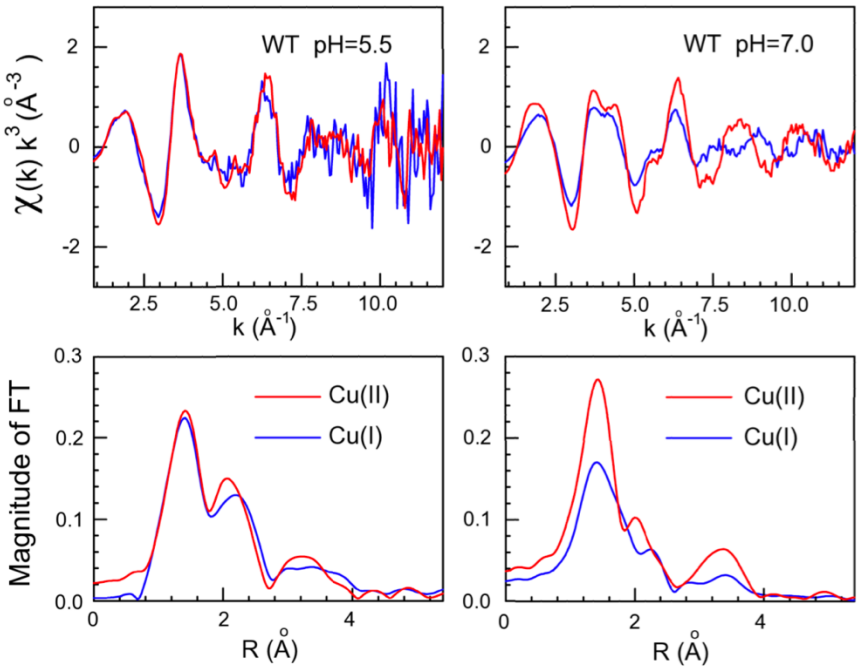

Figure 3.15. Copper coordination in the non-OR region of WT and H96Y HuPrP. k^3-weighted EXAFS spectra and Fourier transforms of the experimental data of Cu(II) and Cu(I) bound to WT HuPrP(90-231) at pH 5.5 and 7.0.

3.2.2 Copper coordination in H96Y, P102L and Q212P HuPrP mutants

The Cu(II) local coordination structure in the H96Y mutant was investigated both at pH 5.5 and 7.0 values. At pH 5.5, the Cu K-edge EXAFS data for H96Y, compared to the WT protein, exhibited a clear modification in the coordination environment. This variation is explained by the existence of a single His in the non-OR region of the H96Y mutant, hampering the coordination of the Cu(II) ion with two His residues (**Figure 3.16**). Conversely, at pH 7.0 the EXAFS spectra of the H96Y mutant and WT proteins are almost identical, thus suggesting that H111 is involved in the copper binding site in both cases. In addition, the EXAFS data showed that the H96Y mutant maintains the same coordination environment around the Cu(II) ion when increasing pH from 5.5 to 7.0. The analysis of the EXAFS data revealed the presence of a four coordinate copper center almost identical to that of the WT protein at pH 7.0, with the H111 residue at 2.00 (2) Å from the ion (**Appendix I, Table S1**). The structures of Cu(II) and Cu(I) binding sites were also investigated in Q212P and P102L HuPrP mutants at both pH 5.5 and 7.0 values (**Figure 3.17 A-B**). The EXAFS data of the mutants share the same coordination pattern observed for the WT at pH 7.0, where the copper ion is coordinated by a single His, namely H111 (**Appendix I, Table S1**). In conclusion, while in the WT the copper ion -at both oxidative states- changes coordination losing the contact with H96 at pH 7.0 (**Figure 3.17 C**), in the mutants copper is bound only to H111 independently of the pH (**Figure 3.17 D**).

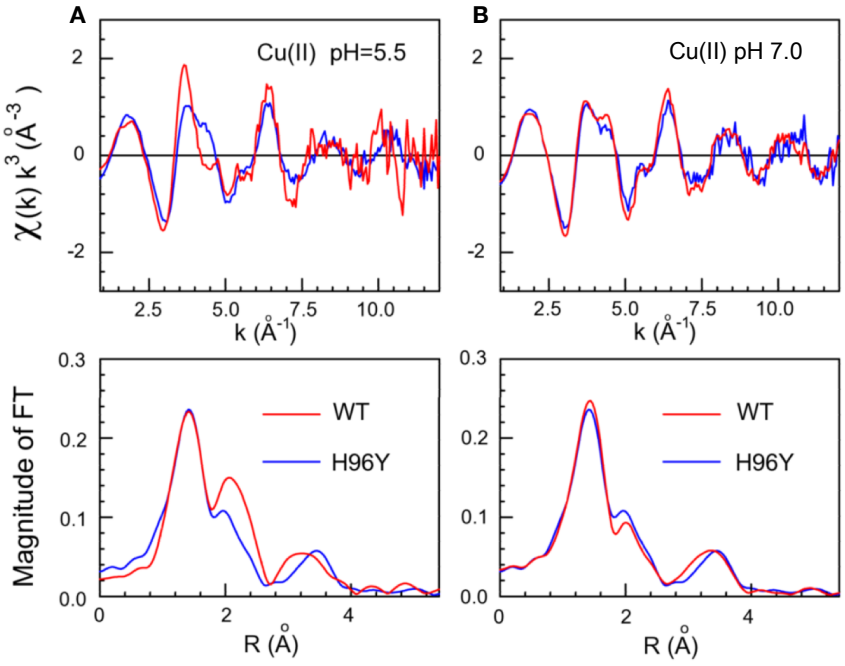

Figure 3.16. Copper coordination in the non-OR region of H96Y HuPrP. k^3-weighted EXAFS spectra and Fourier transforms of the experimental data of Cu(II) and Cu(I) bound to WT HuPrP(90-231) at pH 5.5 and 7.0 (**A**), and of Cu(II) bound to WT HuPrP(90-231) and H96Y at pH 5.5 and 7.0 (**B**).

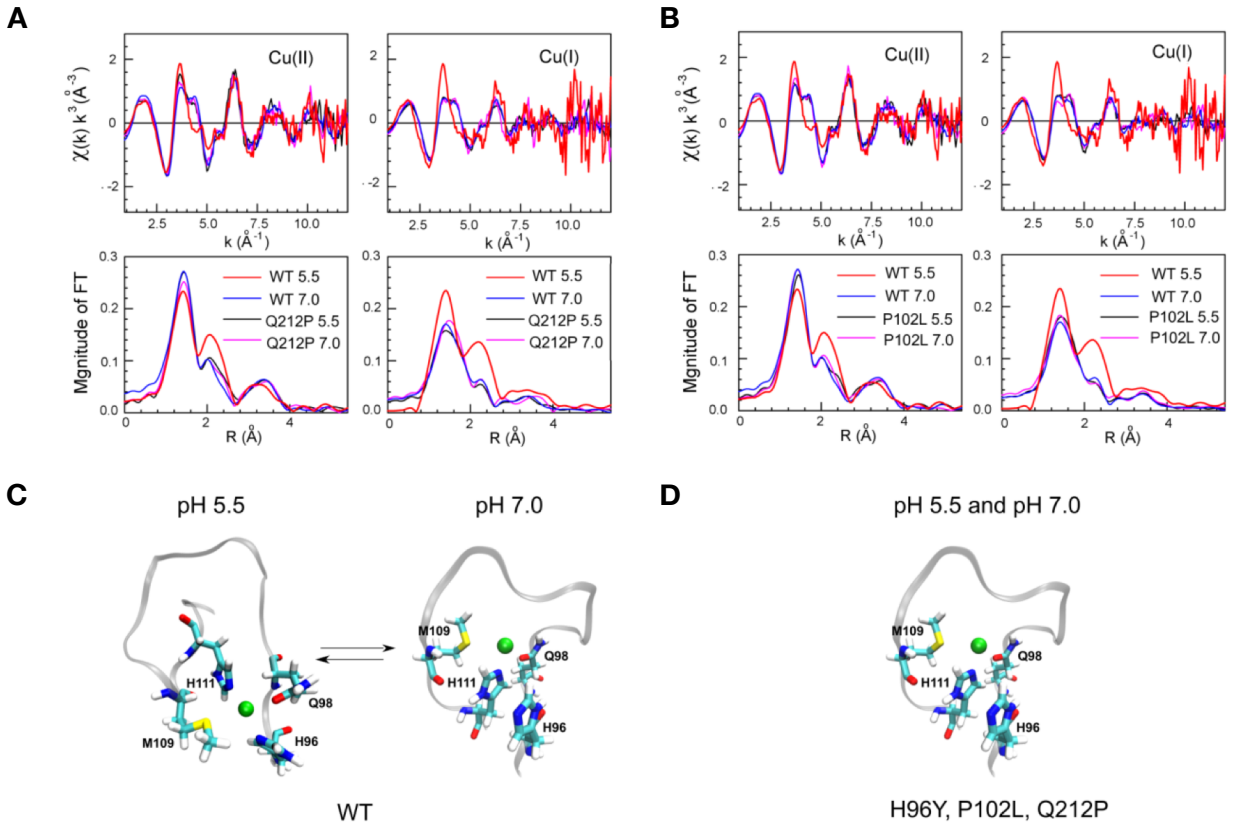

Figure 3.17. Comparison between copper K-edge experimental data of pathological Q212P, P102L and WT HuPrP. k^3-weighted EXAFS spectra and Fourier transforms of Cu(II) and Cu(I) bound to WT HuPrP(90-231) and Q212P at pH 5.5 and 7.0 (**A**) and of Cu(II) and Cu(I) bound to WT HuPrP(90-231) and P102L at pH 5.5 and 7.0 (**B**). Schematic representations of copper binding sites in the WT HuPrP(90-231) (**C**) and in the mutants (**D**) at both pH 5.5 and 7.0. Green spheres identify a single cupper ion at both oxidative states.

3.2.3 The H96Y mutation promotes prion conversion in neuroblastoma cells

The observed structural differences in the copper coordination among WT and pathological mutants at pH 5.5 may have relevant physiological implications since this alteration in the copper binding site might trigger PrP^C to PrP^{Sc} conversion. Hence, the non-OR region could be an important "hot spot" for prion conversion.

We first investigated the effect on prion replication of single His residues along the entire N-terminal PrP^C domain. ScN2a cells were transiently transfected with 3F4-tagged WT and mutant MoPrP constructs in which each individual His located inside the OR and non-OR copper binding sites were substituted by Tyr, thus abolishing the physiological copper binding. The introduction of the 3F4-epitope tag into these constructs makes it possible to discriminate between transfected and endogenous PrP^C. His to Tyr substitutions in MoPrP did not affect the total PrP expression levels (**Figure 3.18 A-B**).

The enhanced resistance to protease digestion is a primary feature to discriminate between PrP^{Sc} and PrP^C in cells chronically infected by prions. The PK digestion profiles showed remarkably different PrP^{Sc} levels among the mutants. While other mutants in the OR region

displayed negligible PK-resistant PrP^{Sc} levels similar to the WT, the H96Y mutant yielded a significantly higher PK-resistant PrP^{Sc} signal, providing a first evidence for the role of H96Y mutation in prion conversion (**Figure 3.18 A-B**).

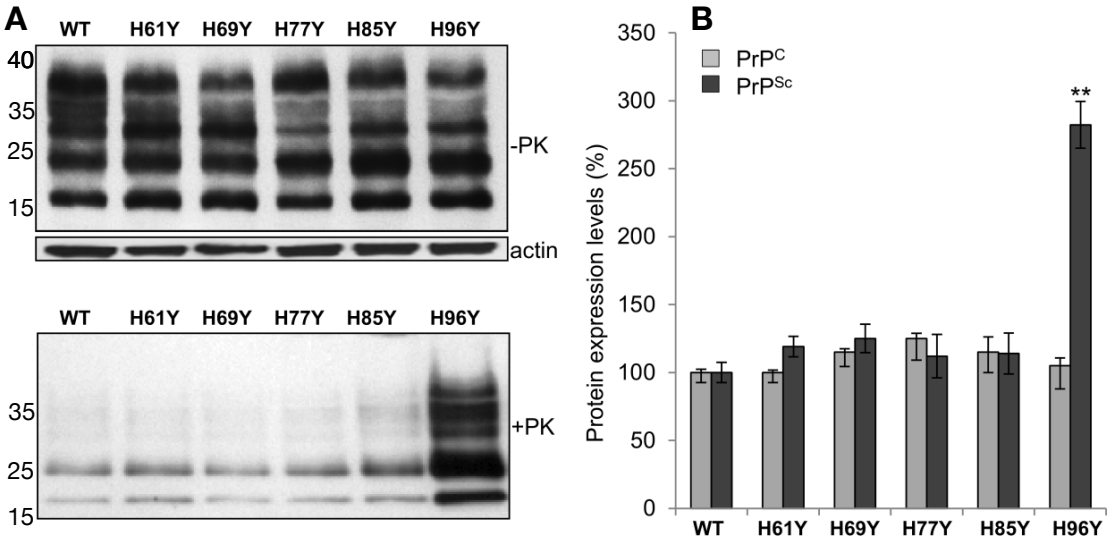

Figure 3.18. The non-OR H96Y mutation promotes prion conversion in ScN2a cells. (**A**) Fifty μg of undigested lysates from ScN2a cells expressing 3F4-tagged WT and mutated MoPrPs was applied to each lane. Five hundred μg of cell lysate was digested with PK (20 μg/mL) at 37°C for 1 hour. MoPrPs were detected by anti-PrP 3F4 antibody. β-actin was used as internal loading control. Arrows (▼) indicate positions on the gels where the blots have been cropped. (**B**) Quantitative analysis of total PrP expression and PrP^{Sc} PK-resistance levels in transfected constructs (n = 4, $^{**}P < 0.005$, by two-tailed *t* test).

Because H96 binds copper, it is likely that the removal of this copper ligand might render PrP^{C} more prone to the conversion in ScN2a cells. Consequently, the absence of copper from the non-OR region could promote this pathological process. To verify this hypothesis, we measured the PrP^{Sc} PK-resistance levels in ScN2a cells transfected either with WT or H96Y MoPrP and treated for 48 hours with cuprizone (CPZ), a well known selective Cu(II) chelator that does not affect cell viability and cannot cross plasma membranes[222]. CPZ treatments on WT ScN2a cells promoted a significantly increase of PrP^{Sc}-PK resistance levels upon 10 to 40 μM CPZ additions, suggesting that PrP^{C} in the apo form is more susceptible to PrP^{Sc} conversion (**Figure 3.19 A-B)**. The PrP^{Sc} levels remained a plateau among control and CPZ-treated H96Y ScN2a cells (**Figure 3.19 A-B)** but always higher than PrP^{Sc} level in the WT cells as also previously presented (**Figure 3.18 A-B**). These data are consistent with the hypothesized mechanism whereby H96Y mutant is *per se* sufficient to generate high amount of PrP^{Sc} molecules. Copper appeared as a pivotal modulator of this process since its absence from PrP^{C} side seems to promote prion conversion.

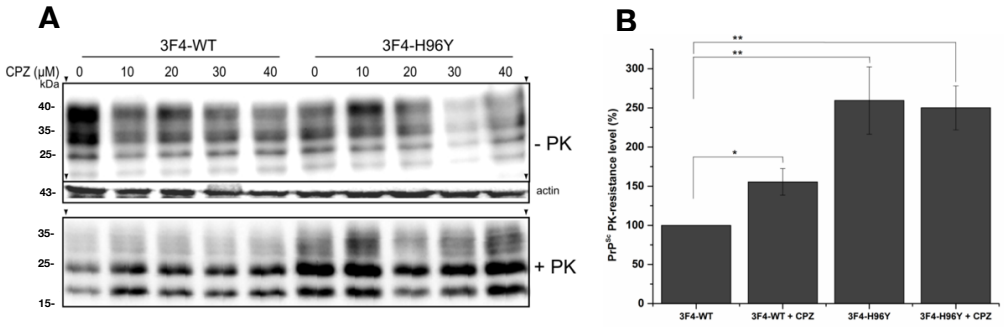

Figure 3.19. The non-OR H96Y mutation promotes prion conversion in ScN2a cells. (**A**) Copper chelation promoted increased PrP^{Sc} formation in 3F4-WT transfected ScN2a cells. CPZ, cuprizone. Full-length blots are presented in the Supplementary Figure S4c-e. (**B**) Quantitative analysis of PrP^{Sc} PK-resistance levels in 3F4-WT and 3F4-H96Y MoPrP transfected ScN2a cells treated with 10 μM CPZ (n = 3, $^{**}P < 0.005$ and $^{*}P < 0.05$).

3.2.4 Biochemical properties of H96Y mutant

We then investigated whether purified PrP^{Sc} from H96Y ScN2a cells shares biochemical properties typical of natural prions, including features such as templating the β-sheet conversion of new PrP molecules, partially PK-resistance, positivity to ThT and ThS staining, cell-to cell transmissibility and intracellular accumulation. We therefore evaluated these properties *in vitro* and in cell-based experiments.

By means of amyloid seeding assay, PTA-isolated PrP^{Sc} seeds from ScN2a cells expressing H96Y mutant were used to promote the conversion of recombinant full-length WT MoPrP. Differently from the WT-PrP^{Sc} seed, we found that the addition of the H96Y-PrP^{Sc} seed significantly promoted MoPrP fibrillization reactions at both pH 5.5 and 7.0 values, resulting in ThT positive kinetics with shorter lag-phases than the controls (**Figure 3.20 A-B**).

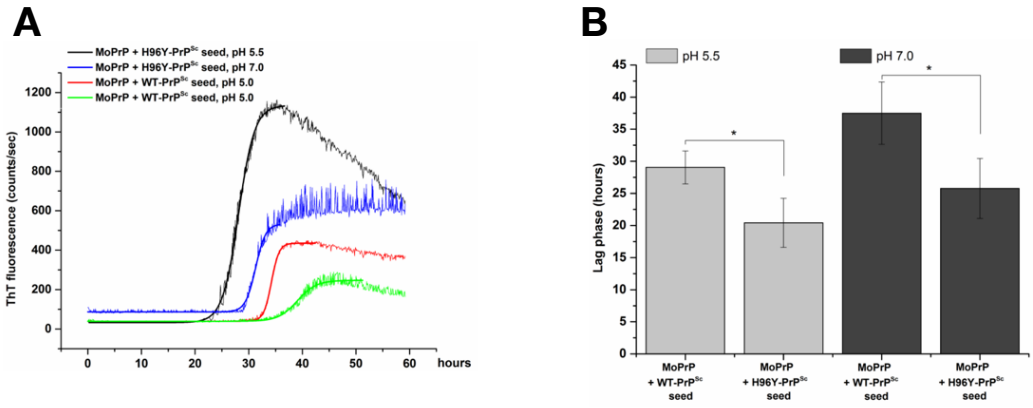

Figure 3.20. The non-OR H96Y mutation promotes prion conversion in ScN2a cells. (**A**) ASA showing the kinetics of MoPrP fibrillization in the presence WT and H96Y-PrP^{Sc} seeds at pH 5.5 and 7.0 and (**B**) the corresponding mean value of the lag phases in hours (n = 4, $^{*}P < 0.05$).

To test the hypothesis that H96Y mutant causes prion formation in non-prion infected cells, N2a cells were transfected with 3F4-WT or H96Y mutant MoPrP and regularly passaged. We found immunoreactive mildly PK-resistant PrP bands –denoted as PrP^{res} or *bona fide* PrP^{Sc} in the absence of *in vivo* assays- starting from passage (P) 4 to P8 (**Figure 3.21 A**). The isolated H96Y-PrP^{res} material observed in P8 was then used as infectious seed in new N2a cells regularly passaged up to P8 (**Figure 3.21 B**). Interestingly, we observed an increment in PrP^{res} levels over passages, thus indicating that H96Y-PrP^{res} seeds induced *de novo* conversion of endogenous PrP^{C} to PK-resistant PrP material (**Figure 3.21 C**).

Subsequently, we evaluated whether N2a cells transfected with H96Y mutant displayed tinctorial features reminiscent of PrP^{Sc}. By using Thioflavin-S (ThS), a specific dye for staining in cells the protein aggregates enriched in amyloid motifs, we found ThS-positive cytoplasmic H96Y mutant deposits similarly to ScN2a (**Figure 3.21 D**).

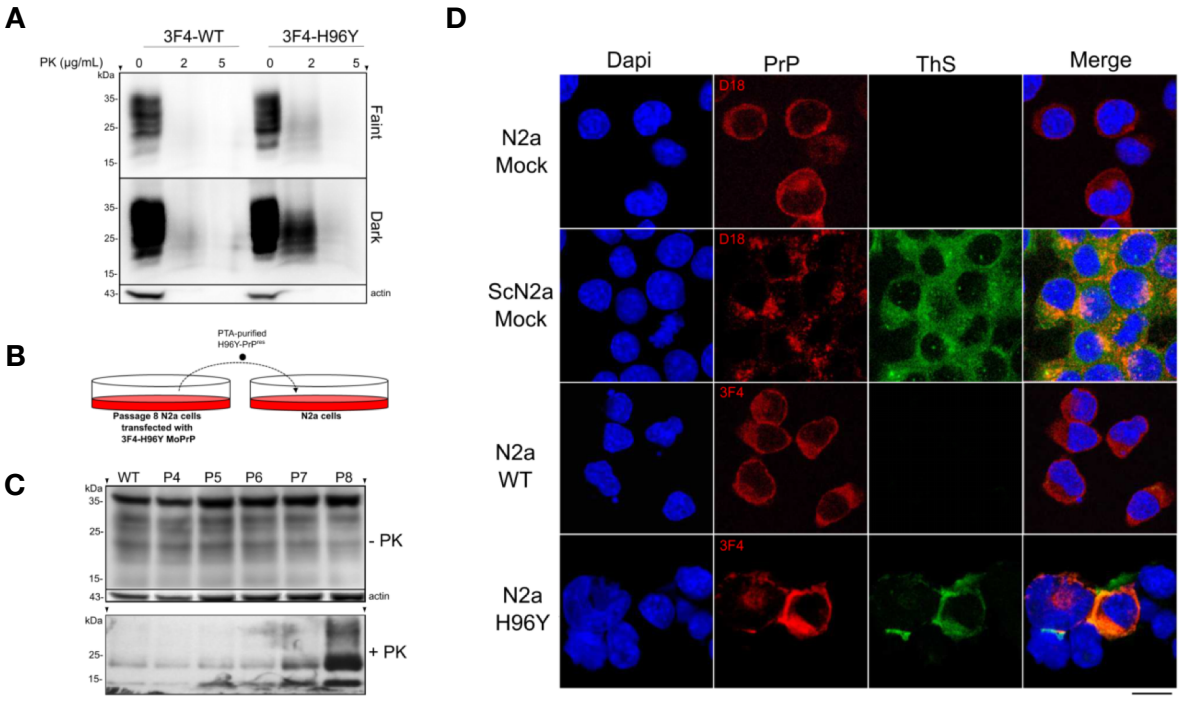

Figure 3.21. Biochemical properties and cellular localization of H96Y mutant in N2a cells. (**A**) The H96Y mutant displays mild PK-resistance when expressed in N2a cells regularly passaged every 7 days up to passage (P) 8. Cell lysates were treated with 2 or 5 µg/mL of PK. Two exposures of the same blot are shown (Faint: 30 sec exposure; Dark: 6 min exposure). PrPs were detected by anti-PrP 3F4 antibody. β-actin is used as internal control. Arrows (▼) indicate positions on the gels where the blots have been cropped. (**B**) Schematic representation of the seeding experiment in N2a cells. (**C**) PTA-extracted PrP^{Sc} from N2a cells transfected with 3F4-H96Y MoPrP were inoculated into N2a cells and regularly passaged every 7 days up to P8. The PrP^{res} detection was assessed by PK digestion (5 µg/mL) through passages. (**D**) ThS-positive H96Y MoPrP aggregates detected in N2a cells. The cells were stained for PrP expression (red) and ThS (green). Untransfected N2a and ScN2a cells (mock) were used as controls. Scale bar: 12 µm.

The observation that the H96Y mutant forms ThS-positive aggregates demands the identification of the primary intracellular compartments where H96Y mutant accumulation occurs. Consistent with previous studies, 3F4-WT MoPrP was found mostly on the cell surface and it was detectable along the ER, endosomal and lysosomal compartments. The WT and H96Y showed co-localization with the ER marker calnexin indicating a correct trafficking through the ER (**Figure 3.23 A**). Biochemical analysis on transfected WT and mutant MoPrP showed that the proteins display the same glycosylation patterns and molecular weight after Endo-H and PNGase-F treatments (**Figure 3.22**). However, we found a significant population of H96Y mutant co-localizing with organelle markers as EEA1 (early endosomes), Tfn (recycling endosomes), M6PR (late endosome) and LAMP2 (lysosome marker) **(Figure 3.23 B)**, suggesting a predominant accumulation of the mutant in the acidic compartments, as reported in previous studies on PrP^{Sc} intracellular accumulation.

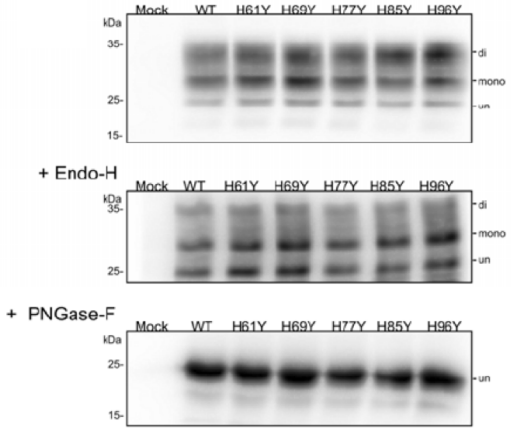

Figure 3.22. The OR and non-OR mutations share the same glycosylation patterns and proteolytic features when treated with Endo-H and PNGase-F as the WT $MoPrP^{C}$. The positions of diglycosylated, monoglycosylated and unglycosylated forms (denoted as di, mono and un) of PrP^{C} are on the right of each WB. PrPs were detected by anti-PrP 3F4 antibody.

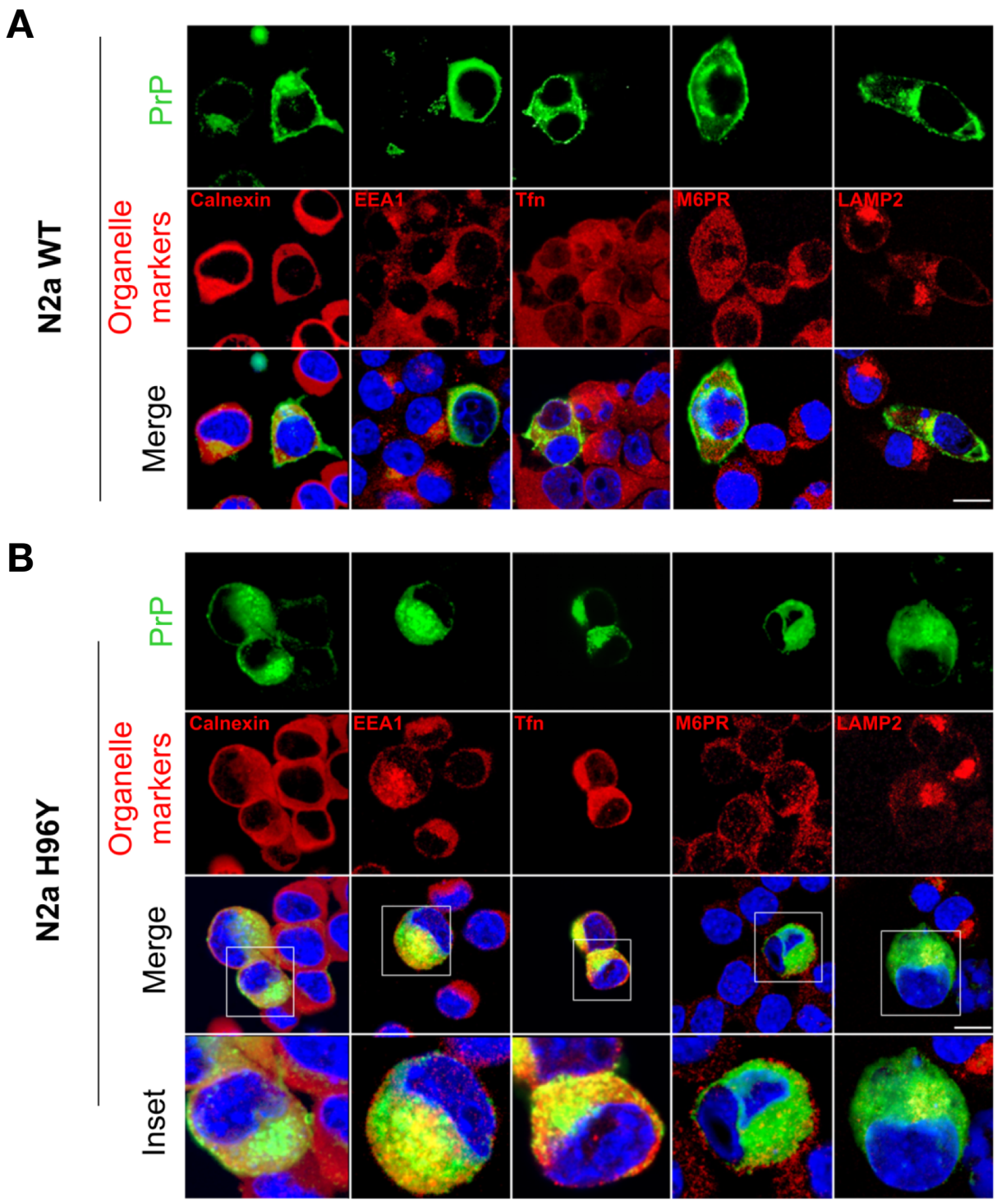

Figure 3.23. The H96Y MoPrP mutant displays intracellular accumulation in the endosomial compartments. PrP localization in N2a cells expressing the 3F4-WT MoPrP (**A**) or H96Y MoPrP (**B**). Nuclei are labeled with DAPI (blue), PrPs are detected by 3F4 antibody (green); organelle markers, such as Calnexin (ER marker), EEA1 (early endosomes marker), Tfn (recycling endosome marker), M6PR (late endosome marker) and LAMP2 (lysosome marker) are labeled in red. Insets in (**B**) shows a magnification of the merged panels (white boxed areas). Scale bars: 12 µm.

3.2.5 Removal of the H96-Cu(II) bond creates transient N-terminal β-sheet structures

To interpret our results from a structural biology point of view, we performed MD simulation studies to predict the structural facets of WT HuPrP(90-231) coordinating Cu(II) either with His96 and His111 or with His111, termed 2His and 1His models, respectively.

The removal of H96 from the Cu(II) coordination sphere did not produce significant changes in the globular domain (residues 128-231), showing similar α_2-α_3 helix orientation as suggested by previous MD and NMR studies[25, 223] (*e.g.* α_2-α_3 helix angle is 51.2° and 49.1° in 2His and 1His models, respectively, while it is 50.9° in NMR structure) (**Figure 3.24 A**). While the C-terminal domain in the two simulation models featured a comparable flexibility (residue-wise Root Mean Square Fluctuation), the N-terminal segment of the 2His model displayed higher flexibility, particularly between residues 98-102 and 116-123 (**Figure 3.24 B** and **Figure 3.25 A**). Additionally, the 2His trajectory yielded a slightly higher radius of gyration as compared to the 1His (1.77±0.08 nm *vs* 1.74±0.04 nm) with more pronounced oscillations (**Figure 3.25 B**) confirming that the N-terminal segment in the 2His trajectory was relatively more disordered.

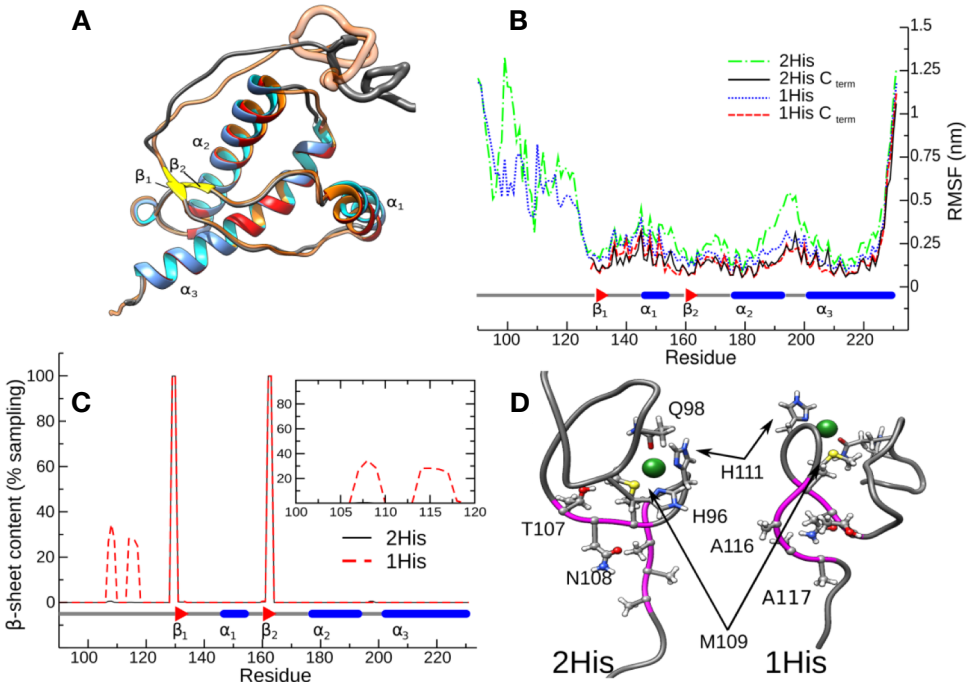

Figure 3.24. **The ion coordination sphere affects HuPrP(90-231) dynamics in MD simulations.** (**A**) Superimposition of average structures sampled in the 2His and 1His trajectories. Helical domains are represented in blue and red in 2His and 1His, respectively, the β_1 and β_2 sheets are in yellow, coils are represented in gray (2His) and orange (1His); the non-OR regions are depicted using a wider transparent ribbon. (**B**) Root Mean Square Fluctuation (RMSF) of residues for the 2His and 1His simulations. RMSF was calculated fitting the coordinates of the complete protein (2His: green dot-dashed line; 1His: blue dotted line) or restricted to the C-terminal domain (2His: black line; 1His: red dashed line). In both simulations the N-terminal domain is, as expected, much more

flexible with the exception of residues 226-231; the 2His simulation apparently features greater fluctuations but the differences fade out when only the stable C terminal domain is considered. Notable exceptions are residues H140 and R151. (**C**) Residue-wise β-sheet content for the 2His and 1His simulation as a percentage of sampling (150.0 ns); the 1His simulation shows unstable β-sheet formation between residues 106-109 and 114-117 (also shown in the inset). (**D**) Comparison of the first centroid obtained by clustering the N-terminal domain Cα atoms in the 2His (left) and 1His (right) simulations; residues 106-109 and 114-117 are shown in ball and stick (backbone is shown in magenta as in **Figure 3.25 A**); copper binding residues H96, Q98 and H111 are shown as sticks and the copper ion as a dark green sphere (note that M109 belongs to both groups); a number of residues forming hydrogen bonds unique to one system are explicitly labeled to improve clarity.

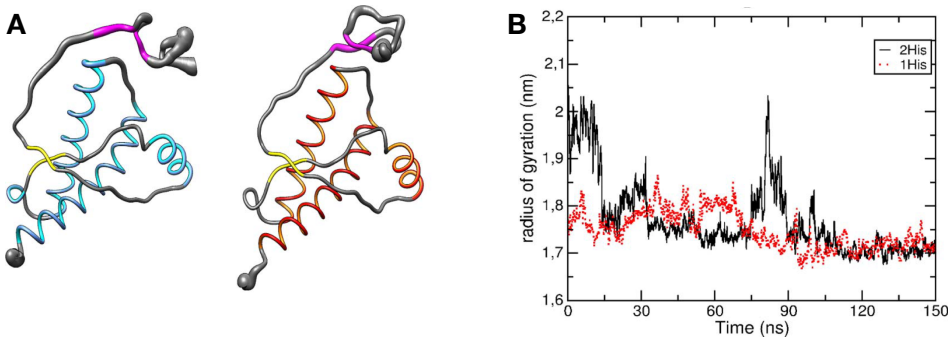

Figure 3.25. (A) Cartoon representation of RMSF. Ribbon width is proportional to fluctuations; the coordinates correspond to those of the first centroid obtained for each trajectory by cluster analysis of the C-terminal domain. The ratio between radius and RMSF is the same in the two models. The average relative orientation of residues 106-109 and 114-117 (colored in magenta) in the 1His system is also clearly observable. (**B**) Radius of gyration (Rg) calculated for the 2His (black) and 1His (red) trajectories. The Rg of the 2His trajectory features transitions between different conformation with Rg up to 2 nm with a lifetime of several nanoseconds each while the Rg of the 1His simulated is stably oscillates around 1.74 nm.

The reduced flexibility of the residues 90-120 segment observed in the 1His trajectory is attributed to the presence of novel hydrogen (H)-bonds and salt bridges, which were uniquely present in the 1His simulation. In particular, we observed that in the 2His system the side-chain of T95 formed H-bond in 89% of sampling with the backbone oxygen of T107, the backbones of T95 and P105 formed a H-bond for 92% of sampling and the side-chains nitrogen atom of Q98 (a residue involved in copper binding) and N100 formed a H-bond in 51% of sampling. In the 1His trajectory, the backbones of residues N108 and A116 formed H-bond in 58% of sampling and the oxydryl group of T107 bound to the backbone of P105 in 62% of sampling. These alterations of the internal hydrogen bond networks in the 1His system created favorable conditions for transient β-sheet motif formations in the segments formed by residues 106-109 and 114-117 (with a lifetime between 20% and 30% of sampling) which were not observed in the 2His trajectory (**Figure 3.24 C** and **Figure 3.25 A**).

A cluster analysis was performed on the N-terminal domain (residues 90-121) of the 2His and 1His trajectories, using 15000 even spaced configurations. More than 80% of the configurations in both trajectories were included in the first cluster (12017 for 2His and 13347 for 1His,

respectively). Comparison of the first centroid structures obtained from the 1His and 2His simulations (**Figure 3.24 D**) shows that in the former case these groups of residues are indeed roughly antiparallel, with the side-chains of residues 106-109 oriented towards the backbone of residues 114-117, *i.e.* in a favorable position for the formation of a small β-sheet. On the other hand, in the 2His trajectory these two clusters form an angle of approximately 90° in most of the sampled structures.

3.2.6 Copper coordination in the non-OR region of prion resistant species

The Cu(II) local coordination structure in the OvPrP ARR and OpPrP has been investigated by X-ray absorption spectroscopy (XAS) at pH 5.5. The EXAFS experimental spectra of these two species are almost identical (**Figure 3.27 B-C**) indicating a similar coordination environment of copper in OvPrP ARR and OpPrP. As showed in the OpPrP amino acidic sequence (**Figure 3.26**) H96 (here in human numbering) is replaced by Y96, therefore only one His residue can coordinate the Cu(II) ion. This result is confirmed by the EXAFS spectra showing markedly different features in the k range around 5 $Å^{-1}$ which is sensitive to the His ligands, as compared to WT HuPrP. Additionally, the intensity of the peaks in the region between 2 and 4 Å of the FT spectra of OvPrP ARR and OpPrP (**Figure 3.27 E-F**) is lower compared to WT HuPrP; this result is compatible with a coordination with one His and an additional amino acidic residue that is chelated to the Cu(II) ion [217]. Note that H96 is present in OvPrP ARR but the EXAFS spectrum of this species is different from that of WT HuPrP, indicating that the Cu(II) ion has a different coordination structure.

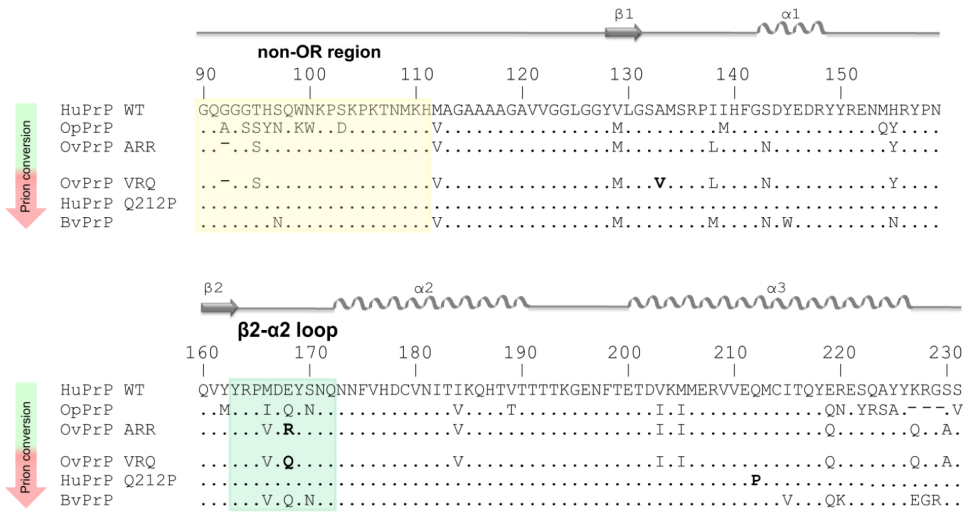

Figure 3.26. Amino acid sequences of HuPrP, OpPrP, OvPrP and BvPrP. Comparison of amino acid sequences and secondary prion protein structure of human (HuPrP; *Homo sapiens*, GenBank accession number AAH22532), opossum (OpPrP; *Monodelphis domestica*, 001035117), ovine with the polymorphic residue position (Q/R) (OvPrP; *Ovis aries*, AFM91142) and bank vole (BvPrP; *Myodes glareolus*, AAL57231). At the top, the secondary structure elements are shown. The yellow box highlights the non-OR copper binding site (residues 90-111) and the green box the β2-α2 loop (residues 163-172).

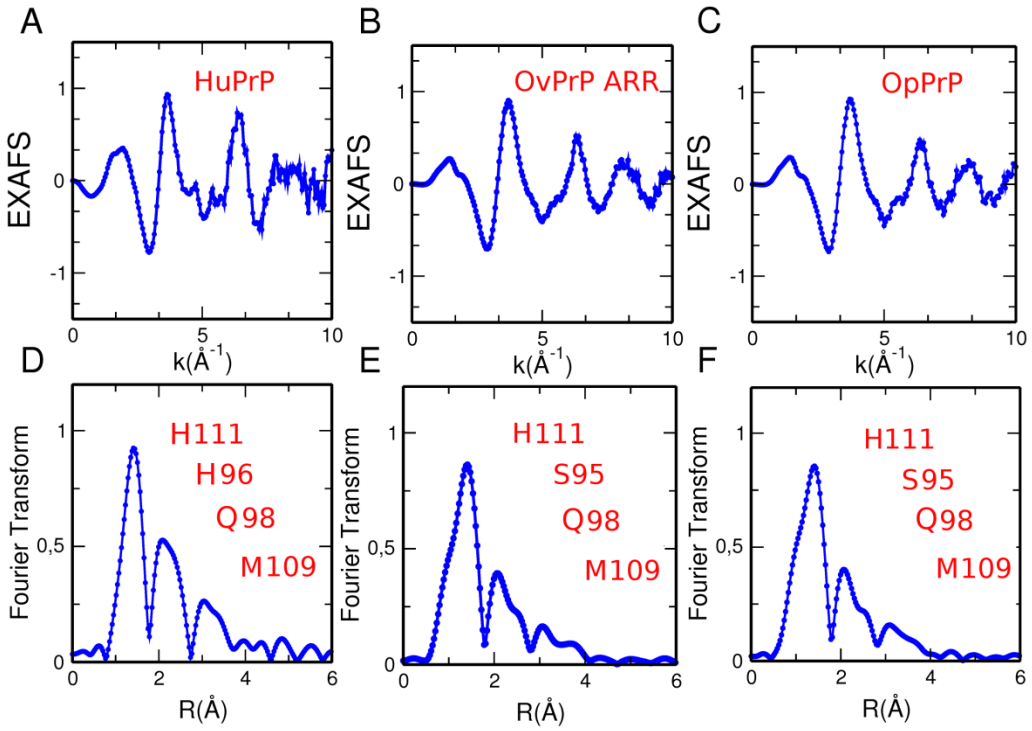

Figure 3.27. Copper coordination in the non-OR region of WT HuPrP, OvPrP ARR and OpPrP. Cu K-edge EXAFS experimental data of (**A**) Cu(II)-bound WT HuPrP, (**B**) Cu(II)-bound OvPrP ARR and (**C**) Cu(II)-bound OpPrP. Non phase-shift-corrected Fourier transforms of the experimental data of (**D**) Cu(II)-bound WT HuPrP, (E) Cu(II)-bound OvPrP ARR and (F) Cu(II)-bound OpPrP calculated in the interval k 2.1-10.0 $Å^{-1}$.

By comparing the amino acidic sequence of OpPrP and OvPrP ARR (**Figure 3.26**) whose EXAFS spectra are equal (**Figure 3.27 B-C**), it is evident that only S95 is present in both systems and it is the only possible ligand of the Cu(II) ion. Starting from these observations a quantitative analysis of the EXAFS data has been carried out using a coordination model around the Cu(II) ion comprising one His, one Ser and one Gln in the equatorial plane. The Ser ligand is chelated to the Cu(II) ion through two oxygen atoms forming a 6-fold ring [217]. This geometry gives rise to multiple scattering (MS) contributions that increase the intensity of the FT higher distance peaks. The fitting procedures applied to the OvPrP ARR and OpPrP EXAFS spectra produced a very good agreement between the theoretical and experimental signals (**Appendix I, Figure S1 A-B**) and the structural parameters obtained from the minimization procedures are listed in **Appendix I, Table S2**. For both OvPrP ARR and OpPrP the EXAFS analysis reveals the existence of a distorted octahedral geometry of the copper center with H111, S95 and Q98 placed in the equatorial positions, and M109 and an oxygen scatterer in the axial sites. We denoted this Cu(II) coordination geometry in OvPrP ARR and OpPrP as type-1 where the copper is tetra-coordinated by Ser, Gln, Met and His residues. Å. A pictorial description of this coordination geometry is shown in **Figure 4.3**.

3.2.7 Copper coordination in the non-OR region of prion susceptible species

The copper coordination was investigated by means of XAS in two susceptible mammalian species, namely OvPrP VRQ and BvPrP. The EXAFS and FT experimental spectra of these systems are similar to those of HuPrP Q212P (**Figure 3.28**) and the low intensity of the second peak of the FT suggests that only one His residue coordinates the Cu(II) ion.

The EXAFS data analyses of OvPrP VRQ and BvPrP have been carried out using the coordination geometry determined for HuPrP Q212P. Also there is agreement between the theoretical and calculated spectra (**Appendix I, Figure S1C-D**), the full list of structural parameters obtained from the minimization procedures is reported in Table S1. The EXAFS data analysis shows the existence of a four-coordinated copper center with one His at 2.00(2) Å, one Gln at 1.99(2) Å, one water molecule at 2.41(3) and one Met at 3.26(4) Å. A pictorial description of this coordination geometry, denoted as type-2, in the susceptible mammalian species is shown in **Figure 4.3**.

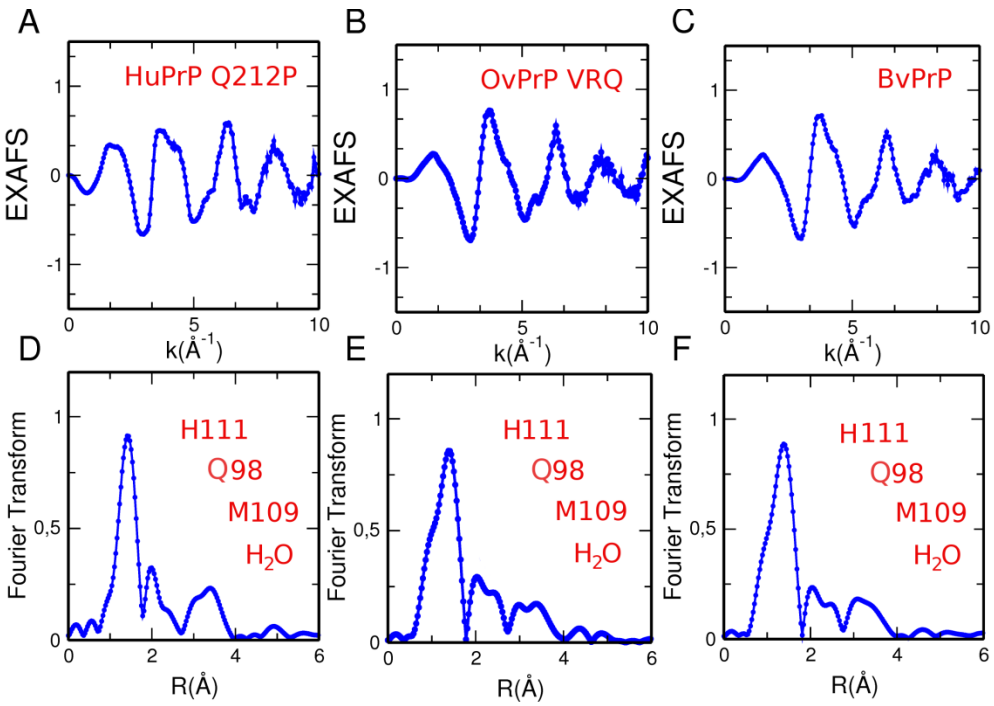

Figure 3.28. Copper coordination in the non-OR region of HuPrP Q212P, OvPrP VRQ and BvPrP. Cu K-edge EXAFS data of (**A**) Cu(II)-bound HuPrP Q212P, (**B**) Cu(II)-bound OvPrP VRQ and (**C**) Cu(II)-bound BvPrP. Non phase-shift-corrected Fourier transforms of the experimental data of (**D**) Cu(II)-bound HuPrP Q212P, (**E**) Cu(II)-bound OvPrP VRQ and (**F**) Cu(II)-bound BvPrP calculated in the interval k 2.1-10.0 Å^{-1}.

CHAPTER IV

DISCUSSION

The conversion of the cellular prion protein PrP^{C} into the infectious isoform (PrP^{Sc}) is the key event in prion diseases. The physiological role of PrP^{C}, as well as the structural and molecular mechanisms leading to PrP^{Sc} conversion, remains one of the greatest gaps in our knowledge of the prion field. Putative roles for PrP^{C} are based on its localization in the central and peripheral nervous systems and on PrP^{C}-interacting molecules or metal ions through its unstructured N-terminal domain.

In the present section, results aimed to analyze the interaction between PrP^{C} and NCAM and PrP^{C} with copper ions will be discussed.

4.1 Identification of the structural determinant responsible for the interaction between PrP^{C} and NCAM

Among the variety of PrP^{C} protein interactors [34], PrP^{C} associates with NCAM *in vivo*. Both molecules have been independently implicated in nervous system development and may play a role in neural stem cells [224, 225]. PrP^{C} recruits to and stabilizes the transmembrane NCAM isoforms (NCAM-180 and NCAM-140) in lipid-rich microdomains. This activates FYN kinase and promotes neurite outgrowth by *cis* and *trans* interactions [218, 226]. The interaction of these two molecules and their relation to specific signaling pathways during neurodevelopment merits further investigation at the structural and molecular level, not the least because the physiological role of PrP^{C} may provide novel insights into the neuropathology of prion diseases. In line of this, the structural basis of the cross-talk between PrP^{C} and NCAM has not been previously investigated.

In this thesis work, we have performed a structural investigation on the interaction between the recombinant FNIII2 domain of NCAM and different peptides originating from N-terminal human PrP^{C} using different experimental approaches.

The *in vitro* experiments designed to confirm the co-localization of PrP^{C} and NCAM in hippocampal neuron cultures led us toward a better understanding of this interaction. We have

identified the HuPrP and MoPrP segments able to interact with the FNIII1,2 domain by means of SPR experiments. These experiments have unveiled that the N-terminal HuPrP domain mediates the FNIII1,2 domain binding with high affinity.

X-ray approaches have been previously applied to better understand the structural properties of the FNIII1,2 domain [227]. Interestingly, the comparison between the FNIII2 NMR structure and the corresponding x-ray structure revealed local structural differences in the length of β-strands. Although the NMR structure features two short β-strands (A and D) on one protein side and four β-strands (B, C, E, and F) on the other, the x-ray structure is characterized by seven strands (**Figure 4.1**). Structural discrepancies between diffraction and NMR data are to be expected considering the differences of the two methods in terms of spatial distribution of the molecules in the sample and time scales accessible to each method. Notably, solution NMR data represent an average over semi-randomly oriented molecules in solution detected in a nanosecond-to-second time regime, whereas diffraction data represent an average over molecules arranged in a periodic crystal lattice acquired in a seconds time scale.

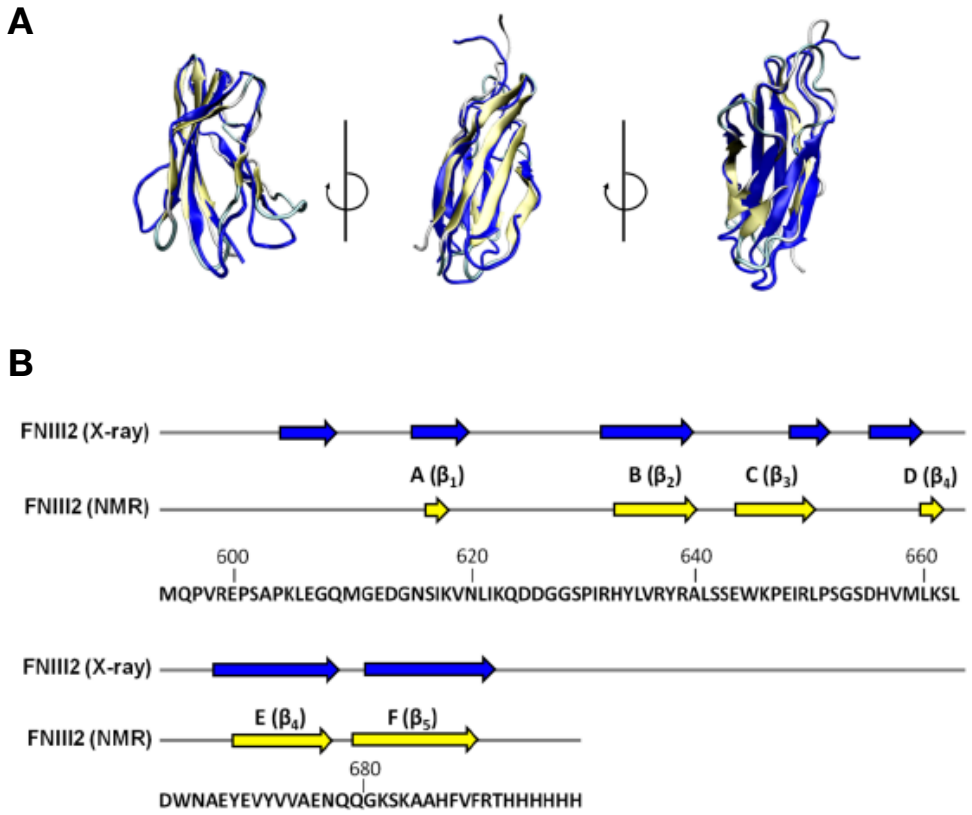

Figure 4.1. Structural comparison between the NMR structure of FNIII2 (in yellow, PDB id 5LKN) and the corresponding X-ray structure (in blue, PDB id 2VKW). In **A** the superimposition of the two 3D structures; in **B** the secondary structure comparison with highlighted the name of the β-strands used for the NMR structure of FNIII2 and the correspodnding amino acid sequence.

We have performed NMR experiments designed to identify the binding sites on the FNIII2 domain and HuPrP N-terminus responsible for the interaction. The implications of our findings are important in prion biology as we provide the first structural evidence that NCAM mediates the interaction with the N-terminal domain of HuPrP through its FNIII1,2 domain. We propose a model where this largely unstructured segment acts as a dynamic element able to recruit NCAM molecules and to mediate physiological processes. We found that the WT HuPrP mediates binding with the FNIII2 domain via its N-terminal segment (residues 23–144). Interestingly, the N terminus contains a glycosaminoglycan (GAG)-binding motif. The binding of GAG is important in prion diseases. This idea is supported by evidence that mutant recombinant PrP binds more GAG, which promotes the aggregation of mutant recombinant PrP more efficiently than HuPrP wild type [228]. Thus, these data corroborate the idea that besides binding metal ions and GAG, the N-terminal domain also mediates *cis* interactions with the NCAM fibronectin domain.

As opposed to WT HuPrP, the P102L mutant seems to possess an extra binding site localized in the segment 93–114, also denoted as the non-octarepeat copper-binding site [164, 216]. Peptides HuPrP(93–114) and HuPrP(93–114, P102L) have the same position in HuPrP N terminus except for the proline-to- leucine substitution at residue 102. Comparison of the (H,N) values for the FNIII2 domain after titration with both HuPrP(93–114) and HuPrP(93–114, P102L) led to a conclusion that the interaction of the latter with the FNIII2 domain is stronger. Thus, we argue that P102L mutation may affect binding with the FNIII2 domain, presumably leading to a stronger interaction with NCAM, which in turn may lead to abnormal Src family kinase activation.

These findings about the interaction between HuPrP and NCAM may have biological relevance on prion conversion. Different compounds, including antibodies or chemical drugs, with high affinity for PrP^{C} have been employed as candidates for therapeutic approaches aimed at inhibiting prion replication. This approach postulates that any PrP^{C} ligand acts as molecular chaperone able to stabilize the protein folding, thus limiting the conversion to PrP^{Sc}. NCAM does not play a direct role during prion formation as observed in NCAM knock-out mice showing the same incubation period when compared with wild-type mice infected by prions [150]. It is plausible that any interference with NCAM-mediated signaling in the diseased brain may favor cell death and inhibit synaptic plasticity. The interactions between PrP^{C} and NCAM could therefore be reduced by accumulation of PrP^{Sc} in the diseased nervous system. Thus, it is conceivable that the association of NCAM to PrP^{C} favors functional signaling pathways through FYN, which is also implicated in synaptic functions. Furthermore, PrP^{C}-NCAM crosstalk is crucial for the coordinated regulation of cell cycle progression and the differentiation of neuronal precursors toward different neuronal phenotypes [229]. We found that this interaction is mediated by the PrP^{C} N-terminus, particularly in the segment from residues 23 to 50 includes four positively charged residues (*i.e.* KKRPK) known to play a role in the PrP^{C} endocytic trafficking and in its localization to lipid rafts [17, 230]. Our study suggests that the interaction between residues 23–50 and the NCAM fibronectin domain may determine the fate of PrP^{C} in the cell surface raft domain. Here PrP^{C} participates in the complex molecular networks and

signaling mechanisms, both cell-intrinsic and cell-extrinsic, that influence cell fate and differentiation. It is worth nothing that involvement of other PrP^C N-terminus regions in the binding with NCAM cannot rule out.

The mechanisms that recruit and assemble different trans-membrane signaling molecules to distinct membrane sub-domains have only started to emerge. In these environments, signaling and scaffolding proteins can self-associate and form dimeric or multimeric assemblies. Protein dimerization has been reported as a common mechanism to cluster downstream signaling components and thereby enhance the signaling cascade [231]. According to a recent model, NCAM is present on the cell surface as *cis* dimers, formed by the interactions between the Ig1 and Ig2 domains [148, 232]. The role of *cis* dimerization in NCAM dimerization is debated, but it is a pre-requisite for NCAM clustering on the cell surface, which in turn results in cell-cell adhesion via *trans* interactions between NCAM clusters.

These data increase the evidence that the largely unstructured N-terminal domain acts as dynamic element able to recruit molecules, i.e. NCAM, and to mediate physiological processes.

4.2 Understanding the role of copper in prion conversion and susceptibility with a special focus on the fifth copper binding site.

Despite numerous investigations, the conversion mechanism(s) leading to PrP^{Sc} formation and transmission remain unclear. NMR-based studies on both Hu and MoPrP structured domains have proposed a role of the β_2-α_2 loop as dynamic "switch" element able to modulate prion conversion and susceptibility of a given specie to TSE [122]. However, the structural rearrangements occurring at the N-terminal region have not yet been clarified due to its intrinsic disorder. As already discussed, the N-terminal domain features several copper binding sites; although there is some contention, the non-OR copper binding site is the highest affinity site for copper in PrP^C [233, 234]. This region attracted interest because of its location adjacent to the palindromic motif sequence AGAAAAGA. This regional proximity raised the question whether copper bound to the non-OR site may have an impact on prion conversion. Indeed, the interaction of copper with a peptide including both the non-OR and the palindromic motif has been shown to induce β-sheet formation and aggregation of this segment [234, 235]. Further in vivo findings have supported the idea that the region encompassing residues 90-125 is involved in prion generation. Moreover, in a previous X-ray study from our laboratory it has been found that this palindromic domain can initiate β-sheet enrichment when HuPrP is crystallized in complex with a Nanobody [40], suggesting that the segment 90-127 may act as alternative N-terminal switch for prion conversion.

In this work, we provide structural and biological evidence that the non-OR region may have pivotal biological implication in prion formation and susceptibility to prion diseases.

In the WT HuPrP Cu(II) and Cu(I) are anchored to His96 and His111 only at pH 5.5, while at pH 7 copper at both oxidative states is coordinated by His111. Conversely, in the mutants (*i.e.*

the GSS-causing Q212P and P102L mutants and the artificial H96Y mutation) copper is bound only to H111 independently of the pH value.

The MD simulations propose a model whereby the molecular switch between the 2His and 1His systems (*i.e.* copper bound to H96 and H111, or only to H111, respectively) may have structural implications. The 1His coordination seems to favor β-sheet enrichment in the region encompassing residues 106-117. At this stage it is unclear how this early β-sheet conversion may drive a complete structural conversion to PrP^{Sc}, but the new structural rearrangements occurring at the palidromic motif might serve as a nucleus for the association of intermolecular β-strands.

To interpret these structural clues in the context of more relevant physiological implications, we used ScN2a and N2a cells transiently expressing 3F4-MoPrP with the substitutions of his residues by tyr residues at N-terminal copper binding sites (OR and non-OR regions) to abolish the binding of copper in these regions. We found that prion replication was not affected by the lack of each histidine in the OR region, in agreement with previous studies, confirming that the deletion of an octapeptide repeat did not lead to prion disease [236]. Conversely, His to Tyr96 substitution removes one crucial copper ligand, thus it may allow to link the effect caused by altered copper coordination with prion conversion. The expression of H96Y mutant highly promotes prion conversion in ScN2a cells and spontaneously generated PrP^{res} together with intracellular MoPrP accumulation in N2a cells. We hypothesize that the non-OR copper-binding site at H96 is much more important for both PrP^{C} function, as shown by the higher affinity for copper binding compared to the OR region [173], and prion propagation and infectivity [237]. Residue H96 is located in a PrP^{Sc} region that is partially resistant to PK, thus copper bound to H96 may have a role during PrP^{Sc} formation even in the absence of the OR region [238]. Based on our findings, we propose that the H96Y mutant may act as other pathogenic mutations located in both N- and C-terminal domains (*e.g.* P102L and Q212P), causing spontaneous prion conversion. Our analysis shows that H96Y mutation induces PrP^{C} accumulation in the acidic endosomal compartments, as observed for other disease-linked mutations [78]. The pH change from neutral to acidic values has been proposed to trigger the PrP^{C} conformational conversion and a change in the balance of distinct internalization mechanisms may promote PrP^{Sc} replication by diverting the protein to distinct intracellular compartments and inhibiting the cellular protein quality control systems [239]. We report here enhanced PK-resistance of the H96Y mutant when expressed in ScN2a cells and its ability to generate *de novo* PrP^{res} in N2a cells.

These findings propose a pivotal role for non-OR region as critical molecular switch for prion conversion **(Figure 4.2)**. We therefore argue that copper bound to the non-OR region may stabilize this segment when coordinated by four amino acid copper centers (*i.e.* His96, His111), preventing misfolding events through transient short and long-range interaction contacts between the 90-127 residues and the C-terminal structured domain. Copper acts as a key modulator of this process since its absence from PrP^{C} side promote prion conversion, as observed in WT ScN2a cells treated with a copper chelator.

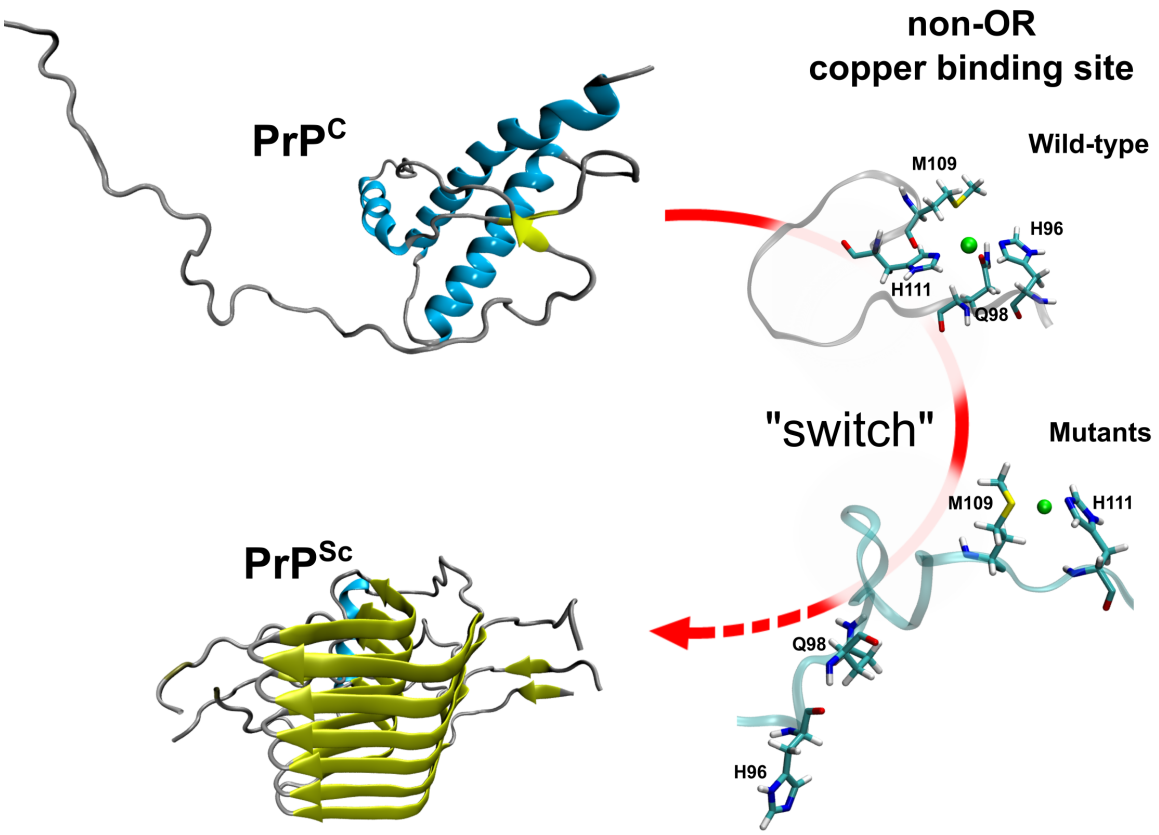

Figure 4.2. Model for the non-OR region molecular switch at acidic pH. PrP^{C} coordinating copper with one His residue in the non-OR region is more prone to the conversion at acidic pH condition. As PrP^{Sc} model we used the HET-s(218-289) 2KJ3 PDB structure.

After assessing the role of the non-OR region in the prion conversion, we expanded our knowledge on Cu(II) coordination in different mammalian PrP^{C}. We analyzed the Cu(II) coordination in both prion resistant (OpPrP and OvPrP ARR) and susceptible (BvPrP and OvPrP VRQ) PrP^{C} species.

In the OpPrP and OvPrP ARR, we found that four residues are surrounding the copper ions, while in BvPrP, OvPrP VRQ and in HuPrP with the pathological point mutations Q212P and P102L the copper is coordinated by three residues.

Based on our data, we prepared two models for Cu(II) coordination in both prion resistant and susceptible species (**Figure 4.3**).

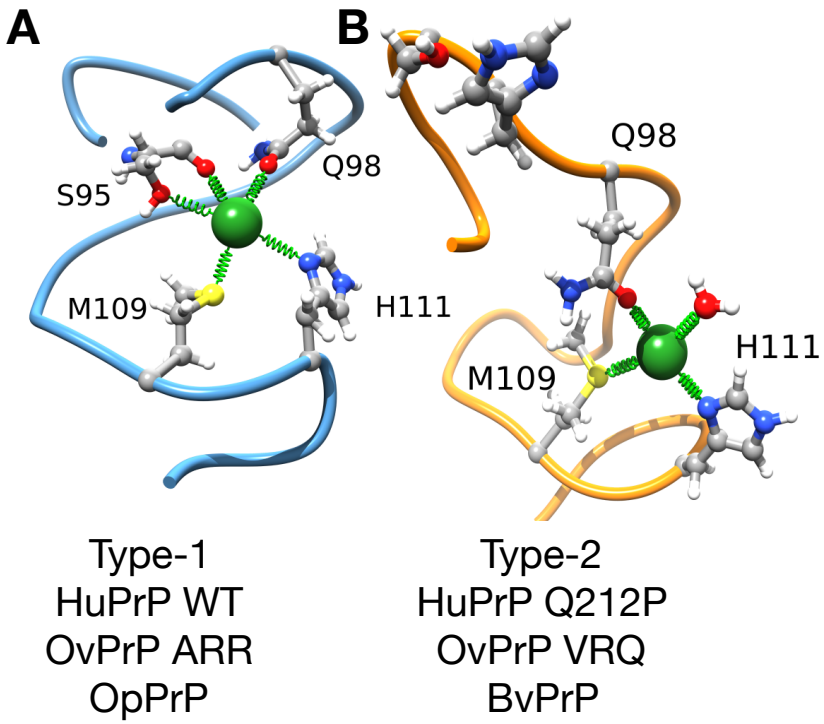

Figure 4.3. Copper coordination models in the non-OR region of the resistant and susceptible species. Schematic representations of copper coordination (A) type-1 and (B) type-2. Blue spheres identify nitrogen atoms, red spheres are oxygen atoms and yellow spheres encode for sulfur atoms. Gray and white spheres represent carbon and hydrogen atoms, respectively.

Type-1 Cu(II) coordination display a closed non-OR region conformation associated with less-susceptible species likely because of higher stability of the PrP^C structure. Instead, in type-2, a water molecule enters the coordination shell, thus leading to a less structured and solvent exposed non-OR region. The more opened conformation of the non-OR region in the type-2 might render the overall PrP^C structure more flexible; therefore we correlate this with higher susceptibility to prion diseases.

Our data highlighted how copper coordination in the non-OR copper binding site may explain the different susceptibility to TSE observed in these mammalian species.

4.3 Conclusions

The present thesis aims at characterizing the role of the PrP^C N-terminal domain in regulating the physiological function of PrP^C and its involvement in the prion conversion.

The flexibility characterizing the unstructured domain qualifies PrP^C as a partially unstructured protein. Important features of the protein N-terminus include the ability to interact with both metal ions and with protein ligands.

In this study we provide a structural and biological evidence that the non-OR region has a crucial role in promoting prion conversion.

In particular, we have shown that a Cu(II) coordination displaying a closed non-OR region conformation is associated with less-susceptible species likely because of higher stability of the PrP^C structure, while a less structured and solvent exposed non-OR region leads to a more opened conformation of the non-OR region that might render the overall PrP^C structure more flexible. We finally correlate the copper coordination in the non-OR copper-binding site with the different susceptibility to TSE observed in these mammalian species (**Figure 4.3**).

Moreover, we provide the first structural evidence that the N-terminal domain of PrP^C interacts with NCAM through its FNIII1,2 domain. We found that this interaction is mediated by the segment from residues 23 to 50 including four positively charged residues (*i.e.* KKRPK) known to play a role in the PrP^C endocytic trafficking and in its localization to lipid rafts [17, 230]. Our study suggests that the interaction between residues 23–50 and the NCAM fibronectin domain may determine the fate of PrP^C in the cell surface raft domain. PrP^C participates in the complex molecular networks and signaling mechanisms, both cell-intrinsic and cell-extrinsic, that influence cell fate and differentiation.

In conclusion, in the present thesis we highlighted how the N-terminus of PrP^C is involved in both metal binding and signaling transduction due to the presence of different epitopes engaged in the binding of metal ions as well as molecules involved in signaling mechanisms such as NCAM (**Figure 4.4**).

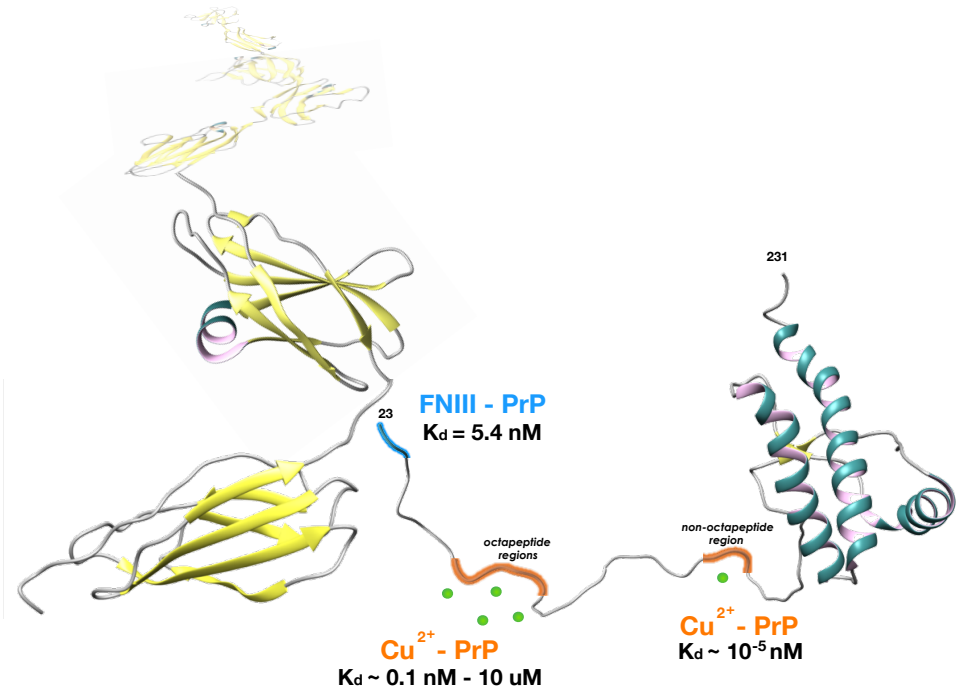

Figure 4.4. PrP^C interaction with copper ions and NCAM. PrP^C interacts with copper ions through the octarepeats and non-octarepeats regions (segments in orange), and with the FNIII1,2 domains of NCAM via the PrP^C 23-50 segment (in blue). Affinity constants are indicated.

APPENDIX I

SUPPLEMENTARY RESULTS

PROTEIN EXPRESSION AND PURIFICATION

1. Prion proteins expression in LB medium.

All MoPrP, HuPrP and other mammalian PrPs variants were cloned into plasmid pET11a. The recombinant proteins were produced in *E. coli* BL21(DE3) in LB medium. As a reference, here we showed results of the HuPrP23-231 WT only.

Large scale protein expression was achieved using a 2 L bioreactor which allows an automated pH, stirrer, temperature and pO2 control. The characteristic fermentation plot of a E. coli BL21(DE3) culture grown in M9 MM is presented in **Figure 1 B**. As we can see from the pO2 curve, bacteria consume oxygen intensively for about 6 hours after induction. The expression in bioreactor allows bacterial yield of 9-10 g/l of paste and a final OD_{600} nm of 7-8. On the basis of expression protocols already established in our laboratory, we confirmed that the PrP expression always results in the formation of insoluble inclusion bodies, even at low temperature and IPTG concentration **(Figure 1 C)**.

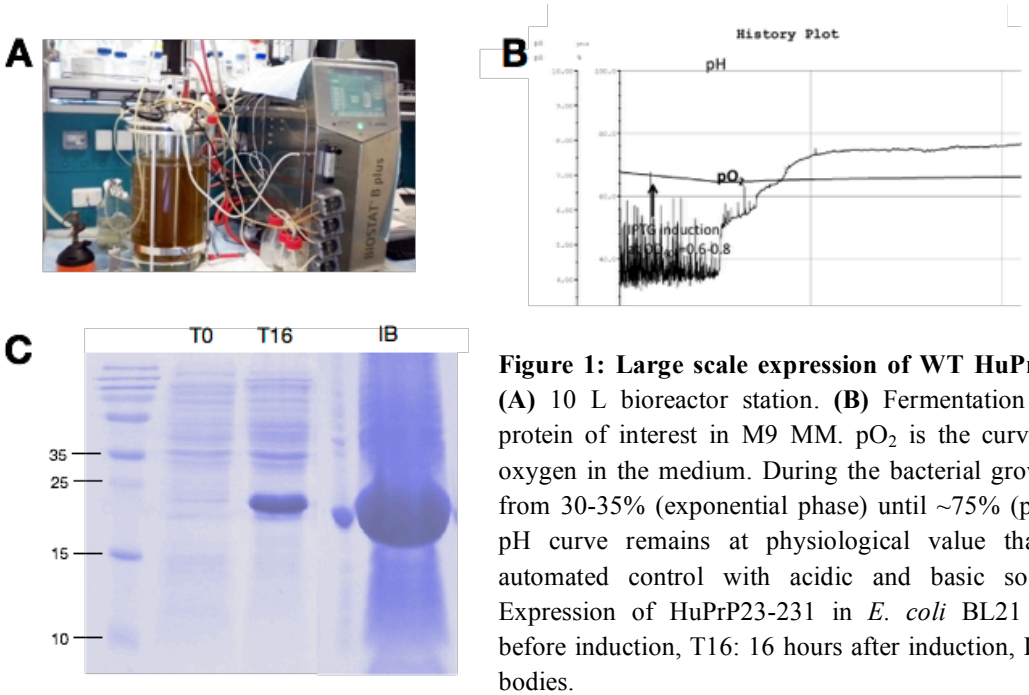

Figure 1: Large scale expression of WT HuPrP (23-231). (A) 10 L bioreactor station. **(B)** Fermentation plot of the protein of interest in M9 MM. pO_2 is the curve of soluble oxygen in the medium. During the bacterial growth, it starts from 30-35% (exponential phase) until ~75% (plateau). The pH curve remains at physiological value thanks to the automated control with acidic and basic solutions. **(C)** Expression of HuPrP23-231 in *E. coli* BL21 (DE3), T0: before induction, T16: 16 hours after induction, IB: inclusion bodies.

2. FNIII1, FNIII2 and FNIII1,2 expression and solubility trials for NMR structural studies

Small scale expression trials in M9 MM aimed at finding the conditions to increase the FNIII1, FNIII2 and FNIII1,2 expression and its solubility in E. coli BL21 (DE3). We evaluated the effect of growth temperature and the effect of IPTG concentration on the expression level at 25°C, 30°C and 37°C (**Figure 2**). We observed that the protein expression results in the soluble fraction (data not shown). We concluded that FNIII1 can be highly and efficiently expressed in M9 MM at 30°C at IPTG concentration of 0.5-0.75 mM, while FNIII2 and FNIII1,2 at 30°C at IPTG concentration of 0.25 mM. Unfortunately, we experienced solubility problems with FNIII1, therefore we were not able to use it for NMR experiments.

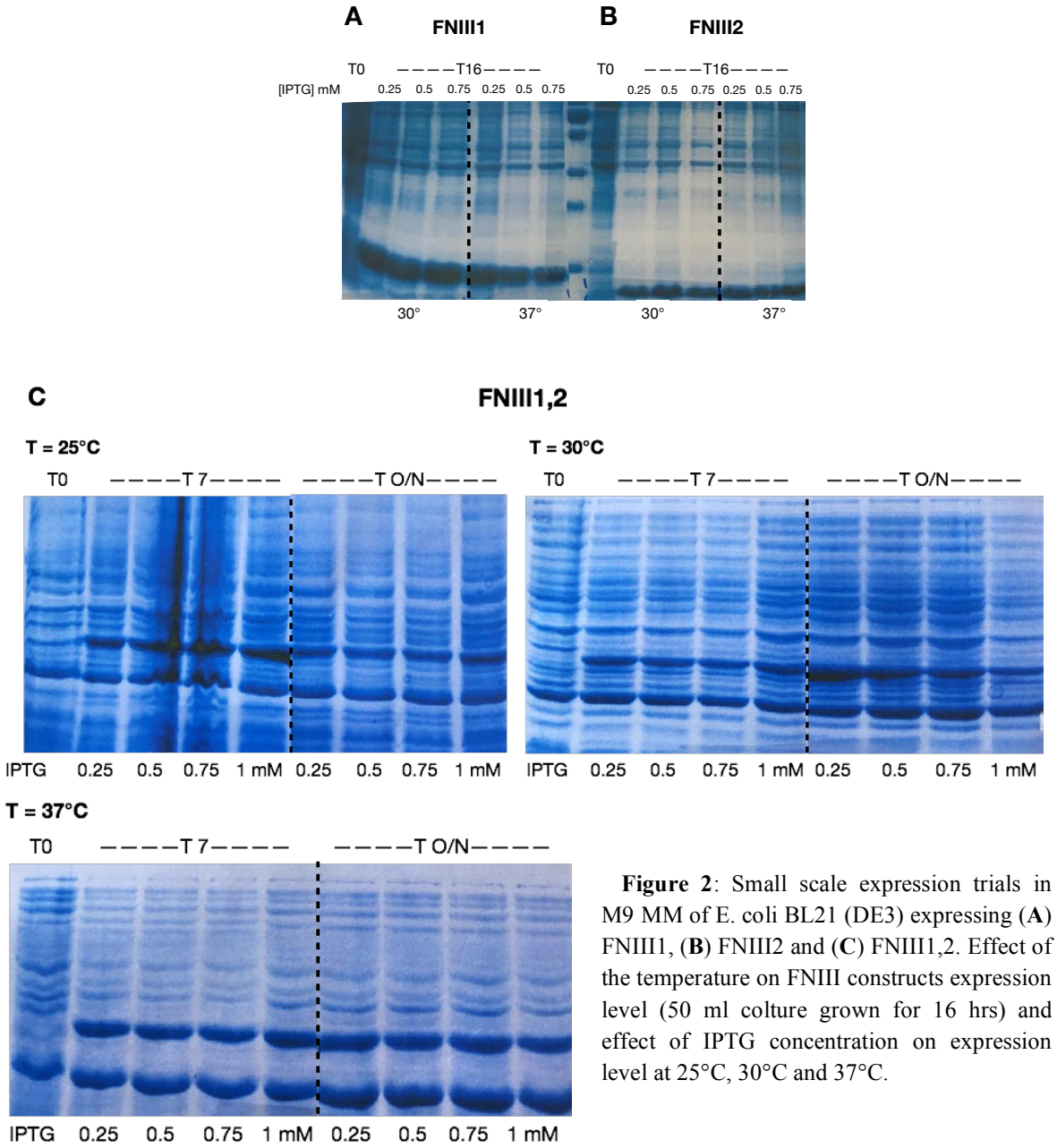

Figure 2: Small scale expression trials in M9 MM of E. coli BL21 (DE3) expressing (**A**) FNIII1, (**B**) FNIII2 and (**C**) FNIII1,2. Effect of the temperature on FNIII constructs expression level (50 ml colture grown for 16 hrs) and effect of IPTG concentration on expression level at 25°C, 30°C and 37°C.

3. Protein purifications and refolding

The soluble FNIII2 for NMR studies contained an uncleavable Histag at the C-terminus and were purified using HIMAC. The protein was virtually pure after this purification step (**Figure 3 A**). FNIII2 was assessed as a monodisperse peak using an analytical gel filtration column (Superdex 200-10/300), equilibrated in 25 mM NaOAc, 0.2 M NaCl, pH 6.0 (**Figure 3 B**).

About the recombinant PrPs, the main advantages of the expression of prion proteins as insoluble inclusion bodies are the high levels of expression and the possibility to easily purify extremely pure proteins after the first purification step. However, inclusion bodies need to be solubilized in strong denaturant agents (such as GndHCl or urea) before use. Therefore, all the purifications were achieved in non-native condition due to the presence of 2-6 M GndHCl in the buffers. Another aspect limiting our work with proteins expressed as inclusion bodies is the refolding process. This step always resulted in protein precipitations (approximately 50% of the total amount of refolded protein), independently of PrPs or TEV protease, which required additional re-solubilization steps with GndHCl of protein precipitates and refolding.

In **Figure 3 D-F** the purified proteins used for NMR and EXAFS experiments.

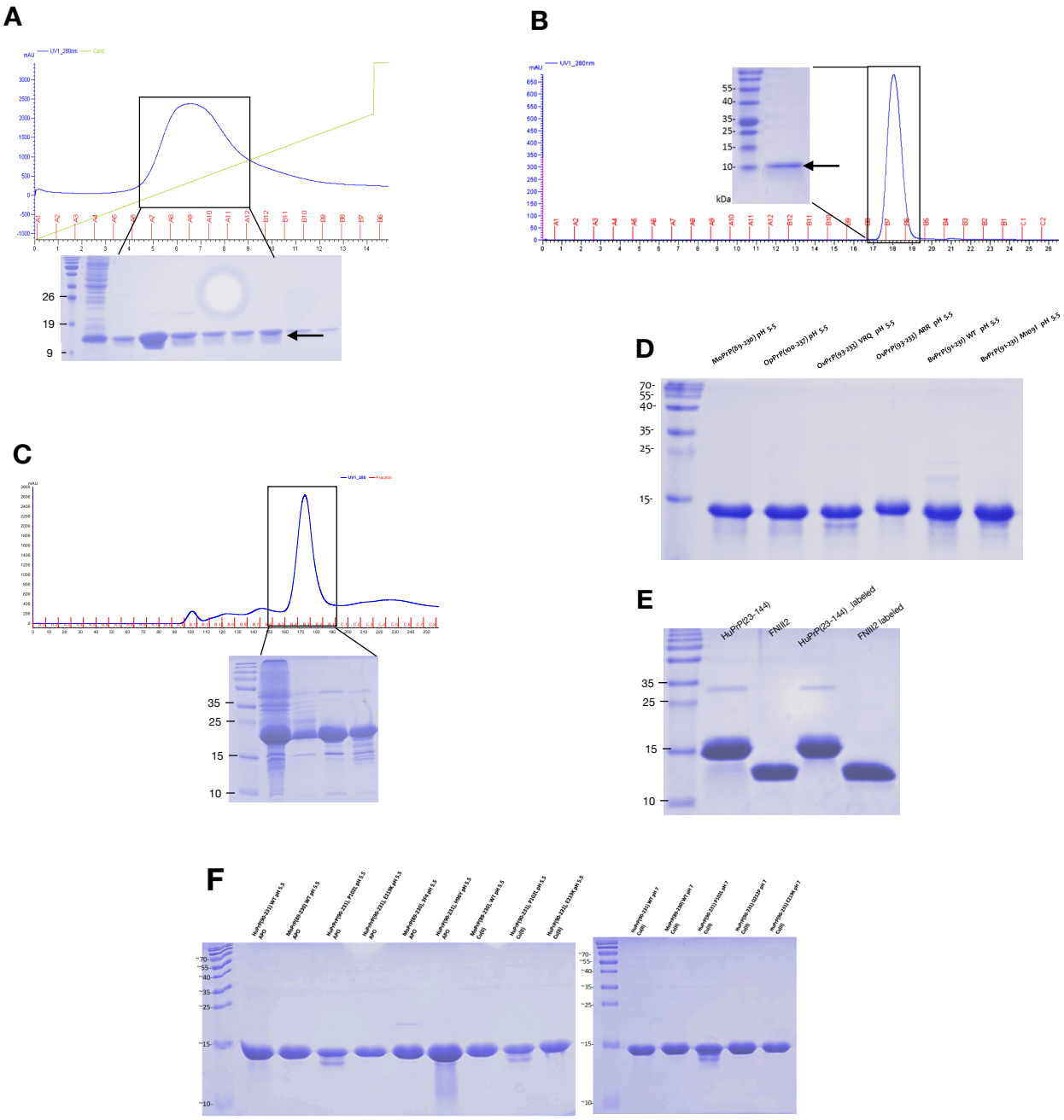

Figure 3. Protein purifications. (A) *Above*, Chromatographic plot of the purification of FNIII2 C-ter_HisTag by HisTrap column, and *below* the corresponding SDS-PAGE of the elution profile. Arrow indicates FNIII2. **(B)** Analytic gel filtration on FNIII2. The inset corresponds to the SDS-PAGE of FNIII2 corresponding of the monodispersed peak. **(C)** *Above,* Size exclusion chromatography profile, and *below* and SDS-PAGE of HuPrP(23-231, M129). **(D-F)** SDS-PAGE of the purified proteins used for NMR and EXAFS experiments.

EXAFS ANALYSIS

Table S1. Structural parameters derived from the EXAFS analysis. Structural parameters detemined from the fit of the EXAFS data at the Cu K-edge of samples 1 to 14. N is the coordination number, R is the distance between the copper ion and the ligand, **?**^{2} is the Debye-Waller factor. Statistical errors are reported in parentheses. Codes 1 to 14 correspond to the following samples: Cu(II) WT HuPrP(90-231) pH5.5 (1), Cu(II) WT HuPrP(90-231) pH 7.0 (2), Cu(II) HuPrP(90-231, Q212P) pH 5.5 (3), Cu(II) HuPrP(90-231, Q212P) pH 7.0 (4), Cu(II) HuPrP(90-231, P102L) pH 5.5 (5), Cu(II) HuPrP(90-231, P102L) pH 7.0 (6), Cu(II) HuPrP(90-231, H96Y) pH 5.5 (7), Cu(II) HuPrP(90-231, H96Y) pH 7.0 (8), Cu(I) WT HuPrP(90-231) pH 5.5 (9), Cu(I) WT HuPrP(90-231) pH 7.0 (10), Cu(I) HuPrP(90-231, Q212P) pH 5.5 (11), Cu(I) HuPrP(90-231, Q212P) pH 7.0 (12), Cu(I) HuPrP(90-231, P102L) pH 5.5 (13), Cu(I) HuPrP(90-231, P102L) pH 7.0 (14).

Cu(II) WT pH=5.5 **(1)**			Cu(II) WT pH=7.0 **(2)**			Cu(II) Q212P pH=5.5 **(3)**			Cu(II) Q212P pH=7.0 **(4)**		
N	**R (Å)**	**σ^2 (Å^2)**	**N**	**R (Å)**	**σ^2 (Å^2)**	**N**	**R (Å)**	**σ^2 (Å^2)**	**N**	**R (Å)**	**σ^2 (Å^2)**
2 N_{His}	1.98(2)	0.006(3)	1 N_{His}	1.99(2)	0.006(3)	1 N_{His}	2.00(2)	0.007(3)	1 N_{His}	1.99(2)	0.007(3)
2 O/N	1.98(2)	0.008(3)	3 O/N	1.99(4)	0.009(3)	3 O/N	1.99(2)	0.009(3)	3 O/N	1.99(3)	0.009(3)
1 O	2.31(3)	0.013(4)	1 O	2.38(4)	0.012(4)	1 O	2.40(4)	0.013(4)	1 O	2.39(3)	0.012(4)
1 S	3.25(4)	0.013(4)	1 S	3.37(4)	0.013(4)	1 S	3.47(4)	0.014(4)	1 S	3.45(4)	0.012(4)
Cu(II) P102L pH=5.5 **(5)**			Cu(II) P102L pH=7.0 **(6)**			Cu(II) H96Y pH=5.5 **(7)**			Cu(II) H96Y pH=7.0 **(8)**		
N	**R (Å)**	**σ^2 (Å^2)**	**N**	**R (Å)**	**σ^2 (Å^2)**	**N**	**R (Å)**	**σ^2 (Å^2)**	**N**	**R (Å)**	**σ^2 (Å^2)**
1 N_{His}	2.00(3)	0.006(3)	1 N_{His}	1.99(2)	0.006(3)	1 N_{His}	2.00(2)	0.007(3)	1 N_{His}	2.00(2)	0.008(3)
O/N	1.99(3)	0.008(3)	3 O/N	1.99(3)	0.009(3)	3 O/N	1.99(2)	0.009(3)	3 O/N	1.99(2)	0.008(3)
1 O	2.34(4)	0.013(4)	1 O	2.38(3)	0.012(4)	1 O	2.40(3)	0.013(4)	1 O	2.39(3)	0.012(4)
1 S	3.32(4)	0.013(4)	1 S	3.38(4)	0.013(4)	1 S	3.47(4)	0.014(4)	1 S	3.45(4)	0.013(4)
Cu(I) WT pH=5.5 **(9)**			Cu(I) WT pH=7.0 **(10)**			Cu(I) Q212P pH=5.5 **(11)**			Cu(I) Q212P pH=7.0 **(12)**		
N	**R (Å)**	**σ^2 (Å^2)**	**N**	**R (Å)**	**σ^2 (Å^2)**	**N**	**R (Å)**	**σ^2 (Å^2)**	**N**	**R (Å)**	**σ^2 (Å^2)**
2 N_{His}	1.98(2)	0.006(3)	1 N_{His}	1.98(2)	0.007(3)	1 N_{His}	1.99(2)	0.007(3)	1 N_{His}	1.99(2)	0.007(3)
2 O/N	1.99(3)	0.009(3)	1 O/N	2.00(2)	0.009(3)	1 O/N	1.99(2)	0.009(3)	3 O/N	1.99(3)	0.009(3)
1 O	2.32(4)	0.014(4)	1 S	2.27(4)	0.009(4)	1 S	2.28(4)	0.008(3)	1 S	2.27(3)	0.009(4)
1 S	3.26(5)	0.013(4)									
Cu(I) P102L pH=5.5 **(13)**			Cu(I) P102L pH=7.0 **(14)**								
N	**R (Å)**	**σ^2 (Å^2)**	**N**	**R (Å)**	**σ^2 (Å^2)**						
1 N_{His}	2.00(2)	0.009(3)	1 N_{His}	1.99(2)	0.008(3)						
1 O/N	1.99(2)	0.009(3)	3 O/N	1.99(3)	0.009(3)						
1 S	2.28(4)	0.009(3)	1 O	2.29(3)	0.010(4)						

Table S2. Structural parameters derived from the EXAFS analysis. Structural parameters determined from the fit of the EXAFS data at the Cu K-edge of Cu(II) HuPrP, Cu(II) OvPrP ARR, Cu(II) OpPrP, Cu(II) HuPrP Q212P, Cu(II) OvPrP VRQ, Cu(II) BvPrP. N is the coordination number, R is the distance between the copper ion and the ligand, σ^2 is the Debye-Waller factor. Statistical errors are reported in parentheses.

OvPrP ARR			**OpPrP**		
N	*R (Å)*	σ^2 *(Å^2)*	*N*	*R (Å)*	σ^2 *(Å^2)*
1 N_{His}	1.98(2)	0.008(3)	1 N_{His}	1.98(2)	0.008(3)
3 O/N	2.00(2)	0.006(3)	3 O/N	2.00(2)	0.009(3)
1 O	2.32(5)	0.015(4)	1 O	2.28(5)	0.014(4)
1 S	3.27(4)	0.009(4)	1 S	3.23(4)	0.009(4)
2 C	2.86(4)	0.007(4)	2 C	2.87(4)	0.006(4)
OvPrP VRQ			**BvPrP**		
N	*R (Å)*	σ^2 *(Å^2)*	*N*	*R (Å)*	σ^2 *(Å^2)*
1 N_{His}	2.00(2)	0.008(3)	1 N_{His}	2.00(2)	0.008(3)
3 O/N	1.99(3)	0.009(3)	3 O/N	1.99(2)	0.009(3)
1 O	2.41(3)	0.010(4)	1 O	2.41(3)	0.009(4)
1 S	3.26(4)	0.015(4)	1 S	3.26(4)	0.013(4)

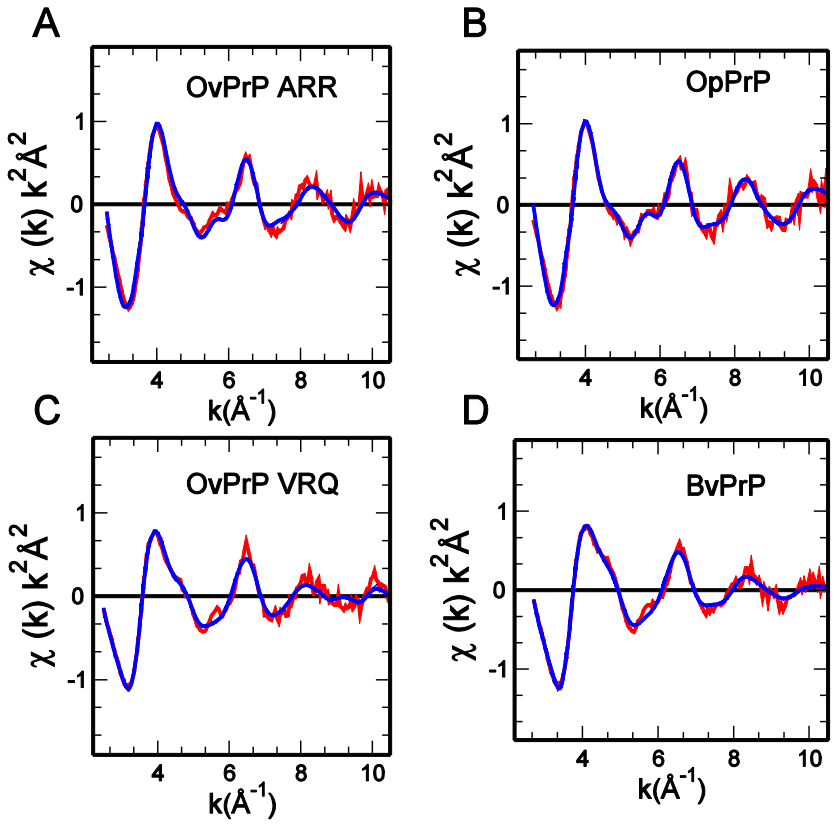

Figure S1. Comparison between the Cu K-edge EXAFS spectra (red lines) of Cu(II) OvPrP ARR (**A**), Cu(II) OpPrP (**B**), Cu(II) OvPrP VRQ (**C**), and Cu(II) BvPrP (**D**) and theoretical curves (blue lines) calculated with the type-1 and type-2 copper coordination models.

APPENDIX II

SUPPLEMENTARY MATERIALS AND METHODS

1. STED nanoscopy experiments

Note: STED microscopy was performed at the NanoBiophotonics Department (Max Plank Institute for Biophysical Chemistry, Göttingen, Germany) and analyzed by Dr. Ladan Amin. For this reason, the related Materials and Methods are presented in this separate section.

Cell culture. P1-P2 FVB wt mice were sacrificed by decapitation in accordance with the guidelines of the Italian Animal Welfare Act.

Immunostaining. Cells were fixed in 4% paraformaldehyde containing 0.15% picric acid in phosphate-buffered saline (PBS), saturated with 0.1 M glycine, permeabilized with 0.1% Triton X-100, saturated with 0.5% BSA (all from Sigma-Aldrich, St. Louis, MO) in PBS and then incubated for 1 h with primary antibodies followed by the 30 min incubation with secondary antibodies conjugated with STAR580 or STAR635P (Abberior, Göttingen, Germany). All incubations were performed at room temperature (20-22 °C).

STED microscopy. 2-color STED microscopy was performed at the NanoBiophotonics Department (Max Plank Institute for Biophysical Chemistry, Göttingen, Germany) equipped with 561 nm and 640 nm pulsed excitation lasers, a pulsed 775 nm STED laser, and a 100x oil immersion objective lens (NA 1.4).

2. Molecular Dynamics simulation on HuPrP WT

Note: The simulation-based structural predictions were performed by Giordano Mancini (Scuola Normale Superiore, Pisa, Italy). For this reason, the related Materials and Methods are presented in this separate section.

Two simulations of WT HuPrP(90-231) in complex with Cu(II) were performed in order to resemble experimental conditions either at pH 5.5 or pH 7.0. Based on experimental results, in the simulation resembling pH 5.5 (hereafter termed 2His) both H96 and H111 were bound to Cu(II), while at pH 7.0 (hereafter termed 1His) only H111 was bound to the metal. Starting coordinates of HuPrP(90-231) were obtained from the 1QM1 PDB structure [25]. Missing hydrogen atoms were added by MolProbity [254] and protonation states counter-checked with

H^{++} code [255]. To model the binding of Cu(II) in the active site a set of harmonic springs was used to enforce copper-ligand distances [256]. Bond lengths of the springs were based on EXAFS data and set to 1.98 Å for the N_δ imidazole atoms in H96 and H111, to 1.98 Å for the amide oxygen in Q98 and to 3.25 Å for the S atom in M109. The systems were modeled using the AMBER99SB-ILDN* all-atom force field[257] implemented in the GROMACS MD package version 4.6.5 [258]. The protein was immersed in a rhombic dodecahedron box with a minimum distance of 2.5 nm from the box edges; a long distance from the box edges was used to take into proper account the flexibility of HuPrP(90-231). The resulting system was composed of 2192 protein atoms, 54873 TIP3P [259] water molecules, 1 Cl^- ion for a total of 166812 atoms. Electrostatic interactions were accounted by means of the Particle Mesh Ewald method (PME) using a cutoff of 1.5 nm for the real space and Van der Waals interactions [260]. The LINCS algorithm was used to constrain bond lengths and angles[261], with the exception of Cu(II)-protein bonds. Relaxation of solvent molecules and Cl^- ion was initially performed keeping solute atoms restrained to their initial positions with a force constant of 1000 kJ/(mol • nm^2), for 3.0 ns in a NPT ensemble and using an integration time step of 1.0 fs. Then, the system was simulated for 5 ns while using a force constant of 1000 kJ/(mol • nm^2) for bonds involving Cu(II) to force the active site residues in the desired position. At this point H111 was freed to create the 1His system and after this step two separate simulations were carried out. The two systems were carried again to 0 K, the force constants in the active site changed to 100 kJ/(mol • nm^2) and then heated again to 298.15 K. The two systems were then simulated for 150 ns in a NVT ensemble with a time step of 2.0 fs and the neighbor list was updated every 10 steps. Temperature was kept constant using the velocity rescale method with a coupling constant of 0.1 ps during sampling [262]. Structures were clustered using backbone atoms and the GROMOS method [263]. A total of 15000 frames from each simulation were selected with constant pace of 10 ps and a Root Mean Square Deviation (RMSD) threshold of 0.30 nm; only the positions of Cα carbon atoms were used for clustering. Two residues were considered to be bound by a hydrogen (H) bond in a given frame if the H-acceptor distance was below 0.375 nm and the acceptor – donor– H angle was below 40.0°. Two residues are connected by a salt bridge if the nitrogen-oxygen distance is below 0.4 nm in a given frame. All analyses were carried out with standard tools present in the GROMACS MD package v. 4.6.5 or with in-house written codes, except for secondary structure assignment which was performed with DSSP [264]. Figures were produced with Chimera 1.10 software.

References:

1. Basler, K., et al., *Scrapie and cellular PrP isoforms are encoded by the same chromosomal gene.* Cell, 1986. **46**(3): p. 417-28.
2. Hsiao, K., et al., *Linkage of a prion protein missense variant to Gerstmann-Straussler syndrome.* Nature, 1989. **338**(6213): p. 342-5.
3. Prusiner, S.B., et al., *Prion protein biology.* Cell, 1998. **93**(3): p. 337-48.
4. Lee, I.Y., et al., *Complete genomic sequence and analysis of the prion protein gene region from three mammalian species.* Genome Res, 1998. **8**(10): p. 1022-37.
5. Premzl, M., et al., *The prion protein gene: identifying regulatory signals using marsupial sequence.* Gene, 2005. **349**: p. 121-34.
6. McKinley, M.P., et al., *Developmental expression of prion protein gene in brain.* Dev Biol, 1987. **121**(1): p. 105-10.
7. Lieberburg, I., *Developmental expression and regional distribution of the scrapie-associated protein mRNA in the rat central nervous system.* Brain Res, 1987. **417**(2): p. 363-6.
8. Kretzschmar, H.A., et al., *Scrapie prion proteins are synthesized in neurons.* Am J Pathol, 1986. **122**(1): p. 1-5.
9. Rapoport, T.A., *Protein translocation across the eukaryotic endoplasmic reticulum and bacterial plasma membranes.* Nature, 2007. **450**(7170): p. 663-9.
10. Hebert, D.N. and M. Molinari, *In and out of the ER: protein folding, quality control, degradation, and related human diseases.* Physiol Rev, 2007. **87**(4): p. 1377-408.
11. Stahl, N., et al., *Scrapie prion protein contains a phosphatidylinositol glycolipid.* Cell, 1987. **51**(2): p. 229-40.
12. Hegde, R.S., et al., *A transmembrane form of the prion protein in neurodegenerative disease.* Science, 1998. **279**(5352): p. 827-34.
13. Stewart, R.S., B. Drisaldi, and D.A. Harris, *A transmembrane form of the prion protein contains an uncleaved signal peptide and is retained in the endoplasmic Reticulum.* Mol Biol Cell, 2001. **12**(4): p. 881-9.
14. Stahl, N., et al., *Glycosylinositol phospholipid anchors of the scrapie and cellular prion proteins contain sialic acid.* Biochemistry, 1992. **31**(21): p. 5043-53.
15. Abid, K., R. Morales, and C. Soto, *Cellular factors implicated in prion replication.* FEBS Lett, 2010. **584**(11): p. 2409-14.
16. Sarnataro, D., et al., *PrP(C) association with lipid rafts in the early secretory pathway stabilizes its cellular conformation.* Mol Biol Cell, 2004. **15**(9): p. 4031-42.
17. Taylor, D.R., et al., *Assigning functions to distinct regions of the N-terminus of the prion protein that are involved in its copper-stimulated, clathrin-dependent endocytosis.* J Cell Sci, 2005. **118**(Pt 21): p. 5141-53.
18. Taylor, D.R. and N.M. Hooper, *The prion protein and lipid rafts.* Mol Membr Biol, 2006. **23**(1): p. 89-99.
19. Aguzzi, A. and A.M. Calella, *Prions: protein aggregation and infectious diseases.* Physiol Rev, 2009. **89**(4): p. 1105-52.
20. Shyng, S.L., M.T. Huber, and D.A. Harris, *A prion protein cycles between the cell surface and an endocytic compartment in cultured neuroblastoma cells.* J Biol Chem, 1993. **268**(21): p. 15922-8.
21. Harris, D.A., *Cellular biology of prion diseases.* Clin Microbiol Rev, 1999. **12**(3): p. 429-44.
22. Sunyach, C., et al., *The mechanism of internalization of glycosylphosphatidylinositol-anchored prion protein.* EMBO J, 2003. **22**(14): p. 3591-601.
23. Hornemann, S., C. Schorn, and K. Wuthrich, *NMR structure of the bovine prion protein isolated from healthy calf brains.* EMBO Rep, 2004. **5**(12): p. 1159-64.

24. Legname, G., Giachin, G. & Benetti, F., *Structural Studies of Prion Proteins and Prions. In: Non-fibrillar Amyloidogenic Protein Assemblies - Common Cytotoxins Underlying Degenerative Diseases (eds Rahimi, F. & Bitan, G.)*. 2012: Springer Netherlands.
25. Zahn, R., et al., *NMR solution structure of the human prion protein.* Proc Natl Acad Sci U S A, 2000. **97**(1): p. 145-50.
26. Surewicz, W.K. and M.I. Apostol, *Prion protein and its conformational conversion: a structural perspective.* Top Curr Chem, 2011. **305**: p. 135-67.
27. Pan, T., et al., *Cell-surface prion protein interacts with glycosaminoglycans.* Biochem J, 2002. **368**(Pt 1): p. 81-90.
28. Yin, S., et al., *Human prion proteins with pathogenic mutations share common conformational changes resulting in enhanced binding to glycosaminoglycans.* Proc Natl Acad Sci U S A, 2007. **104**(18): p. 7546-51.
29. Takemura, K., et al., *DNA aptamers that bind to PrP(C) and not PrP(Sc) show sequence and structure specificity.* Exp Biol Med (Maywood), 2006. **231**(2): p. 204-14.
30. Mashima, T., et al., *Unique quadruplex structure and interaction of an RNA aptamer against bovine prion protein.* Nucleic Acids Res, 2009. **37**(18): p. 6249-58.
31. Taylor, D.R. and N.M. Hooper, *The low-density lipoprotein receptor-related protein 1 (LRP1) mediates the endocytosis of the cellular prion protein.* Biochem J, 2007. **402**(1): p. 17-23.
32. Muramoto, T., et al., *Recombinant scrapie-like prion protein of 106 amino acids is soluble.* Proc Natl Acad Sci U S A, 1996. **93**(26): p. 15457-62.
33. Muramoto, T., et al., *Heritable disorder resembling neuronal storage disease in mice expressing prion protein with deletion of an alpha-helix.* Nat Med, 1997. **3**(7): p. 750-5.
34. Aguzzi, A., F. Baumann, and J. Bremer, *The prion's elusive reason for being.* Annu Rev Neurosci, 2008. **31**: p. 439-77.
35. Brown, D.R., J. Herms, and H.A. Kretzschmar, *Mouse cortical cells lacking cellular PrP survive in culture with a neurotoxic PrP fragment.* Neuroreport, 1994. **5**(16): p. 2057-60.
36. Forloni, G., et al., *Neurotoxicity of a prion protein fragment.* Nature, 1993. **362**(6420): p. 543-6.
37. Gasset, M., et al., *Perturbation of the secondary structure of the scrapie prion protein under conditions that alter infectivity.* Proc Natl Acad Sci U S A, 1993. **90**(1): p. 1-5.
38. Peretz, D., et al., *A conformational transition at the N terminus of the prion protein features in formation of the scrapie isoform.* J Mol Biol, 1997. **273**(3): p. 614-22.
39. White, A.R., et al., *Monoclonal antibodies inhibit prion replication and delay the development of prion disease.* Nature, 2003. **422**(6927): p. 80-3.
40. Abskharon, R.N., et al., *Probing the N-terminal beta-sheet conversion in the crystal structure of the human prion protein bound to a nanobody.* J Am Chem Soc, 2014. **136**(3): p. 937-44.
41. Legname, G., *Elucidating the function of the prion protein.* PLoS Pathog, 2017. **13**(8): p. e1006458.
42. Biljan, I., et al., *Structural basis for the protective effect of the human prion protein carrying the dominant-negative E219K polymorphism.* Biochem J, 2012. **446**(2): p. 243-51.
43. Calzolai, L. and R. Zahn, *Influence of pH on NMR structure and stability of the human prion protein globular domain.* J Biol Chem, 2003. **278**(37): p. 35592-6.
44. Wood, J.L., L.J. Lund, and S.H. Done, *The natural occurrence of scrapie in moufflon.* Vet Rec, 1992. **130**(2): p. 25-7.
45. Wells, G.A., et al., *A novel progressive spongiform encephalopathy in cattle.* Vet Rec, 1987. **121**(18): p. 419-20.
46. Barlow, R.M., *Transmissible mink encephalopathy: pathogenesis and nature of the aetiological agent.* J Clin Pathol Suppl (R Coll Pathol), 1972. **6**: p. 102-9.

47. Wyatt, J.M., et al., *Naturally occurring scrapie-like spongiform encephalopathy in five domestic cats.* Vet Rec, 1991. **129**(11): p. 233-6.
48. Williams, E.S. and S. Young, *Spongiform encephalopathy of Rocky Mountain elk.* J Wildl Dis, 1982. **18**(4): p. 465-71.
49. Jeffrey, M. and L. Gonzalez, *Classical sheep transmissible spongiform encephalopathies: pathogenesis, pathological phenotypes and clinical disease.* Neuropathol Appl Neurobiol, 2007. **33**(4): p. 373-94.
50. Jacobs, J.G., et al., *Molecular discrimination of atypical bovine spongiform encephalopathy strains from a geographical region spanning a wide area in Europe.* J Clin Microbiol, 2007. **45**(6): p. 1821-9.
51. Yamakawa, H., et al., *Serum KL-6 and surfactant protein-D as monitoring and predictive markers of interstitial lung disease in patients with systemic sclerosis and mixed connective tissue disease.* J Thorac Dis, 2017. **9**(2): p. 362-371.
52. Masujin, K., et al., *Biological and biochemical characterization of L-type-like bovine spongiform encephalopathy (BSE) detected in Japanese black beef cattle.* Prion, 2008. **2**(3): p. 123-8.
53. Richt, J.A., et al., *Identification and characterization of two bovine spongiform encephalopathy cases diagnosed in the United States.* J Vet Diagn Invest, 2007. **19**(2): p. 142-54.
54. Dudas, S., et al., *Molecular, biochemical and genetic characteristics of BSE in Canada.* PLoS One, 2010. **5**(5): p. e10638.
55. Casalone, C., et al., *Identification of a second bovine amyloidotic spongiform encephalopathy: molecular similarities with sporadic Creutzfeldt-Jakob disease.* Proc Natl Acad Sci U S A, 2004. **101**(9): p. 3065-70.
56. Biacabe, A.G., et al., *Distinct molecular phenotypes in bovine prion diseases.* EMBO Rep, 2004. **5**(1): p. 110-5.
57. Comoy, E.E., et al., *Atypical BSE (BASE) transmitted from asymptomatic aging cattle to a primate.* PLoS One, 2008. **3**(8): p. e3017.
58. Wilson, R., et al., *Presence of subclinical infection in gene-targeted human prion protein transgenic mice exposed to atypical bovine spongiform encephalopathy.* J Gen Virol, 2013. **94**(Pt 12): p. 2819-27.
59. Williams, E.S. and S. Young, *Chronic wasting disease of captive mule deer: a spongiform encephalopathy.* J Wildl Dis, 1980. **16**(1): p. 89-98.
60. Tamguney, G., et al., *Transmission of elk and deer prions to transgenic mice.* J Virol, 2006. **80**(18): p. 9104-14.
61. Pan, K.M., et al., *Conversion of alpha-helices into beta-sheets features in the formation of the scrapie prion proteins.* Proc Natl Acad Sci U S A, 1993. **90**(23): p. 10962-6.
62. Sigurdson, C.J. and M.W. Miller, *Other animal prion diseases.* Br Med Bull, 2003. **66**: p. 199-212.
63. Sigurdson, C.J., *A prion disease of cervids: chronic wasting disease.* Vet Res, 2008. **39**(4): p. 41.
64. Mathiason, C.K., et al., *Infectious prions in pre-clinical deer and transmission of chronic wasting disease solely by environmental exposure.* PLoS One, 2009. **4**(6): p. e5916.
65. Seelig, D.M., et al., *Pathogenesis of chronic wasting disease in cervidized transgenic mice.* Am J Pathol, 2010. **176**(6): p. 2785-97.
66. Gibbs, C.J., Jr., et al., *Creutzfeldt-Jakob disease (spongiform encephalopathy): transmission to the chimpanzee.* Science, 1968. **161**(3839): p. 388-9.
67. Masters, C.L., D.C. Gajdusek, and C.J. Gibbs, Jr., *Creutzfeldt-Jakob disease virus isolations from the Gerstmann-Straussler syndrome with an analysis of the various forms of amyloid plaque deposition in the virus-induced spongiform encephalopathies.* Brain, 1981. **104**(3): p. 559-88.

68. Medori, R., et al., *Fatal familial insomnia, a prion disease with a mutation at codon 178 of the prion protein gene.* N Engl J Med, 1992. **326**(7): p. 444-9.
69. Gajdusek, D.C., C.J. Gibbs, and M. Alpers, *Experimental transmission of a Kuru-like syndrome to chimpanzees.* Nature, 1966. **209**(5025): p. 794-6.
70. Ladogana, A., et al., *Mortality from Creutzfeldt-Jakob disease and related disorders in Europe, Australia, and Canada.* Neurology, 2005. **64**(9): p. 1586-91.
71. Mead, S., *Prion disease genetics.* Eur J Hum Genet, 2006. **14**(3): p. 273-81.
72. Giachin, G., et al., *Probing early misfolding events in prion protein mutants by NMR spectroscopy.* Molecules, 2013. **18**(8): p. 9451-76.
73. Apetri, A.C., K. Surewicz, and W.K. Surewicz, *The effect of disease-associated mutations on the folding pathway of human prion protein.* J Biol Chem, 2004. **279**(17): p. 18008-14.
74. Kramer, M.L., et al., *Prion protein binds copper within the physiological concentration range.* J Biol Chem, 2001. **276**(20): p. 16711-9.
75. Swietnicki, W., et al., *Familial mutations and the thermodynamic stability of the recombinant human prion protein.* J Biol Chem, 1998. **273**(47): p. 31048-52.
76. Kaneko, K., et al., *Evidence for protein X binding to a discontinuous epitope on the cellular prion protein during scrapie prion propagation.* Proc Natl Acad Sci U S A, 1997. **94**(19): p. 10069-74.
77. Telling, G.C., et al., *Prion propagation in mice expressing human and chimeric PrP transgenes implicates the interaction of cellular PrP with another protein.* Cell, 1995. **83**(1): p. 79-90.
78. Ashok, A. and R.S. Hegde, *Selective processing and metabolism of disease-causing mutant prion proteins.* PLoS Pathog, 2009. **5**(6): p. e1000479.
79. Prusiner, S.B., *Novel proteinaceous infectious particles cause scrapie.* Science, 1982. **216**(4542): p. 136-44.
80. Jarrett, J.T. and P.T. Lansbury, Jr., *Seeding "one-dimensional crystallization" of amyloid: a pathogenic mechanism in Alzheimer's disease and scrapie?* Cell, 1993. **73**(6): p. 1055-8.
81. Prusiner, S.B., *Molecular biology of prion diseases.* Science, 1991. **252**(5012): p. 1515-22.
82. Colby, D.W. and S.B. Prusiner, *Prions.* Cold Spring Harb Perspect Biol, 2011. **3**(1): p. a006833.
83. Prusiner, S.B., et al., *Scrapie prions aggregate to form amyloid-like birefringent rods.* Cell, 1983. **35**(2 Pt 1): p. 349-58.
84. Wille, H., S.B. Prusiner, and F.E. Cohen, *Scrapie infectivity is independent of amyloid staining properties of the N-terminally truncated prion protein.* J Struct Biol, 2000. **130**(2-3): p. 323-38.
85. Gambetti, P., et al., *A novel human disease with abnormal prion protein sensitive to protease.* Ann Neurol, 2008. **63**(6): p. 697-708.
86. Vazquez-Fernandez, E., et al., *Structural organization of mammalian prions as probed by limited proteolysis.* PLoS One, 2012. **7**(11): p. e50111.
87. Govaerts, C., et al., *Evidence for assembly of prions with left-handed beta-helices into trimers.* Proc Natl Acad Sci U S A, 2004. **101**(22): p. 8342-7.
88. Junker, M., et al., *Pertactin beta-helix folding mechanism suggests common themes for the secretion and folding of autotransporter proteins.* Proc Natl Acad Sci U S A, 2006. **103**(13): p. 4918-23.
89. Wasmer, C., et al., *Amyloid fibrils of the HET-s(218-289) prion form a beta solenoid with a triangular hydrophobic core.* Science, 2008. **319**(5869): p. 1523-6.
90. Smirnovas, V., et al., *Structural organization of brain-derived mammalian prions examined by hydrogen-deuterium exchange.* Nat Struct Mol Biol, 2011. **18**(4): p. 504-6.

91. Kraus, A., B.R. Groveman, and B. Caughey, *Prions and the potential transmissibility of protein misfolding diseases.* Annu Rev Microbiol, 2013. **67**: p. 543-64.
92. Requena, J.R. and H. Wille, *The structure of the infectious prion protein: experimental data and molecular models.* Prion, 2014. **8**(1): p. 60-6.
93. Wille, H., et al., *Natural and synthetic prion structure from X-ray fiber diffraction.* Proc Natl Acad Sci U S A, 2009. **106**(40): p. 16990-5.
94. Terry, C., et al., *Ex vivo mammalian prions are formed of paired double helical prion protein fibrils.* Open Biol, 2016. **6**(5).
95. Vazquez-Fernandez, E., et al., *The Structural Architecture of an Infectious Mammalian Prion Using Electron Cryomicroscopy.* PLoS Pathog, 2016. **12**(9): p. e1005835.
96. Wan, W., et al., *Structural studies of truncated forms of the prion protein PrP.* Biophys J, 2015. **108**(6): p. 1548-54.
97. Race, R., et al., *Subclinical scrapie infection in a resistant species: persistence, replication, and adaptation of infectivity during four passages.* J Infect Dis, 2002. **186 Suppl 2**: p. S166-70.
98. Gibbs, C.J., Jr. and D.C. Gajdusek, *Experimental subacute spongiform virus encephalopathies in primates and other laboratory animals.* Science, 1973. **182**(4107): p. 67-8.
99. Nonno, R., et al., *Efficient transmission and characterization of Creutzfeldt-Jakob disease strains in bank voles.* PLoS Pathog, 2006. **2**(2): p. e12.
100. Aguzzi, A., M. Heikenwalder, and M. Polymenidou, *Insights into prion strains and neurotoxicity.* Nat Rev Mol Cell Biol, 2007. **8**(7): p. 552-61.
101. Bartz, J.C., et al., *Adaptation and selection of prion protein strain conformations following interspecies transmission of transmissible mink encephalopathy.* J Virol, 2000. **74**(12): p. 5542-7.
102. Peretz, D., et al., *Strain-specified relative conformational stability of the scrapie prion protein.* Protein Sci, 2001. **10**(4): p. 854-63.
103. Bessen, R.A. and R.F. Marsh, *Identification of two biologically distinct strains of transmissible mink encephalopathy in hamsters.* J Gen Virol, 1992. **73 (Pt 2)**: p. 329-34.
104. Collinge, J., et al., *Transmission of fatal familial insomnia to laboratory animals.* Lancet, 1995. **346**(8974): p. 569-70.
105. Parchi, P., et al., *Molecular basis of phenotypic variability in sporadic Creutzfeldt-Jakob disease.* Ann Neurol, 1996. **39**(6): p. 767-78.
106. Safar, J. and S.B. Prusiner, *Molecular studies of prion diseases.* Prog Brain Res, 1998. **117**: p. 421-34.
107. Bruce, M.E., *Scrapie strain variation and mutation.* Br Med Bull, 1993. **49**(4): p. 822-38.
108. Kurt, T.D., et al., *Prion transmission prevented by modifying the beta2-alpha2 loop structure of host PrPC.* J Neurosci, 2014. **34**(3): p. 1022-7.
109. Christen, B., et al., *Structural plasticity of the cellular prion protein and implications in health and disease.* Proc Natl Acad Sci U S A, 2013. **110**(21): p. 8549-54.
110. Kurt, T.D., et al., *A proposed mechanism for the promotion of prion conversion involving a strictly conserved tyrosine residue in the beta2-alpha2 loop of PrPC.* J Biol Chem, 2014. **289**(15): p. 10660-7.
111. Dutta, A., S. Chen, and W.K. Surewicz, *The effect of beta2-alpha2 loop mutation on amyloidogenic properties of the prion protein.* FEBS Lett, 2013. **587**(18): p. 2918-23.
112. Sigurdson, C.J., et al., *Spongiform encephalopathy in transgenic mice expressing a point mutation in the beta2-alpha2 loop of the prion protein.* J Neurosci, 2011. **31**(39): p. 13840-7.
113. Donne, D.G., et al., *Structure of the recombinant full-length hamster prion protein PrP(29-231): the N terminus is highly flexible.* Proc Natl Acad Sci U S A, 1997. **94**(25): p. 13452-7.

114. Gossert, A.D., et al., *Prion protein NMR structures of elk and of mouse/elk hybrids.* Proc Natl Acad Sci U S A, 2005. **102**(3): p. 646-50.
115. Christen, B., et al., *NMR structure of the bank vole prion protein at 20 degrees C contains a structured loop of residues 165-171.* J Mol Biol, 2008. **383**(2): p. 306-12.
116. Christen, B., et al., *Prion protein NMR structure from tammar wallaby (Macropus eugenii) shows that the beta2-alpha2 loop is modulated by long-range sequence effects.* J Mol Biol, 2009. **389**(5): p. 833-45.
117. Wen, Y., et al., *Unique structural characteristics of the rabbit prion protein.* J Biol Chem, 2010. **285**(41): p. 31682-93.
118. Perez, D.R., F.F. Damberger, and K. Wuthrich, *Horse prion protein NMR structure and comparisons with related variants of the mouse prion protein.* J Mol Biol, 2010. **400**(2): p. 121-8.
119. Riek, R., et al., *NMR structure of the mouse prion protein domain PrP(121-231).* Nature, 1996. **382**(6587): p. 180-2.
120. Sigurdson, C.J., et al., *De novo generation of a transmissible spongiform encephalopathy by mouse transgenesis.* Proc Natl Acad Sci U S A, 2009. **106**(1): p. 304-9.
121. Lysek, D.A., et al., *Prion protein NMR structures of cats, dogs, pigs, and sheep.* Proc Natl Acad Sci U S A, 2005. **102**(3): p. 640-5.
122. Sigurdson, C.J., et al., *A molecular switch controls interspecies prion disease transmission in mice.* J Clin Invest, 2010. **120**(7): p. 2590-9.
123. Sweeting, B., et al., *Structural factors underlying the species barrier and susceptibility to infection in prion disease.* Biochem Cell Biol, 2010. **88**(2): p. 195-202.
124. Goldmann, W., et al., *PrP genotype and agent effects in scrapie: change in allelic interaction with different isolates of agent in sheep, a natural host of scrapie.* J Gen Virol, 1994. **75 (Pt 5)**: p. 989-95.
125. Imran, M. and S. Mahmood, *An overview of human prion diseases.* Virol J, 2011. **8**: p. 559.
126. Groschup, M.H., et al., *Classic scrapie in sheep with the ARR/ARR prion genotype in Germany and France.* Emerg Infect Dis, 2007. **13**(8): p. 1201-7.
127. Rezaei, H., et al., *Amyloidogenic unfolding intermediates differentiate sheep prion protein variants.* J Mol Biol, 2002. **322**(4): p. 799-814.
128. Haire, L.F., et al., *The crystal structure of the globular domain of sheep prion protein.* J Mol Biol, 2004. **336**(5): p. 1175-83.
129. Collinge, J., et al., *Prion protein gene analysis in new variant cases of Creutzfeldt-Jakob disease.* Lancet, 1996. **348**(9019): p. 56.
130. Concepcion, G.P. and E.A. Padlan, *The codon for the methionine at position 129 (M129) in the human prion protein provides an alternative initiation site for translation and renders individuals homozygous for M129 more susceptible to prion disease.* Med Hypotheses, 2005. **65**(5): p. 865-7.
131. Apetri, A.C., D.L. Vanik, and W.K. Surewicz, *Polymorphism at residue 129 modulates the conformational conversion of the D178N variant of human prion protein 90-231.* Biochemistry, 2005. **44**(48): p. 15880-8.
132. Bueler, H., et al., *Normal development and behaviour of mice lacking the neuronal cell-surface PrP protein.* Nature, 1992. **356**(6370): p. 577-82.
133. Manson, J.C., et al., *129/Ola mice carrying a null mutation in PrP that abolishes mRNA production are developmentally normal.* Mol Neurobiol, 1994. **8**(2-3): p. 121-7.
134. Nishida, N., et al., *A mouse prion protein transgene rescues mice deficient for the prion protein gene from purkinje cell degeneration and demyelination.* Lab Invest, 1999. **79**(6): p. 689-97.
135. Sakaguchi, S., et al., *Loss of cerebellar Purkinje cells in aged mice homozygous for a disrupted PrP gene.* Nature, 1996. **380**(6574): p. 528-31.

136. Mironov, A., Jr., et al., *Cytosolic prion protein in neurons.* J Neurosci, 2003. **23**(18): p. 7183-93.
137. Herms, J., et al., *Evidence of presynaptic location and function of the prion protein.* J Neurosci, 1999. **19**(20): p. 8866-75.
138. Siskova, Z., et al., *Brain region specific pre-synaptic and post-synaptic degeneration are early components of neuropathology in prion disease.* PLoS One, 2013. **8**(1): p. e55004.
139. Mastrianni, J.A., et al., *Prion protein conformation in a patient with sporadic fatal insomnia.* N Engl J Med, 1999. **340**(21): p. 1630-8.
140. Gasperini, L., et al., *Prion protein and copper cooperatively protect neurons by modulating NMDA receptor through S-nitrosylation.* Antioxid Redox Signal, 2015. **22**(9): p. 772-84.
141. Lassle, M., et al., *Stress-inducible, murine protein mSTI1. Characterization of binding domains for heat shock proteins and in vitro phosphorylation by different kinases.* J Biol Chem, 1997. **272**(3): p. 1876-84.
142. Chiarini, L.B., et al., *Cellular prion protein transduces neuroprotective signals.* Embo j, 2002. **21**(13): p. 3317-26.
143. Crossin, K.L. and L.A. Krushel, *Cellular signaling by neural cell adhesion molecules of the immunoglobulin superfamily.* Developmental Dynamics: An Official Publication of the American Association of Anatomists, 2000. **218**: p. 260-279.
144. Schachner, M., *Neural recognition molecules and synaptic plasticity.* Current Opinion in Cell Biology, 1997. **9**: p. 627-634.
145. Soroka, V., C. Kasper, and F.M. Poulsen, *Structural Biology of NCAM*, in *Structure and Function of the Neural Cell Adhesion Molecule NCAM*, V. Berezin, Editor. 2010, Springer New York. p. 3-22.
146. Boutin, C., et al., *NCAM expression induces neurogenesis in vivo.* The European Journal of Neuroscience, 2009. **30**: p. 1209-1218.
147. Frei, T., et al., *Different extracellular domains of the neural cell adhesion molecule (N-CAM) are involved in different functions.* The Journal of Cell Biology, 1992. **118**: p. 177-194.
148. Soroka, V., et al., *Structure and interactions of NCAM Ig1-2-3 suggest a novel zipper mechanism for homophilic adhesion.* Structure, 2003. **11**(10): p. 1291-301.
149. Kiselyov, V.V., et al., *Structural biology of NCAM homophilic binding and activation of FGFR.* Journal of Neurochemistry, 2005. **94**: p. 1169-1179.
150. Schmitt-Ulms, G., et al., *Binding of neural cell adhesion molecules (N-CAMs) to the cellular prion protein.* J Mol Biol, 2001. **314**(5): p. 1209-25.
151. Mouillet-Richard, S., et al., *Signal transduction through prion protein.* Science, 2000. **289**(5486): p. 1925-8.
152. Beggs, H.E., P. Soriano, and P.F. Maness, *NCAM-dependent neurite outgrowth is inhibited in neurons from Fyn-minus mice.* J Cell Biol, 1994. **127**(3): p. 825-33.
153. Santuccione, A., et al., *Prion protein recruits its neuronal receptor NCAM to lipid rafts to activate p59fyn and to enhance neurite outgrowth.* The Journal of Cell Biology, 2005. **169**: p. 341-354.
154. Niethammer, P., et al., *Cosignaling of NCAM via lipid rafts and the FGF receptor is required for neuritogenesis.* J Cell Biol, 2002. **157**(3): p. 521-32.
155. Schmitt-Ulms, G., et al., *Binding of neural cell adhesion molecules (N-CAMs) to the cellular prion protein.* Journal of Molecular Biology, 2001. **314**: p. 1209-1225.
156. Klewpatinond, M., et al., *Deconvoluting the Cu2+ binding modes of full-length prion protein.* J Biol Chem, 2008. **283**(4): p. 1870-81.
157. Walter, E.D., et al., *Copper binding extrinsic to the octarepeat region in the prion protein.* Curr Protein Pept Sci, 2009. **10**(5): p. 529-35.
158. Burns, C.S., et al., *Molecular features of the copper binding sites in the octarepeat domain of the prion protein.* Biochemistry, 2002. **41**(12): p. 3991-4001.

159. Prusiner, S.B., et al., *Purification and structural studies of a major scrapie prion protein.* Cell, 1984. **38**(1): p. 127-34.
160. Chiesa, R., et al., *Primary myopathy and accumulation of PrPSc-like molecules in peripheral tissues of transgenic mice expressing a prion protein insertional mutation.* Neurobiol Dis, 2001. **8**(2): p. 279-88.
161. Jones, C.E., et al., *Preferential Cu2+ coordination by His96 and His111 induces beta-sheet formation in the unstructured amyloidogenic region of the prion protein.* J Biol Chem, 2004. **279**(31): p. 32018-27.
162. Quintanar, L., et al., *Copper coordination to the prion protein: Insights from theoretical studies.* Coordination Chemistry Reviews, 2013. **257**(2): p. 429-444.
163. Millhauser, G.L., *Copper and the prion protein: methods, structures, function, and disease.* Annu Rev Phys Chem, 2007. **58**: p. 299-320.
164. D'Angelo, P., et al., *Effects of the pathological Q212P mutation on human prion protein non-octarepeat copper-binding site.* Biochemistry, 2012. **51**(31): p. 6068-79.
165. Hasnain, S.S., et al., *XAFS study of the high-affinity copper-binding site of human PrP(91-231) and its low-resolution structure in solution.* J Mol Biol, 2001. **311**(3): p. 467-73.
166. Hijazi, N., et al., *Copper binding to PrPC may inhibit prion disease propagation.* Brain Res, 2003. **993**(1-2): p. 192-200.
167. Sigurdsson, E.M., et al., *Copper chelation delays the onset of prion disease.* J Biol Chem, 2003. **278**(47): p. 46199-202.
168. Garnett, A.P. and J.H. Viles, *Copper binding to the octarepeats of the prion protein. Affinity, specificity, folding, and cooperativity: insights from circular dichroism.* J Biol Chem, 2003. **278**(9): p. 6795-802.
169. Viles, J.H., et al., *Local structural plasticity of the prion protein. Analysis of NMR relaxation dynamics.* Biochemistry, 2001. **40**(9): p. 2743-53.
170. Aronoff-Spencer, E., et al., *Identification of the Cu2+ binding sites in the N-terminal domain of the prion protein by EPR and CD spectroscopy.* Biochemistry, 2000. **39**(45): p. 13760-71.
171. Davies, P. and D.R. Brown, *The chemistry of copper binding to PrP: is there sufficient evidence to elucidate a role for copper in protein function?* Biochem J, 2008. **410**(2): p. 237-44.
172. Walter, E.D., M. Chattopadhyay, and G.L. Millhauser, *The affinity of copper binding to the prion protein octarepeat domain: evidence for negative cooperativity.* Biochemistry, 2006. **45**(43): p. 13083-92.
173. Nadal, R.C., et al., *Evaluation of copper2+ affinities for the prion protein.* Biochemistry, 2009. **48**(38): p. 8929-31.
174. Chattopadhyay, M., et al., *The octarepeat domain of the prion protein binds Cu(II) with three distinct coordination modes at pH 7.4.* J Am Chem Soc, 2005. **127**(36): p. 12647-56.
175. Chen, S.G., et al., *Truncated forms of the human prion protein in normal brain and in prion diseases.* J Biol Chem, 1995. **270**(32): p. 19173-80.
176. Mange, A., et al., *Alpha- and beta- cleavages of the amino-terminus of the cellular prion protein.* Biol Cell, 2004. **96**(2): p. 125-32.
177. McMahon, H.E., et al., *Cleavage of the amino terminus of the prion protein by reactive oxygen species.* J Biol Chem, 2001. **276**(3): p. 2286-91.
178. Evans, E.G., et al., *Interaction between Prion Protein's Copper-Bound Octarepeat Domain and a Charged C-Terminal Pocket Suggests a Mechanism for N-Terminal Regulation.* Structure, 2016. **24**(7): p. 1057-67.
179. Shyng, S.L., et al., *Sulfated glycans stimulate endocytosis of the cellular isoform of the prion protein, PrPC, in cultured cells.* J Biol Chem, 1995. **270**(50): p. 30221-9.

180. Nunziante, M., S. Gilch, and H.M. Schatzl, *Essential role of the prion protein N terminus in subcellular trafficking and half-life of cellular prion protein.* J Biol Chem, 2003. **278**(6): p. 3726-34.
181. Flechsig, E., et al., *Prion protein devoid of the octapeptide repeat region restores susceptibility to scrapie in PrP knockout mice.* Neuron, 2000. **27**(2): p. 399-408.
182. Atarashi, R., et al., *Deletion of N-terminal residues 23-88 from prion protein (PrP) abrogates the potential to rescue PrP-deficient mice from PrP-like protein/doppel-induced Neurodegeneration.* J Biol Chem, 2003. **278**(31): p. 28944-9.
183. Bremer, J., et al., *Axonal prion protein is required for peripheral myelin maintenance.* Nat Neurosci, 2010. **13**(3): p. 310-8.
184. Mitteregger, G., et al., *The role of the octarepeat region in neuroprotective function of the cellular prion protein.* Brain Pathol, 2007. **17**(2): p. 174-83.
185. Baumann, F., et al., *Functionally relevant domains of the prion protein identified in vivo.* PLoS One, 2009. **4**(9): p. e6707.
186. Li, P., et al., *Doppel-induced cytotoxicity in human neuronal SH-SY5Y cells is antagonized by the prion protein.* Acta Biochim Biophys Sin (Shanghai), 2009. **41**(1): p. 42-53.
187. Parkin, E.T., et al., *Cellular prion protein regulates beta-secretase cleavage of the Alzheimer's amyloid precursor protein.* Proc Natl Acad Sci U S A, 2007. **104**(26): p. 11062-7.
188. Griffiths, H.H., et al., *Prion protein interacts with BACE1 protein and differentially regulates its activity toward wild type and Swedish mutant amyloid precursor protein.* J Biol Chem, 2011. **286**(38): p. 33489-500.
189. Gimbel, D.A., et al., *Memory impairment in transgenic Alzheimer mice requires cellular prion protein.* J Neurosci, 2010. **30**(18): p. 6367-74.
190. Lauren, J., et al., *Cellular prion protein mediates impairment of synaptic plasticity by amyloid-beta oligomers.* Nature, 2009. **457**(7233): p. 1128-32.
191. Caetano, F.A., et al., *Amyloid-beta oligomers increase the localization of prion protein at the cell surface.* J Neurochem, 2011. **117**(3): p. 538-53.
192. Aguzzi, A. and T. O'Connor, *Protein aggregation diseases: pathogenicity and therapeutic perspectives.* Nat Rev Drug Discov, 2010. **9**(3): p. 237-48.
193. Supattapone, S., et al., *Identification of two prion protein regions that modify scrapie incubation time.* J Virol, 2001. **75**(3): p. 1408-13.
194. Barron, R.M., et al., *Changing a single amino acid in the N-terminus of murine PrP alters TSE incubation time across three species barriers.* Embo j, 2001. **20**(18): p. 5070-8.
195. Lawson, V.A., et al., *N-terminal truncation of prion protein affects both formation and conformation of abnormal protease-resistant prion protein generated in vitro.* J Biol Chem, 2001. **276**(38): p. 35265-71.
196. Norstrom, E.M. and J.A. Mastrianni, *The AGAAAAGA palindrome in PrP is required to generate a productive PrPSc-PrPC complex that leads to prion propagation.* J Biol Chem, 2005. **280**(29): p. 27236-43.
197. Wong, C., et al., *Sulfated glycans and elevated temperature stimulate PrP(Sc)-dependent cell-free formation of protease-resistant prion protein.* Embo j, 2001. **20**(3): p. 377-86.
198. Deleault, N.R., et al., *Protease-resistant prion protein amplification reconstituted with partially purified substrates and synthetic polyanions.* J Biol Chem, 2005. **280**(29): p. 26873-9.
199. Kocisko, D.A. and B. Caughey, *Searching for anti-prion compounds: cell-based high-throughput in vitro assays and animal testing strategies.* Methods Enzymol, 2006. **412**: p. 223-34.

200. Taylor, D.R., I.J. Whitehouse, and N.M. Hooper, *Glypican-1 mediates both prion protein lipid raft association and disease isoform formation.* PLoS Pathog, 2009. **5**(11): p. e1000666.
201. Aguzzi, A., C. Sigurdson, and M. Heikenwaelder, *Molecular mechanisms of prion pathogenesis.* Annu Rev Pathol, 2008. **3**: p. 11-40.
202. Jobling, M.F., et al., *Copper and zinc binding modulates the aggregation and neurotoxic properties of the prion peptide PrP106-126.* Biochemistry, 2001. **40**(27): p. 8073-84.
203. Sabareesan, A.T. and J.B. Udgaonkar, *Pathogenic Mutations within the Disordered Palindromic Region of the Prion Protein Induce Structure Therein and Accelerate the Formation of Misfolded Oligomers.* J Mol Biol, 2016. **428**(20): p. 3935-3947.
204. Carafoli, F., J.L. Saffell, and E. Hohenester, *Structure of the Tandem Fibronectin Type 3 Domains of Neural Cell Adhesion Molecule.* Journal of Molecular Biology, 2008. **377**: p. 524-534.
205. Sambrook, J., E.F. Fritsch, and T. Maniatis, *Molecular Cloning: A Laboratory Manual* Second Edition ed. 1989: Cold Spring Harbor Laboratory Press.
206. Perrier, V., et al., *Anti-PrP antibodies block PrPSc replication in prion-infected cell cultures by accelerating PrPC degradation.* Journal of Neurochemistry, 2004. **89**: p. 454-463.
207. Güntert, P., *Automated NMR structure calculation with CYANA.* Methods in Molecular Biology (Clifton, N.J.), 2004. **278**: p. 353-378.
208. Krieger, E., G. Koraimann, and G. Vriend, *Increasing the precision of comparative models with YASARA NOVA--a self-parameterizing force field.* Proteins, 2002. **47**: p. 393-402.
209. Doreleijers, J.F., et al., *CING: an integrated residue-based structure validation program suite.* Journal of Biomolecular Nmr, 2012. **54**: p. 267-283.
210. Delaglio, F., et al., *NMRPipe: a multidimensional spectral processing system based on UNIX pipes.* Journal of biomolecular NMR, 1995. **6**: p. 277-293.
211. Keller, R.L.J., *The Computer Aided Resonance Assignment Tutorial.* 2004.
212. *Sparky - NMR Assignment Program*.
213. Mulder, F.A., et al., *Altered flexibility in the substrate-binding site of related native and engineered high-alkaline Bacillus subtilisins.* Journal of Molecular Biology, 1999. **292**: p. 111-123.
214. Vries, S.J.d., M.v. Dijk, and A.M.J.J. Bonvin, *The HADDOCK web server for data-driven biomolecular docking.* Nature Protocols, 2010. **5**: p. 883-897.
215. Wassenaar, T.A., et al., *WeNMR: Structural Biology on the Grid.* Journal of Grid Computing, 2012. **10**: p. 743-767.
216. Giachin, G., et al., *The non-octarepeat copper binding site of the prion protein is a key regulator of prion conversion.* Sci Rep, 2015. **5**: p. 15253.
217. D'Angelo, P., et al., *X-ray Absorption Study of Copper(II)-Glycinate Complexes in Aqueous Solution.* J. Phys. Chem. B, 1998. **102**: p. 3114-3122.
218. Santuccione, A., et al., *Prion protein recruits its neuronal receptor NCAM to lipid rafts to activate p59fyn and to enhance neurite outgrowth.* J Cell Biol, 2005. **169**(2): p. 341-54.
219. Jacobsen, J., et al., *A peptide motif from the second fibronectin module of the neural cell adhesion molecule, NCAM, NLIKQDDGGSPIRHY, is a binding site for the FGF receptor.* Neurochemical Research, 2008. **33**: p. 2532-2539.
220. de Vries, S.J., M. van Dijk, and A.M. Bonvin, *The HADDOCK web server for data-driven biomolecular docking.* Nat Protoc, 2010. **5**(5): p. 883-97.
221. Parchi, P., et al., *Different patterns of truncated prion protein fragments correlate with distinct phenotypes in P102L Gerstmann-Straussler-Scheinker disease.* Proc Natl Acad Sci U S A, 1998. **95**(14): p. 8322-7.
222. Benetti, F., et al., *Cuprizone neurotoxicity, copper deficiency and neurodegeneration.* Neurotoxicology, 2010. **31**(5): p. 509-17.

223. Rossetti, G., et al., *Structural facets of disease-linked human prion protein mutants: a molecular dynamic study.* Proteins, 2010. **78**(16): p. 3270-80.
224. Steele, A.D., et al., *Prion protein (PrPc) positively regulates neural precursor proliferation during developmental and adult mammalian neurogenesis.* Proc Natl Acad Sci U S A, 2006. **103**(9): p. 3416-21.
225. Amoureux, M.C., et al., *N-CAM binding inhibits the proliferation of hippocampal progenitor cells and promotes their differentiation to a neuronal phenotype.* J Neurosci, 2000. **20**(10): p. 3631-40.
226. Bodrikov, V., et al., *RPTPalpha is essential for NCAM-mediated p59fyn activation and neurite elongation.* J Cell Biol, 2005. **168**(1): p. 127-39.
227. Carafoli, F., J.L. Saffell, and E. Hohenester, *Structure of the tandem fibronectin type 3 domains of neural cell adhesion molecule.* J Mol Biol, 2008. **377**(2): p. 524-34.
228. Silva, J.L., et al., *Experimental approaches to the interaction of the prion protein with nucleic acids and glycosaminoglycans: Modulators of the pathogenic conversion.* Methods, 2011. **53**(3): p. 306-17.
229. Prodromidou, K., et al., *Functional cross-talk between the cellular prion protein and the neural cell adhesion molecule is critical for neuronal differentiation of neural stem/precursor cells.* Stem Cells, 2014. **32**(6): p. 1674-87.
230. Walmsley, A.R., F. Zeng, and N.M. Hooper, *The N-terminal region of the prion protein ectodomain contains a lipid raft targeting determinant.* J Biol Chem, 2003. **278**(39): p. 37241-8.
231. Marianayagam, N.J., M. Sunde, and J.M. Matthews, *The power of two: protein dimerization in biology.* Trends Biochem Sci, 2004. **29**(11): p. 618-25.
232. Kulahin, N., et al., *Direct demonstration of NCAM cis-dimerization and inhibitory effect of palmitoylation using the BRET2 technique.* FEBS Lett, 2011. **585**(1): p. 58-64.
233. Valensin, D., et al., *Specific binding modes of Cu(I) and Ag(I) with neurotoxic domain of the human prion protein.* J Inorg Biochem, 2016. **155**: p. 26-35.
234. Migliorini, C., et al., *Copper-induced structural propensities of the amyloidogenic region of human prion protein.* J Biol Inorg Chem, 2014. **19**(4-5): p. 635-45.
235. Younan, N.D., et al., *Copper(II)-induced secondary structure changes and reduced folding stability of the prion protein.* J Mol Biol, 2011. **410**(3): p. 369-82.
236. Owen, F., et al., *Insertion in prion protein gene in familial Creutzfeldt-Jakob disease.* Lancet, 1989. **1**(8628): p. 51-2.
237. Quaglio, E., R. Chiesa, and D.A. Harris, *Copper converts the cellular prion protein into a protease-resistant species that is distinct from the scrapie isoform.* J Biol Chem, 2001. **276**(14): p. 11432-8.
238. Cox, D.L., J. Pan, and R.R. Singh, *A mechanism for copper inhibition of infectious prion conversion.* Biophys J, 2006. **91**(2): p. L11-3.
239. Baskakov, I.V., et al., *Pathway complexity of prion protein assembly into amyloid.* J Biol Chem, 2002. **277**(24): p. 21140-8.
240. Brown, D.R., C. Clive, and S.J. Haswell, *Antioxidant activity related to copper binding of native prion protein.* J Neurochem, 2001. **76**(1): p. 69-76.
241. Brown, D.R., *Prion protein expression aids cellular uptake and veratridine-induced release of copper.* J Neurosci Res, 1999. **58**(5): p. 717-25.
242. Pauly, P.C. and D.A. Harris, *Copper stimulates endocytosis of the prion protein.* J Biol Chem, 1998. **273**(50): p. 33107-10.
243. Giese, A., et al., *Effect of metal ions on de novo aggregation of full-length prion protein.* Biochem Biophys Res Commun, 2004. **320**(4): p. 1240-6.
244. Kuwahara, C., et al., *Prions prevent neuronal cell-line death.* Nature, 1999. **400**(6741): p. 225-6.
245. Thackray, A.M., et al., *Metal imbalance and compromised antioxidant function are early changes in prion disease.* Biochem J, 2002. **362**(Pt 1): p. 253-8.

246. Brown, D.R., et al., *Normal prion protein has an activity like that of superoxide dismutase.* Biochem J, 1999. **344 Pt 1**: p. 1-5.
247. Cui, T., et al., *Mapping the functional domain of the prion protein.* Eur J Biochem, 2003. **270**(16): p. 3368-76.
248. Miura, T., A. Hori-i, and H. Takeuchi, *Metal-dependent alpha-helix formation promoted by the glycine-rich octapeptide region of prion protein.* FEBS Lett, 1996. **396**(2-3): p. 248-52.
249. Bocharova, O.V., et al., *Copper(II) inhibits in vitro conversion of prion protein into amyloid fibrils.* Biochemistry, 2005. **44**(18): p. 6776-87.
250. Kim, N.H., et al., *Effect of transition metals (Mn, Cu, Fe) and deoxycholic acid (DA) on the conversion of PrPC to PrPres.* Faseb j, 2005. **19**(7): p. 783-5.
251. Sarafoff, N.I., et al., *Automated PrPres amplification using indirect sonication.* J Biochem Biophys Methods, 2005. **63**(3): p. 213-21.
252. Tsiroulnikov, K., et al., *Cu(II) induces small-size aggregates with amyloid characteristics in two alleles of recombinant ovine prion proteins.* Biochim Biophys Acta, 2006. **1764**(7): p. 1218-26.
253. Qin, K., et al., *Copper(II)-induced conformational changes and protease resistance in recombinant and cellular PrP. Effect of protein age and deamidation.* J Biol Chem, 2000. **275**(25): p. 19121-31.
254. Chen, V.B., et al., *MolProbity: all-atom structure validation for macromolecular crystallography.* Acta Crystallogr D Biol Crystallogr, 2010. **66**(Pt 1): p. 12-21.
255. Gordon, J.C., et al., *H++: a server for estimating pKas and adding missing hydrogens to macromolecules.* Nucleic Acids Res, 2005. **33**(Web Server issue): p. W368-71.
256. Rose, F., M. Hodak, and J. Bernholc, *Mechanism of copper(II)-induced misfolding of Parkinson's disease protein.* Sci Rep, 2011. **1**: p. 11.
257. Aliev, A.E., et al., *Motional timescale predictions by molecular dynamics simulations: case study using proline and hydroxyproline sidechain dynamics.* Proteins, 2014. **82**(2): p. 195-215.
258. Van Der Spoel, D., et al., *GROMACS: fast, flexible, and free.* J Comput Chem, 2005. **26**(16): p. 1701-18.
259. Jorgensen, W.L., et al., *Comparison of Simple Potential Functions for Simulating Liquid Water.* Journal of Chemical Physics, 1983. **79**(2): p. 926-935.
260. Cheatham, T.E., et al., *Molecular-Dynamics Simulations on Solvated Biomolecular Systems - the Particle Mesh Ewald Method Leads to Stable Trajectories of DNA, Rna, and Proteins.* Journal of the American Chemical Society, 1995. **117**(14): p. 4193-4194.
261. Hess, B., et al., *LINCS: A linear constraint solver for molecular simulations.* Journal of Computational Chemistry, 1997. **18**(12): p. 1463-1472.
262. Bussi, G., D. Donadio, and M. Parrinello, *Canonical sampling through velocity rescaling.* J Chem Phys, 2007. **126**(1): p. 014101.
263. Torda, A.E. and W.F. Vangunsteren, *Algorithms for Clustering Molecular-Dynamics Configurations.* Journal of Computational Chemistry, 1994. **15**(12): p. 1331-1340.
264. Kabsch, W. and C. Sander, *Dictionary of protein secondary structure: pattern recognition of hydrogen-bonded and geometrical features.* Biopolymers, 1983. **22**(12): p. 2577-637.